Computer Simulations Of Hard-Core Yukawa System In Confinement

Inaugural-Dissertation

zur Erlangung des Doktorgrades
der Mathematisch-Naturwissenschaftlichen Fakultät
der Heinrich-Heine-Universität Düsseldorf

vorgelegt von

Mojtaba Eshraghi

aus Teheran

Düsseldorf, März 2019

Aus dem Institut für Theoretische Physik II: Weiche Materie
der Heinrich-Heine-Universität Düsseldorf

Gedruckt mit der Genehmigung der
Mathematisch-Naturwissenschaftlichen Fakultät der
Heinrich-Heine-Universität Düsseldorf

Berichterstatter:

1. Prof. Dr. Jürgen Horbach

2. Prof. Dr. Hartmut Löwen

Tag der mündlichen Prüfung: 17.05.2019

This thesis is dedicated to my beloved wife **Pegah** whose unconditional encouragement and support made it possible for me to finish this work.

Acknowledgements

Firstly, I would like to express my sincere gratitude to my advisor Prof. Dr. Jürgen Horbach for the continuous support of my Ph.D. study, and related research, for his patience, motivation, and immense knowledge. His guidance helped me in all the time of research and writing of this thesis. I could not have imagined having a better advisor and mentor for my Ph.D. study.

Also, I would like thanks Prof. Dr. Hartmut Löwen for being my second referee and nice discussions.

I thank my dear colleagues Mehrdad Golkia, Nima Hamidi Siboni, Saswati Ganguly, Nicolas Höft, Gaurav Prakash Shrivastav, and Joachim Wenk for all the discussions, helps and for all the fun we have had in these years.

Last but not least, I would like to thank my family; my smart, beautiful, and gorgeous wife Pegah for her endless love and support, my parents, my brothers and sister, my parents-in-law and my brother-in-law for supporting me spiritually throughout writing this thesis and my life in general.

Summary

The hard-core Yukawa potential has been widely used to describe the effective interaction between like-charged colloids. The phase diagram of bulk hard-core Yukawa systems is well studied. It shows the emergence of three different phases, namely body-cantered cubic (BCC) crystal, face-centered cubic (FCC) crystal and fluid, and lines of first-order transitions BCC-fluid, FCC-fluid and BCC-FCC that intersect in a triple point

In this work, we investigate the phase behavior of hard-core Yukawa crystals and fluid in confinement via extensive molecular dynamics (MD) simulations in the NVT ensemble, i.e., with constant number of particles N, in fixed volume V, and at constant temperature T. We have studied these systems in two different type of confinements. First we have studied the behavior of hard-core Yukawa systems in presence of pair of short-range structureless flat hard walls and then the same process has been performed to observe the effect of a pair of relatively long-range flat charged walls on the hard-core Yukawa systems.

The FCC(111) crystal for different densities from the coexistence to slightly higher than coexistence density is investigated at the confinement of a pair of structureless flat hard walls. In this part due to the long-range interaction of hard-core Yukawa particles and short-range interaction of flat hard walls the multiple time step scheme for MD simulation is employed. We have observed that the FCC crystals in confinement of flat hard walls are stable. By using a thermodynamic integration scheme, we were able to calculate the free energy contribution of the system to form a FCC-wall interface. We have observed that the calculated values for FCC-wall interfacial free energies are negative and this negativity is increasing by increment of the density. This negativity means that the hard walls are attractive for the bulk particles.

The fluids at coexistence with FCC and densities lower than coexistence density were examined in presence of the flat hard walls. These density profile

analysis of these systems shows that some layers are forming in the vicinity of the flat hard walls. An analysis of the structure shows the formation of hexagonal layers (pre-freezing) at coexistence and slightly below the coexistence density. Moreover, calculation of the 2D packing fraction for the first formed layer close to the flat wall confirms that their density is close to the density of the first layers in FCC crystals. The free energy of the fluid-wall interface is calculated via thermodynamic integration scheme which shows the negative values. However, the values for the systems with phase transitions are not reliable.

The flat hard wall confinement was also examined on the BCC(111) crystals at coexistence and densities higher than the coexistence density. Our simulations and structure analysis show that a confined configuration with a BCC structure is divided into three regions. First one can observe the formation of hexagonal layers in the vicinity of the walls. Next, we see an area which consists of melted particles from the BCC crystal. The width of this region is decreasing by an increment of density. And the last part is a stable BCC(111) crystal which is located in the middle of the systems.

By investigating the behavior of the fluid which is at coexistence with the BCC for coexistence density and some low dense systems, we observe that same as FCC-fluid coexistence, the pre-freezing happens even for densities lower than coexistence. Moreover, a thermodynamic integration scheme is employed to calculate the fluid-wall interfacial free energy for systems at sufficiently low densities where no pre-freezing is observed. The calculated values are negative.

The next confinement is studied by inserting a pair of flat charged walls into a system with FCC(111) structure. As in the hard wall case, the crystals are stable; however, the calculated FCC-wall interfacial free energies are positive, which mean that the charged walls are not attractive for the bulk particles.

The confinement behavior of fluid hard-core Yukawa system at coexistence with FCC for coexistence and densities lower than coexistence at the presence of flat charged walls are studied. The structure analysis shows that the formed layers in the vicinity of the charged walls are just amorphous layers and there is no evidence for a phase transition. We have calculated the fluid-wall interfacial free energies, and it turned out that they are positive.

In addition, we have investigated the BCC(111) crystal in presence of flat charged walls. Our simulation and structure analysis show that some amorphous layers are formed in the vicinity of the charged walls. Also, between these layers and bulk BCC, there is a fluid area which is made by melted BCC particles.

For the fluid case in presence of charged walls, there is no evidence of pre-freezing and the layers which are formed in the vicinity of the charged walls are just amorphous layers. By performing thermodynamic integration scheme, we were able to calculate the fluid-wall interfacial free energies which are positive. These values are growing with respect to the densities but will saturate at densities close to the coexistence.

The results of this work open the door for targeted experimental and further theoretical studies on charged colloids in confinement.

Contents

1 Introduction

The phase behavior of a system of particles can be different from the one in confinement. For the systems confined between a pair of parallel walls, the competition between particle-particle and particle-wall interaction leads to a rich variety of phase transitions. Specifically, freezing and melting phenomena in confined geometries have been addressed in a large number of studies.

If we consider a fluid which is confined between a pair of flat walls, the interaction between fluid and wall can lead to formation of dense layers (higher than the bulk density) in the vicinity of the walls. These layers can be amorphous layers. Fluid systems such as hard-sphere fluids show a layering near the hard walls and exhibit pronounced oscillation in number density profiles (Courtemanche and van Swol, 1992; R. Roth and S. Dietrich, 2000; Snook and Henderson, 1978).

Moreover, the formed layers in the vicinity of the wall can have specific structure. In other words, a transition between fluid to the crystalline layer can happen in the vicinity of the walls. These systems at flat hard walls confinement experience freezing transition and a formation of the crystalline layer near the walls (Binder (1992), Kurt Binder, Horbach, Vink, and De Virgiliis (2008), Dijkstra (2004), Fortini and Dijkstra (2006), and Schmidt and Löwen (1997)). These studies show that the freezing of the fluid is happening slightly below the freezing point (pre-freezing).

Also by applying confinement on a fluid system, it is possible that freezing point gets below its actual value. This phenomenon which is called capillary crystallization or capillary freezing is reported by Kegel (2001) by studying hard spheres which are confined between hard walls. Laird and Davidchack, 2007 showed that for the confined hard sphere fluid between a pair of hard walls, the pre-freezing transition is independent of the distance between the hard walls and the formation of crystalline layers for the densities below the coexistence density, i.e., below the bulk freezing transition.

Most of colloidal systems are studied as charged colloids via experiments. In contrast to the hard-sphere case, in charged colloids one can tune the particle-particle interaction via changing their charges. In addition, if we confine a system of charged colloids between flat hard walls due to the competition between short-range wall-particle interaction and long-range particle-particle interaction it is possible to observe the layering and freezing phenomena well below the coexistence and more pronounced than the hard-sphere case. Experimental studies of the phase behavior of charged colloids in the bulk show a first order phase transition from a fluid to a body-centered cubic (BCC) crystal (Monovoukas and Gast (1989)). Moreover, theoretical studies on charged colloids in slit pore geometry (Gallardo, Grandner, Almarza, and Klapp (2012) and Grandner and Klapp (2008)) as well as on the phase behavior of crystalline bilayers (Messina and Hartmut Löwen (2003)) show a significant crystalline order in confined charged colloids.

Interactions between charged colloids are well described via the hard-core Yukawa model. In this work, we consider hard-core Yukawa system (El Azhar, Baus, Ryckaert, and Meijer (2000) and Meijer and El Azhar (1997)) which its phase diagram has been extensively studied by El Azhar, Baus, Ryckaert, and Meijer (2000) and Hynninen and Dijkstra (2003) and consists of FCC, BCC, and fluid phases. However, the phase behavior of the charged colloids at the bulk is well studied, but their response to the confinement is which is not considered widely via experiments and simulations.

In this work, we confined the charged colloids which are interacting via hard-core Yukawa potential between a pair of flat hard walls as well as a pair of charged walls, separately. In the case of hard wall confinement, we are dealing with two different types of interactions as short-range particle-wall and long-range particle-particle interactions. The competition between these two types of interaction can lead to a variety of interesting phenomena. From previous studies on hard-sphere confined between flat hard walls, we can expect the formation of high-density layers in the vicinity of the walls. These layers can be amorphous or hexagonal layers. Now the first question is if we confine the hard-core Yukawa states (BCC, FCC, fluids) by flat hard walls (charged and hard walls), do we expect to observe the same behavior at the walls? And what would be the structure of possible formed layers? If we observe a transition to a hexagonal layer in the vicinity of the walls, then how would be the interface between these layers and BCC crystal?

Moreover, previous studies on confined hard sphere particles indicate that the pre-freezing has happened slightly below the coexistence. The next important question is this can be the same for the hard-core Yukawa system? And if yes, how this pre-freezing is comparable to the one in hard-sphere case? Also, we understand that BCC crystal is not a stable state under confinement. So, What are the possible structural change within this phase?

In the following, to answer these questions, we employ Molecular Dynamics (MD) simulations in the NVT ensemble. Moreover, the interfacial free energy of fluid-wall and crystal-wall have been calculated via performing the thermodynamic integration scheme introduced by Benjamin and Horbach (2012).

The rest of this thesis is organized as follows: After the introduction (chapter 2), colloidal suspension and charged colloids are briefly introduced and we discuss how their interaction can be described via point and hard-core Yukawa potentials. We also describe how one can reach the hard-core Yukawa phase diagram from the one for point Yukawa system. Moreover a brief description about wetting, capillary freezing and pre-freezing phenomena is given. Also, in this chapter, we discuss the phase behavior of hard-sphere and charged colloids in confinement.

Then, in chapter 3 we introduce the computational scheme that we have used in this study. In this chapter, we introduce the model which is used to describe the hard-core Yukawa interaction. Moreover, a description of the different types of confinements such as hard and charged walls and their computational models are given. Besides, we briefly described the fundamentals of MD simulations and multiple time step schemes.

Chapter 4 gives an introduction on the thermodynamic integration schemes. In this chapter, we extensively discuss different thermodynamic integration methods for computing free energy differences.

An extensive description of the local bond order parameters which have been used to identify the structure of the particles in our studies is given in chapter 5. In this chapter, we introduce several schemes to calculate the local bond order parameters, and by combining with machine learning method, we give some criteria to identify the specific orders in a system of particles.

By employing the methods mentioned above, chapter 6 presents the results and findings of this study. These results can be divided into three main categories:

1. Hard wall confinement
    - FCC-fluid coexistence, FCC/fluid-wall interfacial free energy, structure analysis
    - BCC-fluid coexistence, BCC/fluid-wall interfacial free energy, structure analysis
2. charged wall confinement
    - FCC-fluid coexistence, FCC/fluid-wall interfacial free energy, structure analysis

- BCC-fluid coexistence, BCC/fluid-wall interfacial free energy, structure analysis

3. Crystal-fluid interfaces
    - FCC-fluid interfacial free energy
    - BCC-fluid interfacial free energy

2 Charged Colloids And Confinement

The screened Coulomb or Yukawa potential is widely used in elementary particles physics, solid state physics, and soft matter to describe effective interactions between charged particles. In this work, we use Yukawa potentials as models for charged colloidal particles. These models are presented in the following.

2.1 Colloidal Suspension

A colloidal suspension is a system of solid particles with size in the range between $1nm$ and $10\mu m$ which are suspended in a solvent. Two criteria define the lower and upper limits of the size of the colloidal particles. The lower limit is due to the requirement that the size of the colloidal particles should be considerably larger than that of the solvent. On the other hand, a colloidal particle behaves like a large molecule, and to this end, it needs to exhibit a robust thermal motion and the thermal motion when it is crucial that thermal displacement is a function of particle size and for the colloidal particles this size is limited to $10\mu m$ (Dhont (1996)). By considering the Stokes-Einstein equation for colloidal particles, the diffusion coefficient D can be described via $D = \frac{k_B T}{6\pi\eta a}$ in which T is temperature, η represents the dynamic viscosity and a is the radius of the particle. If we consider the upper limit of the size for colloidal particles ($a = 10\mu m$) , $k_B T = 300K$, and $\eta = 8.9 \times 10^{-4}\,\mathrm{Pa\,s}$ then the value of the diffusion coefficient regarding their thermal motion can be estimated as $D \approx 4.94 \times 10^{-15} m^2/s$. This value for diffusion coefficient means that the colloidal particles with size of $a = 10\mu m$ can move around $70nm$ in one second, and it would take $\approx 142\,\mathrm{s}$ for such a colloidal particle to move by its own size. So, if we consider a particle with the size larger than the upper limit, its movement is too slow, and sedimentation due to the gravitational field is always an issue for large colloidal particles.

2.2 Charged Colloids

One can categorize all the charged species in the system in terms of the primitive model as macroions, counterions, and coions. The charge of these species add up to zero due to charge neutrality. For instance, in $NaCl$, a Cl anion is the counterion for a Na cation. Macroions such as the charged colloids in a colloidal suspension are very large ions. Often, one can describe the effective interactions between like-charged colloidal particles in terms of a repulsive Yukawa potential, integrating out the degrees of freedom of the counter- and coions in the solvent in which the colloids are suppressed (Ivlev, LÃ, Morfill, Royall, et al. (2012) and Russel, Saville, and Schowalter (1991)).

By inserting the colloids in a fluid, one can always expect the making of charges. The degree of this charge directly depends on the medium in which colloids are immersed. One can describe the relationship between the electrostatic potential Φ and the charge density ρ of a system with dielectric constant ϵ via the Poisson equation as

$$\nabla^2\Phi = -\frac{\rho}{\epsilon} \quad . \tag{2.1}$$

The charge density of the colloidal system ρ can be calculated via

$$\rho = \sum_i z_i e n_i \tag{2.2}$$

where the sum is over different charge species, e is the elementary charge, n_i the number density of species i and z_i is the valence of species i. To solve the Poisson equation (2.1), we need to calculate the charge density ρ associated with the electrostatic potential Φ, and to this end, we need to know the number of ions. One can calculate the number of ions n_i as

$$n_i = n_0 \exp\left(\frac{-ez_i\Phi}{kT}\right) \tag{2.3}$$

in which n_0 is the number density of species i when the electrostatic potential $\Phi = 0$. So we can re-write the charge density ρ as

$$\rho = \sum_i z_i e n_{i0} \exp\left(\frac{-ez_i\Phi}{kT}\right) \quad . \tag{2.4}$$

Now by plugging ρ as given by equation (2.4) in equation (2.1) we obtain the following equation

$$\nabla^2\Phi = -\frac{e}{\epsilon}\sum_i z_i n_{i0} \exp\left(\frac{-ez_i\Phi}{kT}\right) \quad . \tag{2.5}$$

This equation is known as the Poisson-Boltzmann equation.

As a nonlinear differential equation, the Poisson-Boltzmann equation does not have any general analytic solution.

Hückel and Debye (1923) considered the linearized Poisson-Boltzmann equation that can be solved analytically. In a dilute solution and in a position far from the macroions one can write the Debye-Hückel approximation as

$$\left|\frac{e\Phi}{kT}\right| \ll 1 \quad . \tag{2.6}$$

With equation (2.6), the charge density as given by equation (2.4), can be expanded as (Pistoor (1991) and Sharma (2012))

$$\begin{aligned} \rho &= \sum_i z_i e n_{i0} \exp\left(\frac{-z_i e\Phi}{kT}\right) \\ &= \sum_i z_i e n_{i0} \left(1 - \frac{z_i e\Phi}{kT}\right) \\ &= \sum_i z_i e n_{i0} - \sum_i \left(\frac{z_i^2 e^2 n_{i0}\Phi}{kT}\right) \\ &= -\sum_i \left(\frac{z_i^2 e^2 n_{i0}\Phi}{kT}\right) \end{aligned} \tag{2.7}$$

in which $\sum_i z_i e n_{i0} = 0$ due to the charge neutrality. Using equation (2.7) we obtain the linearized Poisson-Boltzmann equation,

$$\begin{aligned} \nabla^2\Phi &= \left(\frac{e^2}{\epsilon kT}\sum_i z_i^2 n_{i0}\right)\Phi \\ &= \kappa^2\Phi \end{aligned} \tag{2.8}$$

with

$$\kappa^2 = \frac{e^2}{\epsilon kT}\sum_i z_i^2 n_{i0} \quad . \tag{2.9}$$

The inverse of κ has the unit of length and is defined as

$$\kappa^{-1} = \left(\frac{e^2}{\epsilon kT}\sum_i z_i^2 n_{i0}\right)^{-1/2} \quad . \tag{2.10}$$

It is called Debye or screening length.

So equation (2.5) can be solved as

$$\Phi = \Phi_0 \exp(-\kappa r) \tag{2.11}$$

in which $\Phi \to \Phi_0$ when $r \to 0$.

If we consider the Coulomb potential as $\Phi_0 = \frac{z_i z_j e^2}{4\pi\varepsilon r}$ then one obtains the Yukawa potential that describes the interaction of weakly charged colloids, as

$$\Phi_{\mathrm{Yuk}} = \frac{Q^2}{4\pi\varepsilon r}\exp(-\kappa r) \quad . \tag{2.12}$$

where $Q^2 = -z_i z_j e^2$ and z_i and z_j are the valence of species i and j, respectively.

2.3 Point Yukawa Interaction

So far we understand that one can describe the Yukawa interaction as

$$U(r) = U_0 \exp(-\kappa r)/r \tag{2.13}$$

in which r is the distance between the particles, U_0 represents the strength of interaction and κ^{-1} is inverse screening length.

There are two limits regarding inverse screening length κ^{-1}. For large κ, interactions are short-ranged and one effectively obtains a hard-sphere-like potential. On the other hand for $\kappa \to 0$ one obtains a Coulomb potential (Meijer and Frenkel (1991)).

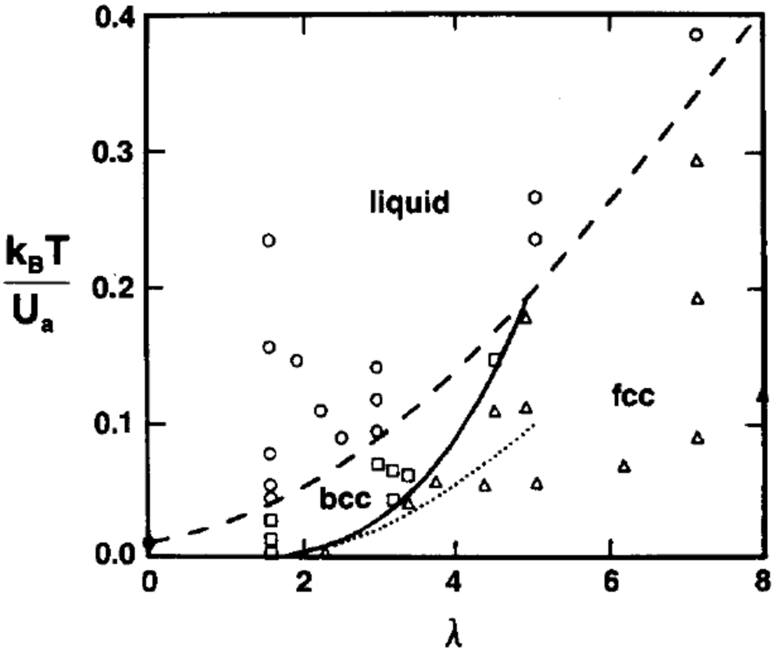

Figure 2.1: shows the phase diagram of point Yukawa system in terms of λ and $k_B T/U_a$ which is presented by Robbins, Kremer, and Grest (1988).

Using computer simulations, Robbins, Kremer, and Grest (1988) extensively studied the phase diagram of the Yukawa system. They have defined the energy per particle of a Yukawa system with N particles as

$$U_t = \frac{1}{2N} U_0 \sum_{i,j,i\neq j}^{N} (a/r_{ij}) \exp\left(\frac{-\lambda r_{ij}}{a}\right) \tag{2.14}$$

in which r_{ij} defines the distance between particles i and j and $a = \rho^{-1/3}$ is the inter-particle distance where ρ denotes the number density of the system and $\lambda = \kappa a$. The prefactor U_0 describes the strength of the interaction and is defined as

$$U_0 = \frac{(Ze)^2}{\epsilon a} \tag{2.15}$$

where Ze is the charge of the like-charged point particles.

Figure 2.1 shows the phase diagram of the point Yukawa system as proposed by Robbins, Kremer, and Grest (1988). This phase diagram shows $k_B T/U_a$ as a function of λ and consist of the points that they have studied. The phase diagram indicates that for low values of λ one can observe the body-centered cubic (BCC) crystal (square points) while for high values of λ there is a transition to a face-centered cubic (FCC) crystal (triangles). However, at high temperature they have observed a transition from BCC to fluid phase (circles). While Alexander (1978) believed that below the melting point the BCC crystal should always be stable when the transition is weakly first order, Robbins, Kremer, and Grest (1988) showed that with increasing temperature the range of stability for BCC is increasing, but the BCC phase is not stable for any large κ.

Hamaguchi, Farouki, and Dubin (1997) performed a variety of molecular dynamics (MD) and Monte Carlo (MC) simulations on screened Coulomb systems for both weak (Hamaguchi, Farouki, and Dubin (1996)) and strong screening regimes. They were able to calculate the temperature for both solid-fluid and solid-solid transition as a function of the screening parameter. The phase diagram that they have provided (figure 2.2) also covers the triple point of Yukawa systems. They have considered a system of point Yukawa particles and thus the potential between a pair of particles is given by

$$\phi(r) = \frac{Q^2}{4\pi\varepsilon r} \exp(-\kappa_D r) \tag{2.16}$$

in which r stands for the distance between two particles and $\lambda_D = \kappa_D^{-1}$ is the Debye length. In this form of the Yukawa potential one can characterize the thermodynamics of them by defining the two dimensionless parameters

$$\kappa = a/\lambda_D \tag{2.17}$$

and

$$\Gamma = \frac{Q^2}{4\pi\varepsilon_0 a k T} \tag{2.18}$$

where $a = \left(\frac{3}{4}\pi n\right)^{1/3}$ is the mean inter-particle distance and n stands for the number density of the system. Moreover, Γ represents a ratio of the unscreened Coulomb potential to the kinetic energy per particle. In their studies, they have presented the energy ratio Γ and normalized temperature τ as a function of

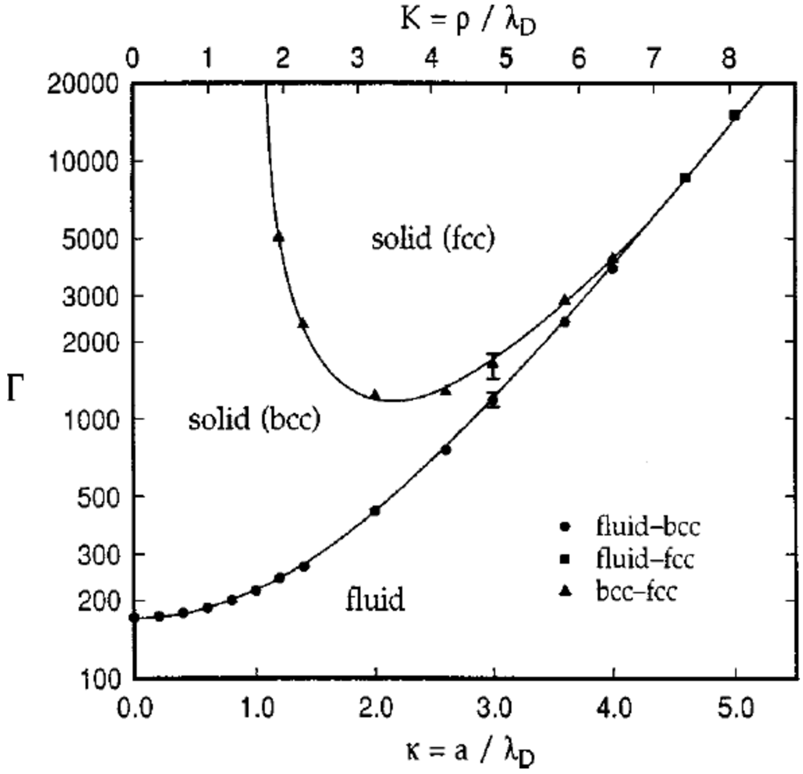

Figure 2.2: shows the phase diagram of point Yukawa system in terms of κ and Γ which is presented by Hamaguchi, Farouki, and Dubin (1997).

screening parameter κ for solid-fluid and solid-solid phase transition. Since the most natural temperature scale can be defined as typical phonon energy and this temperature is proportional to particle position's fluctuation then one can define τ as (Robbins, Kremer, and Grest (1988))

$$\tau = \frac{kT}{m\omega_E^2 a'^2} \tag{2.19}$$

in which they have used $a' = n^{-1/3}$ instead of Wigner-Seitz radius a and ω_E stands for Einstein frequency which is oscillation frequency of a particle around its rest position. Also, by replacing the a by a' as the length unit, one can define $K = a'/\lambda_D$ which leads to

$$K = (4/3\pi)^{1/3}\,\kappa \approx 1.61199\kappa \tag{2.20}$$

Later in this chapter, we will discuss the advantage of this substitution.

2.4 Hard-Core Yukawa Interaction

So far we have understood that charged colloids are particles which are suspended in a solvent. The work of Derjaguin and Landau (1941) and Verwey and Overbeek (1948) known as the DLVO theory, predicts that the effective interaction between a pair of colloidal particles can be divided into three different parts:

1. Hard-core repulsion interaction
2. Screened Coulomb repulsion
3. Van der Waals attraction

In most of situations the magnitude of the Van der Waals attraction is negligible in comparison to the other interactions. Then we can conclude the interaction with hard-core and screened Coulomb parts which is known as repulsive hard-core Yukawa interaction. So basically, the hard-core Yukawa system consists of hard-core particles which interact via a Yukawa potential.

Meijer and El Azhar (1997) proposed a method in which by using the Clausius-Clapeyron technique (Kofke (1993)) and numerical methods (Bennett (1976)) to calculate the free energy difference they were able to determine the coexistence line. The Clausius-Clapeyron technique is a method to identifying phase transition between two phases. If we consider a pressure-temperature (P-T) plane with two phases and coexistence line is separating these two phases then Clausius-Clapeyron relation can derive the slope of the tangent of the coexistence line. This slope is defined by $\frac{dP}{dT} = \frac{\Delta S}{\Delta V}$, where ΔS is entropy change and ΔV denotes the volume change. To calculate the free energy difference, Meijer and El Azhar (1997) needed to know the free energy difference of the two coexistence points. These two points are at an initial state near the coexistence line. They have calculated the free energy difference of the coexisting phases near the coexistence line. As a result, they have presented some points near the coexistence line which made them able to predict the coexistence with high accuracy. The Yukawa system consists of solid-fluid and solid-solid transition, and they decided to use it as a general case for the calculation of coexistence line via computer simulations. Moreover, they have considered this fact that the point Yukawa model is neglecting the size of colloidal particles and due to this issue, they have considered the modified Yukawa system with hard-core particles of diameter σ which interact via Yukawa potential. Their modified potential is defined as follows

$$\beta U = \begin{cases} \infty & \text{for } r < \sigma \\ \beta\varepsilon \frac{\exp[-\kappa\sigma(r/\sigma - 1)]}{r/\sigma} & \text{for } r > \sigma \end{cases} \tag{2.21}$$

in which ε is the interaction strength and $\beta = 1/k_B T$.

Their simulations with $\kappa\sigma = 5$, led to a phase diagram of the hard-core Yukawa system (figure 2.3) which proposed two triple points with FCC-BCC-fluid phases. This extra triple point is the main difference between this model and the point Yukawa model which is due to the fact that for the lower value of $\beta\lambda$ the phase diagram of the hard-core Yukawa system is significantly different regarding the point Yukawa system.

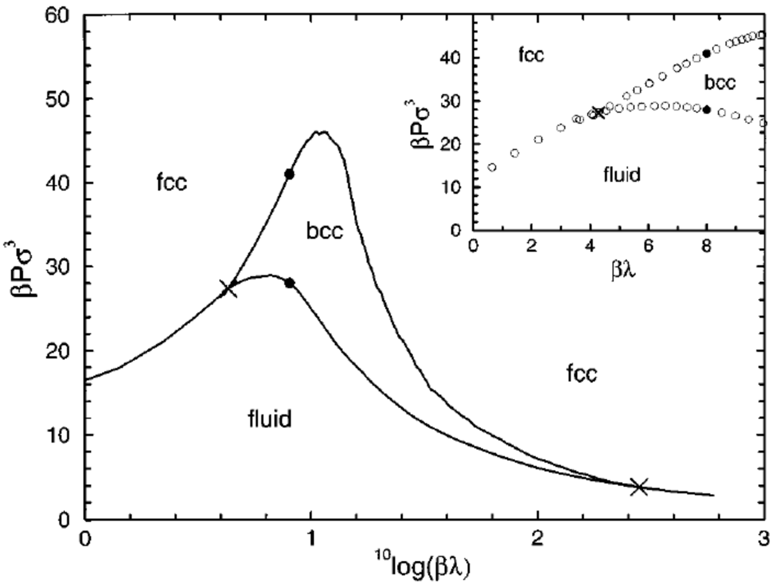

Figure 2.3: shows the calculated phase diagram of hard-core Yukawa system at $\kappa\sigma = 5$ in terms of pressure P and $lambda$ (Meijer and El Azhar (1997))

Later, El Azhar, Baus, Ryckaert, and Meijer (2000) by knowing the position of the first triple-point based on their previous calculation of coexistence line, were able to determine the line of triple point for hard-core Yukawa systems. Also, they have found that the observation of two different triple points is due to the presence of hard-core Yukawa particles and, on the other hand, the repulsion of the interaction. They have also found that, these two triple points lead to a region where the BCC can be stable but by the increment of κ the region will disappear.

Hynninen and Dijkstra (2003) determined the phase diagram of hard-core particles which interact via repulsive Yukawa potential with combining the calculation of Helmholtz free energy with Kofke integration method (Kofke (1993)). Kofke integration as known as Gibbs-Duhem integration first time proposed by Kofke (1993) and consist of numerical methods which combines the molecular simulations to the thermodynamic equations. This integration scheme has been used to define the phase coexistence lines. In this method, Kofke used a thermodynamic integration scheme to obtain the chemical potential of the coexisting phases by using the Gibbs-Duhem equation. Gibbs-Duhem equation is defined by

$$d(\beta\mu) = hd\beta + dVdP \tag{2.22}$$

with h the molar enthalpy, μ the chemical potential, and V and P are volume and pressure, respectively.

By using similar methods as El Azhar, Baus, Ryckaert, and Meijer (2000) and because the previous study was based on contact value of $\beta\varepsilon = 8$, they have tried to extend the phase diagram for a variety of contact values. The primary outcome of their studies is that they have found that for large enough values of $\beta\varepsilon$, it is possible to map the point Yukawa to hard-core Yukawa systems. By keeping the contact value $\beta\varepsilon$ as a fixed parameter, in the hard-core Yukawa, $\beta\epsilon$ and $\kappa\sigma$ are independent of each other so it indicates that they are independent of packing fraction $\eta = (\pi/6)\sigma N/V$. In other words, at coexistence apart from the equal chemical potential μ and pressure p we need to consider equal $\beta\varepsilon$ for different values of the packing fraction η.

To obtain this phase diagram, Hynninen and Dijkstra (2003) have introduced a mapping scheme between point Yukawa (Hamaguchi, Farouki, and Dubin (1997)) and the hard-core Yukawa systems. In this case, there would be different units in the case of hard-core Yukawa model to the point Yukawa one. For example, for the point Yukawa model we consider the inter-particle distance $a = n^{-1/3}$ as the length scale, in which n corresponds to the number density. By considering a as the length scale one can rewrite the point Yukawa potential as follows

$$\beta u\left(r\right) = \beta U_0 \frac{\exp\left(-a' r/a\right)}{r/a} \quad , \tag{2.23}$$

where $a' = K a$ is the inverse of screening length and βU_0 is the constant potential prefactor. If we consider that equations (2.21) and (2.23) are equal, then

$$\exp(\kappa\sigma)\sigma\beta\varepsilon = \beta U_0 a \tag{2.24}$$

and by considering $a = \left(\frac{6\eta}{\pi}\right)^{-1/3}\sigma$, one can rewrite (2.24) as

$$\beta U_0 = \exp(\kappa\sigma)\sigma\beta\varepsilon \left(\frac{6\eta}{\pi}\right)^{1/3} \tag{2.25}$$

and also extract the equation for a'

$$a' = \kappa\sigma \left(\frac{6\eta}{\pi}\right)^{-1/3} \quad . \tag{2.26}$$

So one can use equations (2.24) and (2.26) to map the point Yukawa phase diagram to the hard-core Yukawa one and vice versa. Moreover, Hynninen and Dijkstra (2003) provided a couple of fit functions for the phase boundaries of fluid-BCC and BCC-FCC. The fit function for the BCC-fluid boundary for $0 \leqslant a' \leqslant 12$ is given by

$$\begin{aligned} \ln\left(\beta U_0\right) = {} & 4.67 - 0.417a' + 0.1329a'^2 - 0.0104a'^3 \\ & + 4.343 \times 10^{-4} a'^4 - 6.924 \times 10^{-6} a'^5 \end{aligned} \tag{2.27}$$

while the phase boundary of BCC-FCC for $1.85 \leqslant a' \leqslant 6.8$ is

$$\begin{aligned} \ln\left(\beta U_0\right) = {} & 97.65106 - 150.469699a' + 106.626405a'^2 \\ & - 41.67136a'^3 + 9.639931a'^4 - 1.3150249a'^5 \\ & + 0.09784811a'^6 - 0.00306396a'^7 \quad . \end{aligned} \tag{2.28}$$

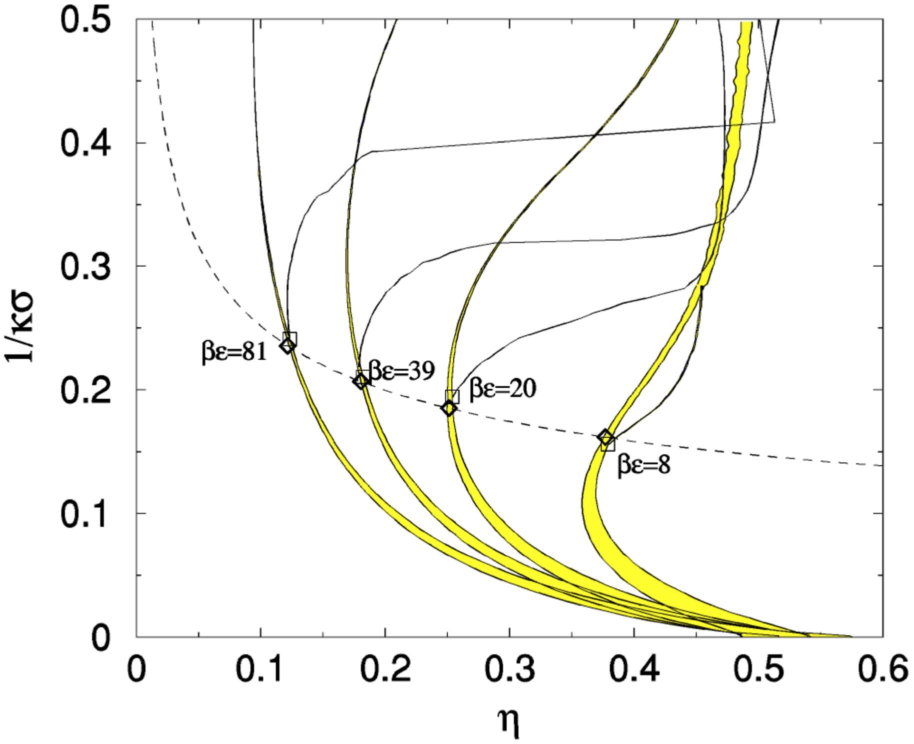

Figure 2.4: Phase diagram of hard-core Yukawa model for $\beta\varepsilon = 8, 20, 39$ and 81 from Hynninen and Dijkstra (2003).

Since their calculations are done for systems of about $N = 250$ particles, their estimations for the boundaries as well as thickness of coexistence lines, i.e. difference between density of coexisting phases are strongly affected by finite size effect. They have calculated the phase diagram of hard-core Yukawa systems for different contact values of $\beta\varepsilon = 8, 20, 39$ and 81. In their phase diagram one can see the phase behavior of hard-core Yukawa systems starts from hard sphere limits at $1/\kappa\sigma = 0$ in which packing fractions for FCC-fluid coexistence are equal to $\eta_{fcc} = 0.543$ and $\eta_{fl} = 0.491$ (Pollock and Hansen (1973)).

Figure 2.4 represents the phase diagrams of the hard-core Yukawa model for $\beta\varepsilon = 8, 20, 39$ and 81 and as one can see that for especially for high values of $\beta\varepsilon$ the difference between the coexistence densities are very small in comparison to the systems like hard-sphere. Also, the difference between hard-core and point Yukawa phase diagrams are more pronounced by increment of the contact value $\beta\varepsilon$. The phase diagram for contact value of $\beta\varepsilon = 81$ is the basis of this thesis and will be discussed more in the following chapters.

2.5 Phase Behavior In Confinement

The phase behavior of particles in confinement can be entirely different from that in the bulk. In general, confinement leads to an inhomogeneous structure, for example for a system confined between two walls, one can observe a layering at walls. Such a system of particles at confinement can lead to several different phenomena like wetting, pre-freezing, capillary freezing, etc. In this section, we will give some description of these phenomena and mainly will give some idea about the behavior of hard-spheres and charged colloids in the different type of confinements.

2.5.1 *Wetting Phenomena, Capillary Freezing And Pre-freezing*

If one puts a fluid drop on the surface of a solid, then one can expect that the fluid will cover the surface to the point that both fluid and solid are in equilibrium.

Consider an environment with three different phases such as a fluid, a solid surface, and a gas. If we assume that the fluid is in contact with the surface and the ideal gas surrounds them, then by the Young equation (Young et al., 1805) one can describe the relationship between surface tensions of these phases and also contact as follows (see Fig. 2.5)

$$\gamma_{sg} = \gamma_{sf} + \gamma_{fg} \cos\theta \tag{2.29}$$

where γ_{sg}, γ_{sf}, γ_{fg}, are solid-gas, solid-fluid and fluid-gas surface tension and θ is the contact angle. Note that these values of surface tension are defined when they are in thermodynamic equilibrium (Bonn, Eggers, et al., 2009; de Gennes, 1981), and in fact the Young equation can be derived from the force balance between these γs.

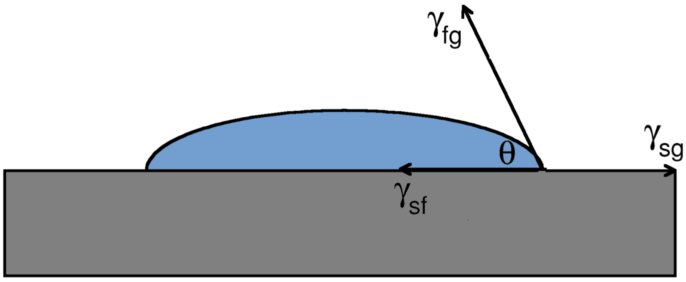

Figure 2.5: Schematic of relation between surface tension in a wetting phenomenon which is introduced by Young et al. (1805).

Depending on the internal and external situation of a system, the contact between fluid and surface can be categorized in three different scenarios:

1. The fluid completely covers the surface.
2. The fluid remains as a drop such how that some part of it is in contact with the surface.
3. The fluid does not cover the surface and tends to leave it.

One can also define these scenarios concerning the contact angle. If $\theta = 0°$, then $\gamma_{sg} = \gamma_{sf} + \gamma_{fg}$ and this corresponds to the case that fluid completely covers the surface and is called "complete wetting." If $0^\circ < \theta < 180^\circ$ then $\gamma_{sg} < \gamma_{sf} + \gamma_{fg}$ and this case is called partial wetting which in this case the fluid drop is invested by a thin film on the surface. In the very last example, if $\theta = 180^\circ$, then the fluid tends to leave the surface and is called non-wetting phenomenon and this corresponds to a layer of gas between the solid surface and fluid. We have shown these three different type of wetting in Fig. 2.6.

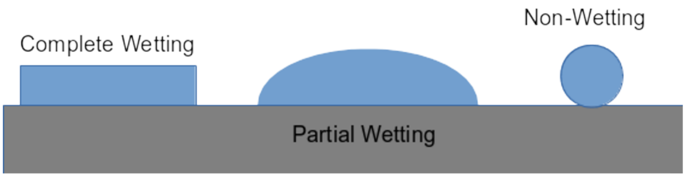

Figure 2.6: shows the different types of wetting.

One can also extend this concept to a system consisting of a fluid, a crystal, and a flat wall. Then we can re-write equation (2.29) as follows

$$\gamma_{sf} \cos\theta = \gamma_{fw} - \gamma_{cw} \tag{2.30}$$

where γ_{sf}, γ_{fw}, γ_{cw}, are crystal-fluid, fluid-wall and solid-wall surface tension and θ is the contact angle.

Lets consider a fluid which is confined by a pair of flat walls. In this case, well below the freezing point if a meta-stable crystal phase wets the surface, the phenomenon is called pre-freezing (Courtemanche and van Swol, 1992; Laird and Davidchack, 2007). But also the freezing can be induced by confinement which is mostly freezing of whole fluid and not some preferred layers close to the wall, which is called capillary freezing (Dijkstra, 2004; Kegel, 2001).

2.5.2 *Hard-Spheres and Charged Colloids In Confinements*

The behavior of hard sphere systems and charged colloids confined by flat and structured walls especially evidences of freezing and melting in such a system attracts a lots of attentions in past decades.

Snook and Henderson (1978) studied the phase behavior of the hard-sphere fluid system near a hard wall by performing Monte Carlo simulations. In density profile of this confined system, they have observed fluctuations with high densities near the hard wall. They have seen that the particles which are near the hard walls tend to leave the walls, but they will push back to the walls due to the interaction with bulk particles. Also, the same thing is happening to the particles in the second layer, they want to move to the first layer, but they will push back to the second layer. They have also found out that the high density of hard sphere fluid near the hard wall is because of their quasi-random walk in two dimensions and the number of particles does not play a role in that. However they argue that assuming to have an ordered structure, e.g. hexagonal order near the hard wall is not unusual, however, they have seen no evidence for such an arrangement.

Later on, studies on wetting phenomena in the hard sphere systems at confinement showed some fluctuation in density profiles. These fluctuations are considered as freezing and melting layers for the fluid-solid interface (Courtemanche and van Swol (1992)). During these studies, it has been observed that by decreasing the pressure of the systems the number of formed layers close to the walls are reducing and for low enough pressure all the layers will melt. Moreover, a series of molecular dynamics (MD) simulations have performed on the hard sphere systems which were in contact with a single smooth hard wall (Courtemanche, Pasmore, and Van Swol (1993)). This type of wall was coupled to the system in one dimension and acted like a piston to keep the pressure constant. The density profiles of this study showed the observation of crystal layers next to the wall. These layers are formed at the pressure under the bulk crystallization pressure which made this work as the first study which demonstrates pre-freezing for solid-fluid simulations.

Also, the phase diagram for a range of densities of the hard spheres which are confined between parallel plates has been calculated by Schmidt and Löwen (1997). They performed a Monte Carlo (MC) simulation on a system of hard sphere particles which were confined by a pair of parallel glass plates to study the phase diagram of this hard sphere system in confinement. By changing the separation of two plates from the hard sphere diameter to infinity, they were able to study the systems from 2D limits of hard disks to the 3D bulk hard sphere. By providing the phase diagram for the confined hard sphere, they have observed very weak and very strong first-order transition between crystals as well as a freezing transition for the confined hard sphere fluid. Huisman, Peters, et al. (1997) have used X-ray scattering experiments to study liquid gallium metal in contact with a solid wall (diamond) with (111) orientation. Their results (density profile) indicate a pronounced layering of the liquid near the wall, which this layering is suppressed by increasing the distance of fluid from the wall. They have mentioned that the liquid near this solid wall appears to be a solid-like structure mostly at lower temperatures.

Dijkstra (2004) employed Monte Carlo (MC) simulations on hard sphere fluids which were confined by two flat hard walls. The density profiles in this work show the formation of a crystalline layer near the hard walls. Moreover, the study indicates that the thickness of this crystalline layers is growing logarithmically by the difference between fluid and bulk densities. Later on, Fortini and Dijkstra (2006) considered a system of hard spheres confined between two parallel hard plates. For this system, they were able to calculate the equilibrium phase diagram. By changing the distance between two plates, they have shown that it is possible to observe the freezing and melting transition and they have confirmed that by inducing the hard plates in a system of bulk hard spheres, the system will form a (111) crystalline layer by increasing of the entropy.

Carbajal-Tinoco, Castro-Román, and Arauz-Lara (1996) studied the static properties of colloidal suspensions which were confined by a pair of glass plates. They have used the digital video microscopy and have calculated the statistic properties for a wide range of colloidal particles concentration in the liquid phase. Moreover, by considering a pair potential which they derived from the Ornstein-Zernike equation Hansen and McDonald (1990), they found out that the wall not only prevents the particles move to the plane but also it may modify the particles move through the homogeneous system.

Grandner and Klapp (2008) performed Monte Carlo (MC) simulations in the NPT ensemble to study the phase behavior of charged colloids in confinement and investigate freezing. They considered macroions which are interacting via DLVO interactions. They showed that the freezing for this confined system occurs below the bulk freezing point. Moreover, Puertas, de las Nieves, and Cuetos (2015) studied the phase behavior of charged colloids which are confined by a pair of parallel planes by performing Monte Carlo simulations in the canonical ensemble. They showed that for large charges and strong confinement the internal energy of the confined charged colloids is decreasing. Moreover, they showed that the repulsion is less strong in comparison with charged colloids at bulk.

Here, in this work, we study the phase behavior of charged colloids which are described via hard-core Yukawa potential in confinement by performing molecular dynamics (MD) simulations in the NVT ensemble. In the following, we will explain the method and the results of these simulations in detail.

3 Computer Simulation Details

In this chapter, we will introduce the simulation techniques, i.e. the numerical algorithms, analysis methods, etc. that we have used in our studies. Moreover, the potential used for particle-particle as well as particle-wall interactions will be discussed in detail. In addition, we give an introduction on molecular dynamics (MD) simulation, NVT ensemble and the corresponding thermostat that we have used, and the methods for improving the simulation performance such as multiple time-step schemes and neighbor lists.

3.1 Modeling Hard-Core Yukawa Interaction

In chapter 2, we have already mentioned that the interaction between charged colloids can be described via a hard-core Yukawa potential as described by eq. (2.21) (Hynninen and Dijkstra, 2003). This potential consists of a Yukawa interaction for $r > \sigma$ and hard-core interaction for $r < \sigma$, in which r is the distance between each pair of particles and σ is the diameter of a hard-core particle. For convenience, we have replaced the hard-core interaction by an inverse power-law potential $\propto (1/r)^{256}$. So the interactions between charged colloids in our simulation are given by

$$\beta u\left(r\right) = \beta\varepsilon\left(\frac{\exp\left[-\kappa\sigma\left(r/\sigma-1\right)\right]}{r/\sigma} + \left(\frac{\sigma}{r}\right)^{256}\right) \tag{3.1}$$

with κ the screening parameter, σ the diameter of hard-core particles, $\beta = 1/k_BT$ the inverse thermal energy and ε as energy of a pair of particles at contact.

This change from hard-core interaction to the inverse power-law potential is chosen such that it does not have a significant effect on the structure and behavior of hard-core Yukawa systems in the bulk. Benjamin and Horbach (2015) show that the phase behavior and the free energy in FCC-fluid interface with inverse power-law potential ($\propto (\frac{1}{r})^{256}$) is very similar to the one for hard spheres. Figure 3.1 shows the comparison between the potentials which are introduced via equations (2.21) and (3.1). As already discussed in chapter 2, the phase diagram of hard-core Yukawa systems are extensively studied by Hynninen and Dijkstra (2003). Here, we use equations (2.27) and (2.28) to produce the phase diagram of the systems that we want to study. In our study, we consider BCC, FCC and fluid phases around BCC-fluid and FCC-fluid coexistence states.

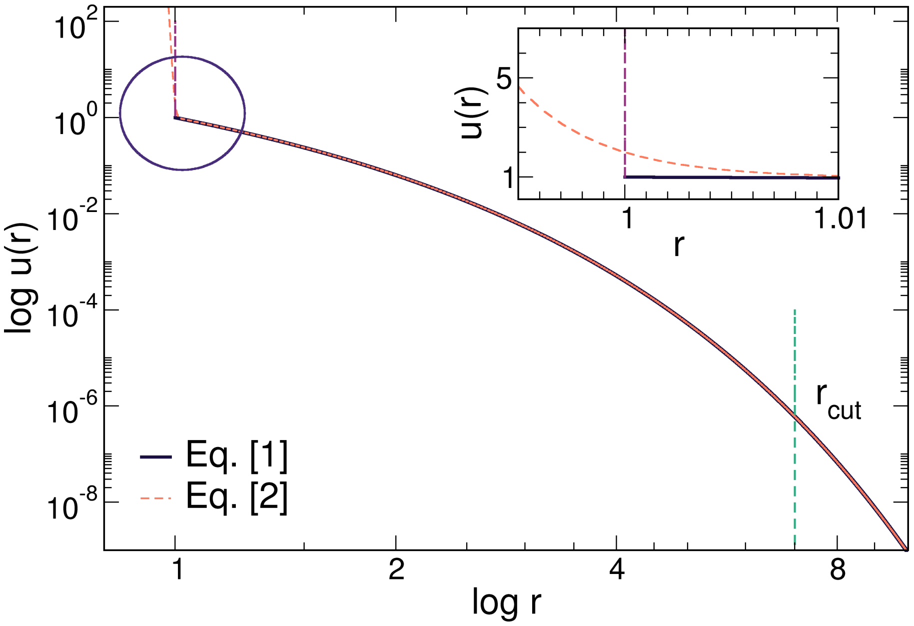

Figure 3.1: shows the comparison of the potential Eq. (3.1) with the hard-core Yukawa potential of Eq. (2.21).

Figure 3.2 shows the phase diagram of hard-core Yukawa systems as a function of packing fraction η at the contact value $\beta\epsilon = 81$. This phase diagram includes BCC, FCC, and fluid phases. Here, the coexistence boundaries are shown as dashed lines. In the inset of figure 3.2, the densities are displayed that we consider in the following for the fluid and BCC states at $1/\kappa\sigma = 0.486$ (see chapter 6).

3.2 Modeling Hard Flat Walls Interaction

An inverse power-law potential also models the interaction between hard-core Yukawa particles and the hard flat walls. However, this potential is acting in z-direction ($\propto (1/z)^{256}$) in which z indicates the distance between a particle and the flat wall. Since we have placed these parallel walls at $z = 0$ and $z = L_z$, the interaction between the hard flat wall and each hard-core Yukawa particle can be written as

$$u^{h}_{p-fw} = \epsilon \left[\left(\frac{\sigma}{z}\right)^{256} + \left(\frac{\sigma}{L_z - z}\right)^{256} \right] \tag{3.2}$$

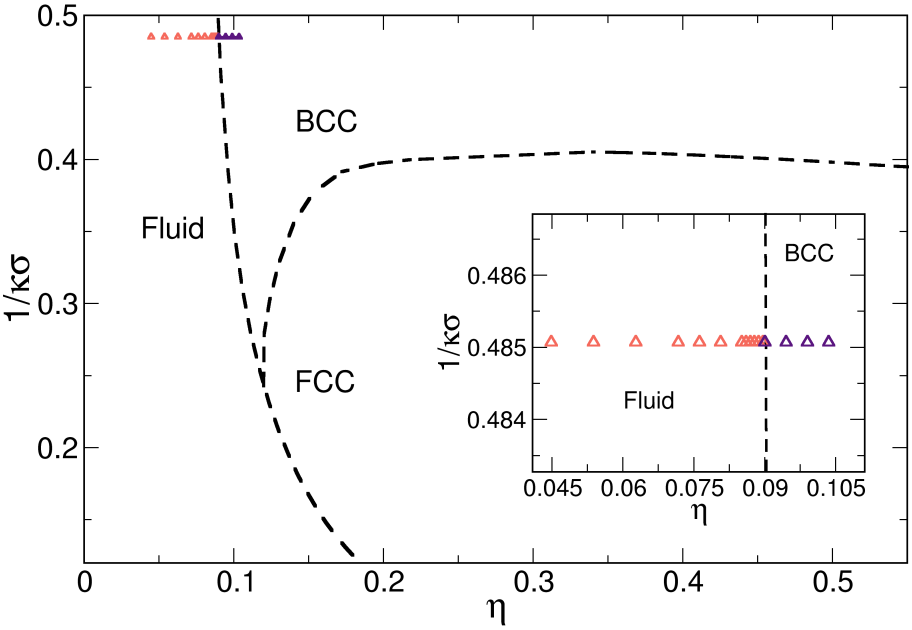

Figure 3.2: shows the phase diagram of the Hard-core Yukawa system in bulk which consists of FCC, BCC and fluid phases. This phase diagram is calculated by equations (2.27) and (2.28) as proposed by Hynninen and Dijkstra (2003).

Here, for the sake of simplicity, the parameter ϵ is set to one. The potential is cut-off at $z_{\text{cut}} = 2.0\sigma$, and shifted to zero at z_{cut}.

3.3 Modeling Charged Walls Interactions

The second type of confinement that we consider in this study is a pair of parallel charged walls. This wall is similar to the hard-core Yukawa small-big particle interaction, as introduced by Louis, Allahyarov, Löwen, and Roth (2002) and later on modified by Karanikas, Dzubiella, Moncho-Jordá, and Louis (2008). Hence the wall-particle interactions are given by

$$u_{fw} = \begin{cases} \infty & \text{for } \; r < \frac{\sigma}{2} \\ \varepsilon \exp\left[-\kappa\left(z - \frac{\sigma}{2}\right)\right] & \text{for } \; r \geqslant \frac{\sigma}{2} \end{cases} . \tag{3.3}$$

As for the hard wall case, we have used an inverse power-law term to model the hard sphere part. So in our simulation model, the interaction between charged walls and hard-core Yukawa particles is defined as

$$\begin{aligned} u^{c}_{p-fw} = \varepsilon \exp\left[-\kappa\left(L_z - z - \frac{\sigma}{2}\right) - \kappa\left(z - \frac{\sigma}{2}\right)\right] \\ + \varepsilon\left[\left(\frac{\sigma}{z}\right)^{256} + \left(\frac{\sigma}{L_z - z}\right)^{256}\right] \quad . \end{aligned} \tag{3.4}$$

Here, the walls are placed at $z = 0$ and $z = L_z$ and for truncation of interaction the cut off is set to $z_{\text{cut}} = 4.0\sigma$.

3.4 Molecular Dynamics (MD) Simulation

Due to the similarity to real experiments, molecular dynamics (MD) is one of the most popular and well-known computer simulation method (Frenkel and Smit (2001)). In a MD simulation, Newton's equations of motion are solved for a system consisting of N particles, interacting via a model potential as discussed in the previous section. To this end, one has to solve the equations of motion until the system reaches an equilibrated state where the thermodynamics of the system no longer changes with time. After reaching equilibrium, one can perform the analysis of the trajectories and calculate different thermodynamic properties.

3.4.1 *Solving the Equations of Motion*

After choosing an interaction model for the calculation of the forces between the particles, one needs to integrate Newton's equations of motion which are defined as

$$m_i \frac{d^2 \mathbf{r}_i}{dt^2} = \mathbf{F}_i \tag{3.5}$$

in which $\mathbf{F}_i$ is the total force on particle i with mass m_i and at position $\mathbf{r}_i$. The force $\mathbf{F}_i$ can be directly calculated via

$$\mathbf{F}_i \left(\mathbf{r}_i(t)\right) = -\nabla_{r_i} U \left(\mathbf{r}_i(t)\right) \tag{3.6}$$

in which U is potential energy and ∇_{r_i} is gradient with respect to $\mathbf{r}_i$. In this work, we have employed a widely used integration method, known as the velocity Verlet algorithm (Swope, Andersen, Berens, and Wilson (1982)). The position and velocity update via velocity Verlet algorithm can be written as

$$\mathbf{r}_i \left(t + \Delta t\right) = \mathbf{r}_i \left(t\right) + \mathbf{v}_i \left(t\right) \Delta t + \frac{\mathbf{F}_i \left(t\right)}{2m_i} \Delta t^2 + \Theta \left(\Delta t^4\right) \tag{3.7}$$

$$\mathbf{v}_i \left(t + \Delta t\right) = \mathbf{v}_i \left(t\right) + \frac{\Delta t}{2m_i} \left[\mathbf{F}_i \left(t\right) + \mathbf{F}_i \left(t + \Delta t\right)\right] + \Theta \left(\Delta t^4\right) \tag{3.8}$$

where $\mathbf{r}_i \left(t\right)$ and $\mathbf{v}_i \left(t\right)$ correspond to the position and velocity of particle i at time t, respectively.

The velocity Verlet algorithm allows to perform MD simulations in the microcanonical ensemble, i.e. for systems at constant particle number N, constant volume V and constant energy E. It belongs to the class of symplectic algorithms and thus it correctly describes the symmetries of the underlying Newton's equations of motion (e.g. time reversibility).

3.4.2 *MD Simulations at fixed Temperature*

When we are talking about performing molecular dynamics (MD) simulations at constant temperature, we are coupling a large heat bath to a system of N

particles with a fixed volume V to have average value of the temperature equal to a constant.

In this work, we have kept the temperature constant, by coupling our system of particles to the Berendsen thermostat which has been proposed by Berendsen, Postma, et al. (1984). In this method, a system of N particles is coupled to the heat bath with a fixed temperature T_0 which is considered as the reference temperature. To this end, one needs to insert the friction and stochastic terms into the equations of motion (Schneider and Stoll (1978)). This coupling is done in terms of a Langevin equation for each particle i that has the following form (Berendsen, Postma, et al. (1984))

$$m_i \dot{v}_i = F_i - m_i \gamma_i v_i + R_i(t) \tag{3.9}$$

in which i, γ_i is a damping constant and $R_i(t)$ a Gaussian stochastic term with a mean value of zero and $\left\langle R_i(t) R_j(t+\tau) \right\rangle = 2 m_i \gamma_i k T_0 \delta(\tau) \delta_{ij}$. In equation (3.9), the damping constant γ_i controls how strongly the heat bath and the system are coupled. According to the Langevin equation (3.9), the system globally couples to the heat bath and in the meantime locally couples to the random noises. Since we need to have only the global coupling, we have to modify equation (3.9). One can derive the time dependent temperature T from the derivative of the kinetic energy E_{kin} as

$$\frac{dE_{kin}}{dt} = \lim_{\Delta t \to 0} \left[\frac{1}{\Delta t} \left(\sum_{i=1}^{3N} \frac{1}{2} m_i v_i^2(t+\Delta t) - \sum_{i=1}^{3N} \frac{1}{2} m_i v_i^2(t) \right) \right] \tag{3.10}$$

in which m_i is the mass of particle i. The difference between the velocity at time t and $t + \Delta t$ can be written as

$$\Delta v_i = \frac{1}{m_i} \int_t^{t+\Delta t} \left[F_i(t') - m_i \gamma_i v_i(t') + R_i(t') \right] dt' \tag{3.11}$$

and since $R(t')$, $v_i(t)$, and $R(t' + \Delta t)$ are not correlated and if we consider the damping constant $\gamma_i = \gamma$ for all particles then

$$\sum_{i=1}^{3N} \int_t^{t+\Delta t} dt' \int_t^{t+\Delta t} dt" R_i(t') R_i(t") = 6 N m \gamma k T_0 \Delta t$$

$$\frac{dE_{kin}}{dt} = \sum_{i=1}^{3N} v_i F_i + 2\gamma \left(\frac{3N}{2} k T_0 - E_k \right) \tag{3.12}$$

in which the first term is equal to minus the derivative of the potential energy and the next term describes the global coupling to the heat bath. So one can write the modified Langevin equations of motion which consist of only global coupling to the heat bath as

$$m_i \dot{v}_i = F_i + m_i \gamma \left(\frac{T_0}{T} - 1 \right) v_i \tag{3.13}$$

Now to obtain the desired temperature we can scale the velocities regarding this temperature. To scale the velocity one needs to introduce a scaling factor as

$$sf = 1 + \frac{\Delta t}{\tau_T} \left[\frac{T_0}{T\left(t - \frac{\Delta t}{2}\right)} - 1 \right] \tag{3.14}$$

This proper scaling minimizes the $\sum_i m_i (\Delta v_i)^2$ and satisfies the global constraints via a least square local disturbance.

The crucial parameter in this thermostat is τ_T which controls the strength of the coupling. If the value of the coupling parameter is too high, then the thermostat is technically turned off, and the temperature will reach to the value which is appropriate for the micro-canonical ensemble and won't fluctuate over the desired temperature for canonical ensemble. On the other hand, if the value of τ is too small, then it will cause a too small fluctuation which is not realistic (Hünenberger (2005)). In fact, the special case of the Berendsen thermostat with $\tau = \Delta t$ which connects the controlling parameter of the thermostat to the time step completely suppresses temperature fluctuations. Moreover, in our MD simulation as an optimum value $\tau \sim 0.2$ has been used.

3.5 Multiple time-step

As we have already mentioned in the previous sections, in some cases especially when we are studying the behavior of hard-core Yukawa particles confined by hard walls, basically, we are dealing with two different interactions ranges. The hard walls introduce a short-range interaction while the hard-core Yukawa interaction has a longer range. As a consequence of this difference, to integrate the equations of motion, we need to use the time step which is appropriate for the short-range interactions. This means that the long-range interactions should be also considered with the same time step which is expensive regarding computational time.

To overcome this timescale problem, Tuckerman, Berne, and Martyna (1992) have proposed a multiple time step scheme to solve the equations of motion using a Liouville formalism. If we consider a single particle system with force $\mathbf{F}$ then one can write the Liouville operator as (Frenkel and Smit (2001))

$$iL = iL_r + iL_p \tag{3.15}$$

in which iL_r and iL_p correspond to shifts in positions and momenta, respectively and they can be defined as

$$\begin{aligned} iL_r &= \mathbf{v}\frac{\partial}{\partial \mathbf{r}} \\ iL_p &= \frac{\mathbf{F}}{m}\frac{\partial}{\partial \mathbf{v}} \end{aligned} \tag{3.16}$$

where $\mathbf{v}$ represent velocity and $\mathbf{r}$ shows the position. Moreover, operators $e^{L_r t}$ and $e^{L_p t}$ lead to the translation of coordinates and momenta, respectively.

The total Liouville operator iL can be defined as $iL_r + iL_p$, but since they are non-commuting operators one can not substitute the $\exp(iLt)$ by $\exp(iL_r t) \times \exp(iL_p t)$. To write the total Liouville operator iL in terms of the time evolution operator $exp(iL\Delta t)$, we can extend them by considering the time step Δt as

$$\exp(iL\Delta t) \approx \exp(iL_p \frac{\Delta t}{2}) \exp(iL_r \Delta t) \exp(iL_p \frac{\Delta t}{2}) \tag{3.17}$$

Now by applying the Liouville operator with initial condition for all particles $\mathbf{r}(0)$, $\mathbf{v}(0)$ as

$$e^{iL\Delta t}(\mathbf{r}(0), \mathbf{v}(0)) = \Big(\mathbf{r}(0) + \Delta t \mathbf{v}(0) + (\Delta t^2/2m)\mathbf{F}(0), \mathbf{v}(0) + (\Delta t^2/2m)(\mathbf{F}(0) + \mathbf{F}(\Delta t))\Big) \tag{3.18}$$

So we obtain the velocity Verlet algorithm form the application of the time evolution operator over a time step Δt.

$$\begin{aligned} \mathbf{r}(\Delta t) &= \mathbf{r}(0) + \Delta t \mathbf{v}(0) + (\Delta t^2/2m)\mathbf{F}(0) \\ \mathbf{v}(\Delta t) &= \mathbf{v}(0) + (\Delta t^2/2m)(\mathbf{F}(0) + \mathbf{F}(\Delta t)) \end{aligned} \tag{3.19}$$

If we divide iL_r and iL_p into two short and long parts as

$$\begin{aligned} iL_{short} &= \frac{\mathbf{F}_{short}}{m} \frac{\partial}{\partial \mathbf{v}} \quad , \\ iL_{long} &= \frac{\mathbf{F}_{long}}{m} \frac{\partial}{\partial \mathbf{v}} \quad , \end{aligned} \tag{3.20}$$

then with respect to equation (3.17) we can re-write the time evolution operator as

$$\begin{aligned} e^{iL\Delta t} &= e^{i(L_{short} + L_{long} + L_r)} \\ &\approx e^{iL_{long}\Delta t/2} e^{i(L_{short} + L_r)\Delta t} e^{iL_{long}\Delta t/2} \\ &= e^{iL_{long}\frac{\Delta t}{2}} \left[e^{iL_{short}\frac{\delta t}{2n}} e^{iL_r \frac{\delta t}{n}} e^{iL_{short}\frac{\delta t}{2n}} \right] e^{iL_{long}\frac{\Delta t}{2}} \end{aligned} \tag{3.21}$$

in which Δt and $\delta t = \Delta t/n$ are long and short time steps, respectively.

By using this expression we first make a step with the long range force and then we performing n small steps with short range force using the velocity Verlet algorithm.

The idea is that in the integration part of the simulation, after updating velocities with the time step Δt we introduce an inner iteration which is repeating $n = \frac{\Delta t}{\Delta t_{short}}$ times. In this inner iteration which is a multiple time step cycle, the velocities and positions will be updated via the short-range time step Δt_{short} and, after finishing this cycle, finally the velocities will be updated by long-range time step again. The point is when the positions of particles are updated due to the short-range interaction, the movement of the particle which does not feel this interaction is negligible.

The implementation of the multiple time step scheme in a MD simulation can be described by the following programming code (using FORTRAN90 syntax).

```
!MD steps
do time = 1, nsteps
!update the velocity with half of the long time step
do i = 1, npart
do j = 1, 3
vel(j,i) = vel(j,i) * 0.5 * dt * flong(j,i)
end do
end do
!n small iterations with short time step
do mts = 1, nts
!update the velocity with half of short time step
do i = 1, npart
do j = 1, 3
vel(j,i) = vel(j,i) * 0.5 * (dt / nts) * fshort(j,i)
end do
end do
!update the positions
do i = 1, npart
do j = 1, 3
pos(j,i) = pos(j,i) + (dt / nts) * vel(j,i)
end do
end do
!update the short range forces
call force_short
!update the velocity with half of short time step
do i = 1, npart
do j = 1, 3
vel(j,i) = vel(j,i) * 0.5 * (dt / nts) * fshort(j,i)
end do
end do
end do
!update long range forces
call force_long
!update the velocity with half of the long time step
do i = 1, npart
```

```
do j = 1, 3
vel(j,i) = vel(j,i) * 0.5 * dt * flong(j,i)
end do
end do
end do
```

3.6 Cell and Verlet neighbor lists

In a computer simulation, the calculation of forces and energies are the most time-consuming tasks. To overcome this non-efficiency and save time, first of all, we truncated the potential via a cut-off radius. With considering the cut-off radius r_{rcut}, we are limiting the calculation of forces and potentials to the particle which are inside a sphere with a radius of r_{rcut} with respect to a reference particle i. We determine r_{rcut} such that the pair potential and force beyond the r_{rcut} should be strictly zero. For instance when we are considering the cut-off radius of inverse power-law potential $\propto 1/r^{256}$ interaction as $r_{rcut} = 1.2\sigma$ then $u(r_{cut}) \approx 10^{-20}$.

To be more efficient, alongside the cut-off strategy, it is a good idea to consider the interaction between the reference particle i and its neighboring particles. There are some methods which are developed for CPU time saving such as Verlet list and cell list. We give a brief introduction about them and discuss their efficiency in detail.

The cell list which is also known as the linked cell list was first proposed by Hockney and Eastwood (1988). To be more clear in the case that we consider the calculations for all the pairs, then our required time to do so is in scale with N^2. The idea of this method is that we are dividing the simulation box into cells with linear dimensions of the order of the cut-off radius. By choosing a particle in any cell, this particle will interact just with the particles in the same cell or in the nearest and next-nearest neighbor cells. In a 2D simulation, the number of neighboring cells is equal to 8, and this value for a 3D is 26. Figure 3.3, shows the cell list arrangement.

Another scheme that one can use to reduce the required time to calculate the force is the Verlet neighbor list (Verlet (1967)). In this method, we introduce a radius which is called Verlet radius r_v which is about 10-20% larger than the cut-off radius of the particle-particle interaction. The particles inside this radius are making the Verlet list. During the simulation when the displacement of any particle is greater than $r_v - r_{cut}$ then one needs to update the Verlet list to be able to calculate the new forces and energies. Figure3.4, shows the Verlet list arrangement.

Moreover, if the number of particles in the Verlet list n_v is very less than the total number of particles in the simulation box N, then this scheme becomes

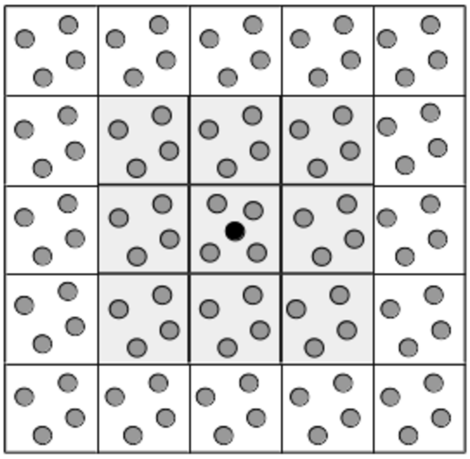

Figure 3.3: shows the cell list which indicates that the black particle is just interacting with particles in gray area. Eshraghi (2015).

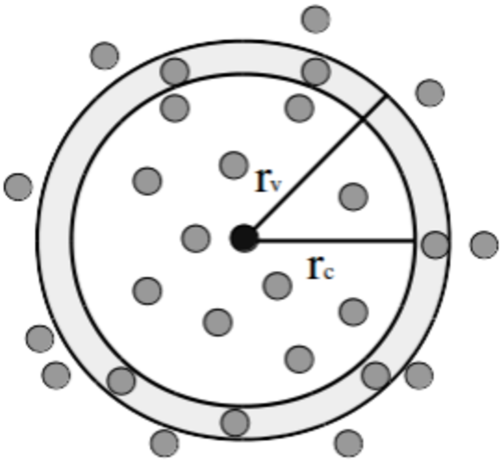

Figure 3.4: shows the Verlet list or neighbor list method. This representation indicates that we consider the interaction of the interested particle with the particles in the circle with radius rv Eshraghi (2015).

more efficient. In 3D simulation, the number of particles in the Verlet list can be defined as (Frenkel and Smit (2001))

$$n_v = \frac{4}{3}\pi r_v^3 \rho \quad . \tag{3.22}$$

Here, ρ is the number density of the system. With a typical value of hard-core Yukawa at coexistence with $\rho = 0.26087$, the number of particles in the Verlet list can be calculated as $n_v \approx 570$. Thus, it does make sense to use this method for $N > 1000$. For the cell list, the number of particles in the list can be calculated as

$$n_l = 27 \rho r_{cut}^3 \tag{3.23}$$

In our case, the number of particles in the cell list is $n_l \approx 2415$, i.e., around four times larger than the one for the Verlet list. Frenkel and Smit (2001) showed that the number of pairs that should be considered in Verlet list is around 16 times smaller than the one in the cell list which makes it more efficient than the cell list.

By considering the efficiency of the Verlet list in energy calculations, Auerbach, Paul, et al. (1987) developed a method that constructs a Verlet list by using a cell list (figure 3.5). The idea in this combined scheme is that like the cell list method we divide the simulation box into equal cells, but at the same time like the Verlet list we introduce the Verlet radius, and the final list consists of the particles which are common in these cells and the Verlet radius. This means that each particle interacts with the particles that are in the same and neighboring cells and also within the Verlet radius. Moreover, updating of this list is same as Verlet list.

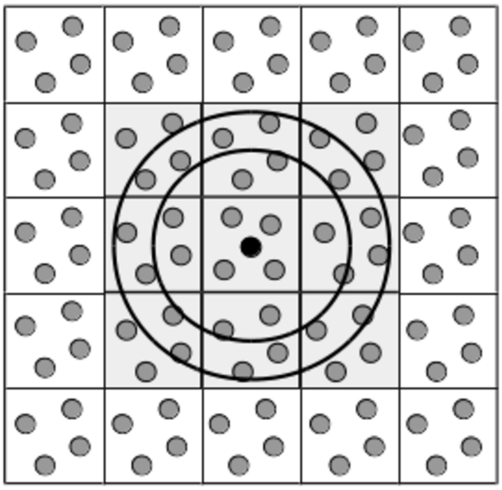

Figure 3.5: shows the combination of Verlet and cell list methods. In this combination consider all particles which are in cell list, but they should be in Verlet radius as well. Eshraghi (2015)

4 Calculation Of Interfacial Free Energy

For a system in the canonical NVT ensemble, i.e., with constant particle number N, volume V, and temperature T, one can define the Helmholtz free energy F as

$$F \equiv E - TS \tag{4.1}$$

in which E is the energy of the system and S denotes the entropy. The thermodynamic potential in the NPT ensemble, i.e., at constant pressure P, is the Gibbs free energy G that can be written as

$$G \equiv F + PV \quad . \tag{4.2}$$

Let's consider a first order phase transition (Kurt Binder (1987)) at a constant temperature T. Then, one can observe a discontinuous change of the entropy S at this temperature which is associated with the production of latent heat L as

$$L = T\Delta S \quad . \tag{4.3}$$

Thus, at the first-order phase transition there is a discontinuity of the derivatives of the Gibbs free energy G, the entropy being one example

$$S = -\left(\frac{\partial G}{\partial T}\right)_{N,P} \tag{4.4}$$

Also, the volume V given by

$$V = \left(\frac{\partial G}{\partial P}\right)_{N,T}, \tag{4.5}$$

might be discontinuous at the transition. As an example, one can consider the solid-liquid and liquid-gas transition as first order transitions.

Consider two phases as phase A and phase B, and one can write their free energy as F_A and F_B, respectively. So by comparing the free energy of these two phases, we can understand how stable they are. The first step to calculate the free energy difference ΔF is the computation of the ensemble average. Let's consider a system of N particles and observable $A(\vec{r}_1, \vec{r}_2, \cdots, \vec{r}_N)$, so the expectation value of this observable can be written as

$$\left\langle A\left(\vec{r}^{(N)}\right)\right\rangle = \frac{\int d\vec{r}^{(N)} A\left(\vec{r}^{(N)}\right) \exp\left(-\beta U\left(\vec{r}^{(N)}\right)\right)}{\int d\vec{r}^{(N)} \exp\left(-\beta U\left(\vec{r}^{(N)}\right)\right)} \quad . \tag{4.6}$$

But the direct calculation of this high dimensional integral in general is not possible. As an example in classical statistical mechanics, one can define the Helmholtz free energy F as

$$F = -k_B T \ln Q\left(N, V, T\right) \tag{4.7}$$

in which $Q\left(N, V, T\right)$ is the canonical partition function which is given by

$$Q\left(N, V, T\right) = \frac{\int d\vec{p}^N d\vec{r}^N \exp\left[-\beta \mathcal{H}(\vec{p}^N, \vec{r}^N)\right]}{h^{dN} N!} \tag{4.8}$$

where h is the Planck constant, $\mathcal{H}$ is the Hamiltonian, $\beta = \frac{1}{k_B T}$, and $\vec{r}$ and $\vec{p}$ represent positions and momenta, respectively (Pathria and Beale (2012)). In a simulation, it is not possible to directly calculate the free energy, entropy, and related quantities because they are not the averages of the functions of the coordinates of the system and the canonical partition function cannot be written as a canonical average over phase space.

In an experiment, one can determine the derivative of the free energy with respect to the temperature T and the volume V. One can write the partial derivative of the Helmholtz free energy F with respect to the volume V at constant number of particles N and temperature T as follows

$$\left(\frac{\partial F}{\partial V}\right)_{N,T} = -P \quad . \tag{4.9}$$

On the other hand, we can define the partial derivative of Helmholtz free energy F regarding the temperature T in a system with a fixed number of particles N and volume V as

$$\left(\frac{\partial F/T}{\partial 1/T}\right)_{N,V} = -E \quad . \tag{4.10}$$

Note that the outcome of equations (4.9) and (4.10) are now mechanical quantities and one can calculate them via a simulation (Frenkel and Smit (2001)).

The interfacial free energy γ is the contribution to the free energy of a system of the particles to form an interface which is separating to different phases from each other. The calculation of the interfacial free energy between a crystal and a fluid as well as between crystal or fluid and walls plays a key role for the understanding of wetting phenomena (De Gennes (1985) and de, Brochard-Wyart, and Quere (2004)) as well as heterogeneous nucleation (Dietrich (1988)). Experimental Calculation of interfacial free energy is a hard task to do, but some few studies by Navascues (1979), Glicksman and Singh (1989) and Howe (1997) have calculated the solid-solid, solid-vapor and solid-liquid interfacial free energy.

Due to this lack of experimental data on the interfacial free energy, analytical and computer simulation techniques have been used to calculate the interfacial free energy for different physical systems. In this chapter, we will briefly discuss thermodynamic integration method to calculate free energy differences of a given system of particles, and finally, we will describe the method that we are using to calculate interfacial free energies regarding confinements.

4.1 Thermodynamic Integration

Assume that we want to calculate the free energy of a system of N particles at a given temperature T and number density ρ. The thermodynamic integration (TI) method is a scheme to calculate the free energy difference between a reference phase or state and the final phase or state that we are interested to study. To calculate the energy difference between initial and final state by tuning the thermodynamic parameters, the system will take a path which connects these two states from initial state to the state of interest such that in each point of the path system is in equilibrium, therefore, this path can be reversible (Callen (1998)).

Kirkwood and Buff (1949) proposed a formalism for parameterization of the potential function to calculate the free energy difference. Here, for a system of N particles and potential energy function U we assume that this potential function has a linear relationship with the coupling parameter λ. If we consider our reference system as A and the desired one as B, then we can assume their potential energy function as u_A and u_B, respectively. So, based on the Kirkwood formalism, one can write the λ-dependent potential energy function of the path between states A and B as

$$U\left(\vec{r}^{(N)}, \lambda\right) = (1 - \lambda)\, U_A(\vec{r}^{(N)}) - \lambda U_B(\vec{r}^{(N)}) \tag{4.11}$$

The corresponding partition function for such a system can be written as

$$Q\left(N, V, T, \lambda\right) = \frac{1}{\Lambda^{3N} N!} \int d\vec{r}^{(N)} \exp\left[-\beta U\left(\vec{r}^{(N)}, \lambda\right)\right] \tag{4.12}$$

where $\beta = 1/k_B T$ and $\Lambda = h\sqrt{\frac{\beta}{2\pi m}}$ is the de Broglie wavelength (with m the mass of the particles). One can derive the derivative of the λ-dependent Helmholtz free energy $F(\lambda)$ for a system of N particles and with fixed volume V and temperature T as

$$\begin{aligned}\left(\frac{\partial F(\lambda)}{\partial \lambda}\right)_{N,V,T} &= -\frac{1}{\beta}\frac{\partial}{\partial \lambda}\ln Q(N,V,T,\lambda) \\ &= \frac{1}{\beta Q(N,V,T,\lambda)}\frac{\partial Q(N,V,T,\lambda)}{\partial \lambda} \\ &= \frac{\int d\vec{r}^{N}\left(\frac{\partial U(\lambda)}{\partial \lambda}\right)\exp\left[-\beta U(\lambda)\right]}{\int d\vec{r}^{N}\exp\left[-\beta U(\lambda)\right]} \\ &= \left\langle \frac{\partial U(\lambda)}{\partial \lambda}\right\rangle_{\lambda}\end{aligned} \tag{4.13}$$

in which $\langle \cdots \rangle_\lambda$ denotes the ensemble average over λ. Now one can write the free energy difference between states A and B as

$$\Delta F(\lambda) = F(\lambda = 1) - F(\lambda = 0) = \int_{\lambda=0}^{\lambda=1} d\lambda \left\langle \frac{\partial U(\lambda)}{\partial \lambda}\right\rangle_{\lambda} \tag{4.14}$$

Now we have the free energy difference regarding an ensemble average which we can calculate directly via a simulation.

Heni and Löwen (1999) employed square-barrier and triangular cleaving potentials to perform the thermodynamic integration and calculate the interfacial free energy of a hard sphere fluid in contact with a flat hard wall. They have also completed the same process to calculate the interfacial free energy of an FCC crystal with (111), (100), and (110) orientations. However, due to the pre-freezing at coexistence density, they have to calculate the value for fluid-wall interfacial free energy via an extrapolation from lower densities to the coexistence density.

Fortini and Dijkstra (2006) improved the calculation of Heni and Löwen (1999) by using an exponential barrier function beside the square-barrier one to perform the thermodynamic integration. They have calculated the fluid-wall interfacial free energy of hard sphere fluids as well as crystal-wall interfacial free energy for the hard sphere crystals with (111) and (100) orientations, however, the calculation was for the densities below the bulk coexistence density. However, using this scheme they were not able to distinguish between partial and complete wetting.

To calculate the interfacial free energy between crystal and liquid of Lennard-Jones system, Davidchack and Laird (2003) have applied a thermodynamic integration scheme by using the cleaving wall method. To obtain a reversible thermodynamic path, they have divided the bulk crystal by a cleaving potential (wall), but both parts of the system have interaction with each other via periodic boundary conditions. The same setting is also done for the fluid. In the next step by keeping the cleaving walls, they have put each part of the crystal in one side of the fluid and gradually removed the walls. So the crystal-liquid interfacial free energy is proportional to the total work that has been done to perform these steps.

By considering Lennard-Jones fluid and crystal with (111) orientation which are confined between structured walls, Benjamin and Horbach (2012) proposed a modified thermodynamic integration to compute the free energy of fluid-wall and crystal-wall interfaces. As the first step, they have considered a reversible thermodynamic path from a bulk Lennard-Jones system to a state where these systems are in contact with structureless flat walls. In the second step, they transformed the structureless walls into structured walls which are formed by the crystal particles. These steps has been done via NPT ensemble, and by considering a λ-dependent Hamiltonian for these systems, they were able to calculate the Gibbs free energy difference ΔG between initial and final state of the thermodynamic path. By using Gibbs free energy difference ΔG they could calculate the interfacial free energy for Lennard-Jones fluids and crystals in contact with structured walls.

4.2 Present Work

In this work we have used Benjamin and Horbach (2012), Benjamin and Horbach (2014a) and Benjamin and Horbach (2015) approach , but the λ parameterization of the Hamiltonian is changed with respect to the requirements of the hard-core Yukawa systems. In the following, we explain our approach in detail.

4.2.1 *Fluid-Wall And Crystal-Wall Interfacial Free Energy*

To calculate the interfacial free energy of the fluid, FCC and BCC crystals with (111) orientation we have used a reversible and smooth thermodynamic path from a bulk fluid, FCC or BCC ($\lambda = 0$) to the system which is confined by a pair of flat structureless hard/charged walls ($\lambda = 1$).

Through this smooth and reversible path, we need to gradually turn on the interaction of the bulk particles with the walls and at the same time turn off the periodic boundaries in the direction of flat walls. To this end, we need to parameterize the Hamiltonian of the system. Let's consider a system of N particles in a volume V, and at temperature T. Then one can write the Hamiltonian of such system as

$$\mathcal{H}(\lambda) = \sum_{i=1}^{N} \frac{\vec{p}_i^{\,2}}{2m_i} + \sum_i \sum_{j \neq i} u_{ij} \tag{4.15}$$

in which u_{ij} describes the interaction between particle i and particle j. To obtain our desired thermodynamic integration path, we should parameterize the Hamiltonian such that $\lambda = 0$ corresponds to the system with periodic boundary condition and $\lambda = 1$ to the system confined between two walls. Now, the λ-dependent Hamiltonian of the system can be written as

$$\mathcal{H}(\lambda) = \sum_{i=1}^{N} \frac{\vec{p}_i^2}{2m_i} + U_{p-p} + U_{p-im}(\lambda) + U_{p-fw}(\lambda) \tag{4.16}$$

in which U_{p-p} is the total potential energy of the particle-particle in the bulk, U_{p-i} is the total potential energy with respect to interaction of the bulk particles with the ones which are in the other side of the wall (image particles), and this interaction is due to the periodic boundary condition and U_{p-fw} is the total potential energy due to the interaction between particles and flat walls.

By turning off the periodic boundary condition and turning on the flat wall interaction, we can parameterize U_{p-i} and U_{p-fw} as follows

$$U_{p-i}(\lambda) = (1-\lambda)^l U_{p-i} \tag{4.17}$$

$$U_{p-fw}(\lambda) = \lambda^m \left(\frac{1+\lambda}{2}\right)^n U_{p-w} \tag{4.18}$$

in which l, m and n are parameters which control the smoothness of the thermodynamic path. The free energy difference between bulk ($\lambda = 0$) and confined ($\lambda = 1$) states can be derived as

$$\frac{\partial \mathcal{H}}{\partial \lambda} = \frac{\partial U_{p-i}(\lambda)}{\partial \lambda} + \frac{\partial U_{p-fw}(\lambda)}{\partial \lambda}$$

$$\Delta F = \int_0^1 \left\langle \frac{\partial \mathcal{H}}{\partial \lambda} \right\rangle_\lambda d\lambda \tag{4.19}$$

So one can calculate the interfacial free energy of the fluid and crystal in contact with the flat walls as

$$\gamma = \frac{\Delta F}{A} \tag{4.20}$$

in which $A = 2L_xL_y$ is the total area of the interface.

4.2.2 *Fluid-Crystal Interfacial Free Energy*

If we consider a crystal which is growing from its melt, then the calculation and determination of the interfacial free energy between a crystal and its melt, γ_{cf}, plays an important role for the rate of this growth (Turnbull (1952)) and also for the wetting behavior of the growing crystal.

In many studies, the thermodynamic integration method (TI) has been used to calculate the interfacial free energies between a crystal and a fluid. Broughton and Gilmer (1986) performed a thermodynamic integration method for a system of particles which are interacting with a modified Lennard-Jones potential to calculate the crystal-fluid interfacial free energy γ_{cf}. They separated crystal and fluid into two parts by inserting a modified cleaving wall. After bringing these two systems together, they removed the cleaving wall and calculated the crystal-fluid interfacial free energy γ_{cf}. Their method is not general and requires the different modification of a cleaving wall for any orientation of the crystal.

Instead of using a flat cleaving wall, Davidchack and Laird (2000) employ structured cleaving walls which are made of several crystalline layers of frozen particles. Their calculation was more accurate than Broughton and Gilmer (1986) and could solve the anisotropy issue in the calculation of crystal-fluid interfacial free energy γ_{cf}.

Both the above mentioned thermodynamic integration methods to calculate crystal-fluid interfacial free energy γ_{cf}, have a common step in which after bringing the crystal and fluid together, they tried to remove the cleaving walls gradually. However, this removal led to a hysteresis which means because of the thermal fluctuations the position of the crystal and fluid can change and they can freeze and melt at the same time. So, this means that the path is not completely reversible since the position of the fluid and crystal will not match with the initial position of the cleaving walls.

To overcome these issues, Benjamin and Horbach (2014b) proposed a thermodynamic integration scheme to calculate the crystal-fluid interfacial free energy γ_{cf} for a system of particles interacting via a Lennard-Jones potential. The same method is also employed to calculate the crystal-fluid interfacial free energy γ_{cf} for a system of hard spheres (Benjamin and Horbach (2015)). In the following, we are describing this method and will explain how they overcome the issue of the movement of the crystal-fluid interface. In this work, we are using the same approach to calculate the crystal-fluid interfacial free energy γ_{cf} for the hard-core Yukawa system. This method can be categorized into six steps as follows:

Step 1: In this step, to avoid the movement of the crystal-fluid interface, we are confining the fluid by a pair of flat and structureless short-range Gaussian walls. We put these walls at the end of the fluid system in z-direction such that the bulk particles cannot leave the box. Note that the range of the Gaussian wall should be such that its contribution to the interfacial free energy is small. We gradually switch on the interaction between particles and Gaussian walls, but the periodic boundary condition is on for the whole step. The Hamiltonian of the system for this step can be written as

$$\mathcal{H}_1(\lambda) = \sum_{i=1}^{N} \frac{\vec{p}_i^{\,2}}{2m_i} + U_{p-p} + U_{p-im}(\lambda) + U_{p-fw}(\lambda) \tag{4.21}$$

where

$$U_{p-fw}(\lambda) = \lambda^m U_{p-fw} \tag{4.22}$$

describes the total potential energy due to the interaction of particles with flat Gaussian walls.

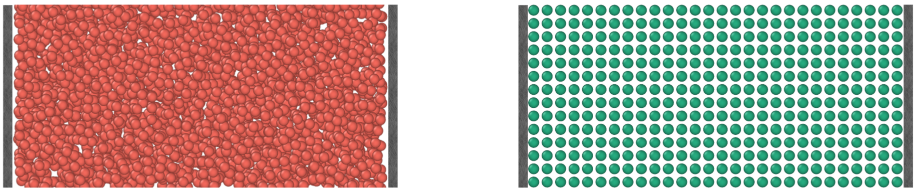

(a) Step 1 (b) Step2

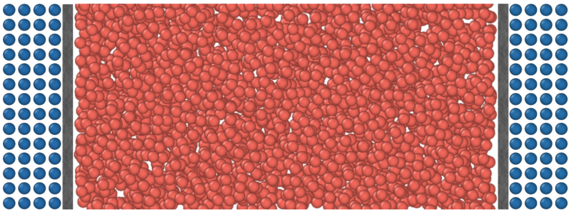

(c) Step3

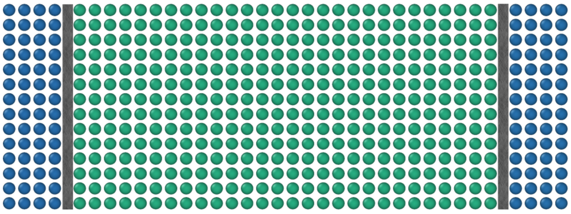

(d) Step4

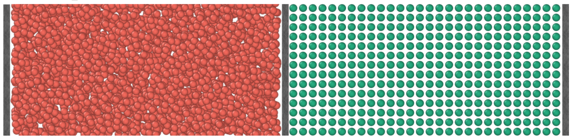

(e) Step5

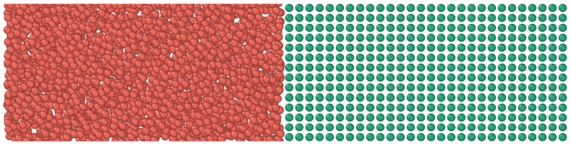

(f) Step6

Figure 4.1: shows the thermodynamic integration step to calculate the crystal-fluid interfacial free energy.

Step 2: This step is same as step one, but here we are confining the FCC or BCC crystals by a pair of extremely short-range Gaussian walls. So one can write the Hamiltonian as

$$\mathcal{H}_2\left(\lambda\right) = \sum_{i=1}^{N} \frac{\vec{p}_i^{\,2}}{2m_i} + U_{p-p} + U_{p-im}\left(\lambda\right) + U_{p-fw}\left(\lambda\right) \tag{4.23}$$

where

$$U_{p-fw}\left(\lambda\right) = \lambda^m U_{p-fw} \quad . \tag{4.24}$$

Step 3: In this step, we construct a structured wall from several layers of the crystal in the last part of step 2. Then we take the fluids from step 1 and gradually confine them with the structured walls, and in the meantime we are turning off the periodic boundaries in the direction of the walls. However, the Gaussian wall still is remaining to prevent the fluid particles from leaving the box. One can write the Hamiltonian of this step as follows

$$\mathcal{H}_3(\lambda) = \sum_{i=1}^{N} \frac{\vec{p}_i^2}{2m_i} + U_{p-p} + U_{p-i}(\lambda) + U_{p-pw}(\lambda) + U_{f-w} \tag{4.25}$$

in which

$$U_{p-i}(\lambda) = (1-\lambda)^n U_{p-i} \tag{4.26}$$

describes the total potential energy with respect to the interaction of the bulk particles with image particles. Moreover, the total potential energy with respect to the interaction of particles with structured walls can be defined as

$$U_{p-pw}(\lambda) = \lambda^p U_{p-pw} \quad . \tag{4.27}$$

Step 4: This step is same as step 3, but we are confining the crystals from step 2 between the structured walls. So we can write the λ-dependent Hamiltonian as

$$\mathcal{H}_4(\lambda) = \sum_{i=1}^{N} \frac{\vec{p}_i^2}{2m_i} + U_{p-p} + U_{p-i}(\lambda) + U_{p-pw}(\lambda) + U_{p-fw} \tag{4.28}$$

in which

$$U_{p-i}(\lambda) = (1-\lambda)^n U_{p-i} \tag{4.29}$$

and

$$U_{p-pw}(\lambda) = \lambda^p U_{p-pw} \quad . \tag{4.30}$$

Step 5: In this step, we need to bring fluid and crystal together. To this end, we need to turn on the fluid-crystal interaction gradually and in the meantime turn off the interaction of each phase with the structured walls. So we can write the Hamiltonian of this step as

$$\mathcal{H}_5(\lambda) = \sum_{i=1}^{N} \frac{\vec{p}_i^2}{2m_i} + U_{p-p}^{c(l)} + U_{p-p}^{c+l}(\lambda) + U_{p-pw}^{c(l)}(\lambda) + U_{p-fw} \tag{4.31}$$

in which

$$U_{p-pw}^{c(l)}(\lambda) = (1-\lambda)^n U_{p-pw} \tag{4.32}$$

and

$$U_{p-p}^{c+l}(\lambda) = \lambda^p U_{p-p}^{c+l} \quad . \tag{4.33}$$

Here, $U_{pp}^{c+l}(\lambda)$ describes the total potential energy due to the interaction of crystal and fluid.

Step 6: Now it is time to remove the Gaussian walls and letting the liquid-crystal system to relax. So we are gradually removing the Gaussian walls from each side of the fluid and crystal phases as

$$\mathcal{H}_6(\lambda) = \sum_{i=1}^{N} \frac{\vec{p}_i^2}{2m_i} + U_{p-p}^{c(l)} + U_{p-fw}(\lambda) \tag{4.34}$$

in which

$$U_{p-fw}(\lambda) = (1-\lambda)^m U_{p-fw} \quad . \tag{4.35}$$

Figure 4.1 shows these six steps of the modified thermodynamic integration method. The free energy difference of each step can be calculated via

$$\Delta F_i = \int_0^1 \left\langle \frac{\partial \mathcal{H}_i}{\partial \lambda} \right\rangle d\lambda, \tag{4.36}$$

and the interfacial free energy can be calculated as

$$\gamma = \frac{\Delta F_1 + \Delta F_2 + \Delta F_3 + \Delta F_4 + \Delta F_5 + \Delta F_6}{A} \tag{4.37}$$

in which $A = 2L_x L_y$ is the total area of the interface.

5 Local Bond Order Parameters

One of the main outcomes of a computer simulation are the configurations which are describing the position of the particles in each state of the simulations. In our case of study we are interested to investigate the behavior of inhomogeneous structures in confinement and characterize local order around each particles in these systems. To analyze the structures of different systems confined between a pair of hard walls or charged walls, we have used the local bond order parameters. These parameters allow to distinguish between FCC, BCC and fluid local ordering around a particle. In this study, we have considered three different approaches to analyze the structure of the hard-core Yukawa systems in confinement which will be discussed below in detail.

The starting point of the calculation of local bond order parameters is to identify the neighboring particles of each particle inside the system. To minimize the effort we are considering $N_b(i)$ nearest neighbors around particle i by a cut-off radius which we can extract from the first minimum of the radial distribution function $g(r)$. The radial distribution function $g(r)$ describes the probability of finding a particle at distance r from a reference particle relative to the corresponding case in an ideal gas. This quantity is defined by

$$g\left(r\right) = \frac{V}{N^2 4\pi r^2} \left\langle \sum_{i=1}^{N} \sum_{j=1, j\neq i}^{N} \delta\left(r - |\mathbf{r}_i - \mathbf{r}_j|\right) \right\rangle \tag{5.1}$$

in which $\mathbf{r}_i$ and $\mathbf{r}_j$ represent the position of particles i and j, respectively, and $\langle \cdots \rangle$ stands for time or ensemble average. Figure 5.1 shows the radial distribution function $g(r)$ for different phases in the presence of a pair of flat hard walls.

By considering $N_b(i)$ nearest neighbors, one can do an expansion into spherical harmonics Y_{lm} and define a parameter $\bar{Q}_{lm}(i)$ for particle i as

$$\bar{Q}_{lm}(i) = \frac{1}{N_b(i)} \sum_{j=l}^{N_b(i)} Y_{lm}(i) \left(\hat{r}_{ij}\right) \tag{5.2}$$

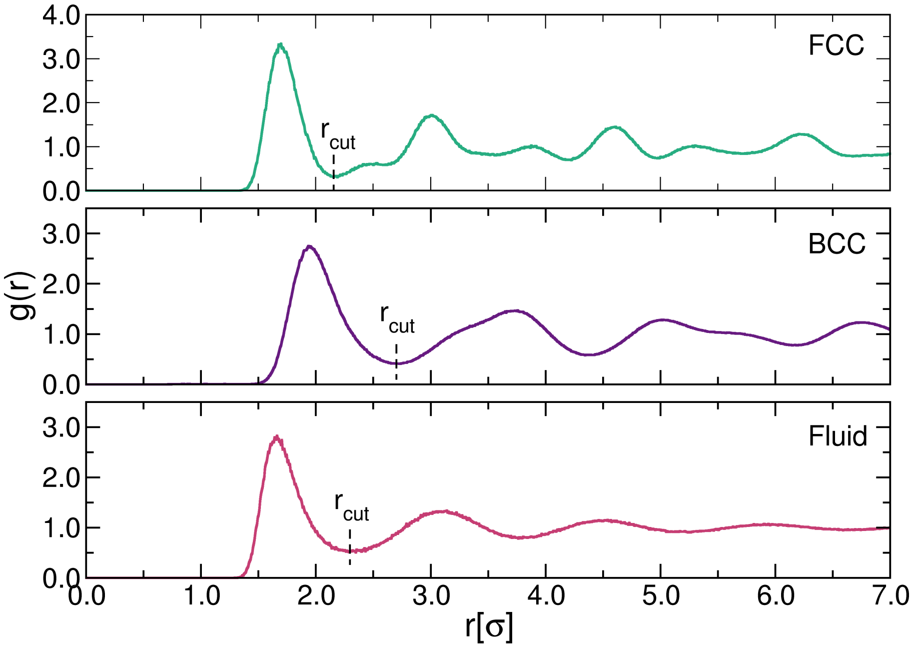

Figure 5.1: shows the radial distribution function $g(r)$ for three different systems as FCC ($\eta = 0.1397$) , BCC ($\eta = 0.0900$) and fluid ($\eta = 0.1366$) in contact with a pair of flat hard walls.

where $m \in [-l, l]$ is an integer parameter and, $\hat{r}_{ij}$ represents the unit distance vector between particles i and j. Steinhardt, Nelson, and Ronchetti (1983) suggested a rotationally invariant combination of $\bar{Q}_{lm}(i)$ as follows

$$Q_l(i) = \left(\frac{4\pi}{2l+1} \sum_{m=-l}^{l} \left| \bar{Q}_{lm}(i) \right|^2 \right)^{1/2} \quad . \tag{5.3}$$

From this equation one can calculate the order parameters Q_4 and Q_6 which can help us to distinguish between solid structures and fluid systems. For this purpose we can produce a $Q_4 - Q_6$ map and based on that we can identify the structure of each particle in the system.

Later on, Ten Wolde, Ruiz-Montero, and Frenkel (1995) argued that the above approach of the global order parameters is not completely useful for solid-like structures because due to the incoherently adding up of $\bar{Q}_{lm}(i)$ in the fluid a global order parameter Q_6 can be vanished. This means that the single value of Q_6 which assigned to all particles to identify the structure of whole system becomes zero. So they proposed an approach to calculate the local order parameter as

$$\tilde{q}_{lm}(i) = \frac{\bar{Q}_{lm(i)}}{\left(\sum_{m=-l}^{l} \left| \bar{Q}_{lm}(i) \right|^2 \right)^{1/2}} \tag{5.4}$$

Then one can calculate the product of this local parameter as

$$q_l q_l(i) = \frac{1}{N_b(i)} \sum_{j=l}^{N_b(i)} q_l(i) \cdot q_l(j) \tag{5.5}$$

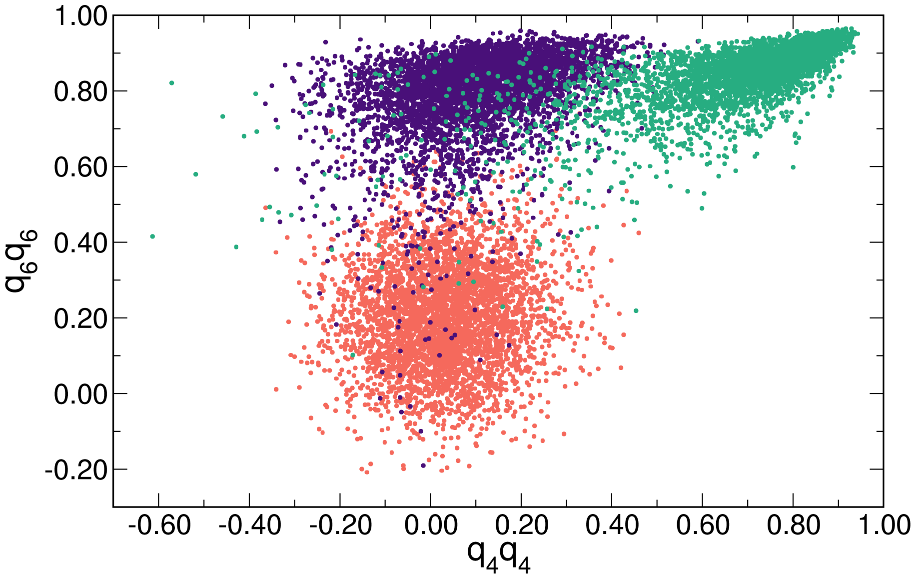

Figure 5.2: shows the $q_4q_4 - q_6q_6$ plain (Ten Wolde, Ruiz-Montero, and Frenkel (1995)) which is used to distinguish between bulk phases in hard-core Yukawa system of particles. The green part indicated the particles with FCC structure, purple part belongs to the BCC structure and light magma points shows the fluid phase. This plain is made by the first minimum of radial distribution function $g(r)$ as cut-off for considering the neighbors. The bulk systems in this figure are correspond to the densities of figure 5.1

where the internal product $q_l(i) \cdot q_l(j)$ can be expressed as

$$q_l(i) \cdot q_l(j) = \sum_{m=-l}^{l} \tilde{q}_{lm}(i)\tilde{q}^*_{lm}(j) \tag{5.6}$$

in which $\tilde{q}^*_{lm}$ is the conjugate complex of $\tilde{q}_{lm}$. So if this dot product reaches some specified value then one can say particle i and j are connected.

On the other hand, by calculating the local parameters such as q_4q_4 and q_6q_6 we can produce a $q_4q_4 - q_6q_6$ map (see figure 5.2). In other words, we consider bulk phases of BCC, FCC and fluid configurations and assign a point to each particle in these systems in the $q4q4 - q6q6$ map. This map is created based on the first shell of neighbors. Now if we also consider the second neighbor shell using a cut-off corresponding to the second minimum of radial distribution function $g(r)$, we will end up with another map which is presented in figure 5.3. Each phase in these maps is presented as a separated island which enables us to distinguish between the three different phases.

Another approach which has been widely used has been proposed by Lechner and Dellago (2008). They have shown that by using the following equations (eq. (5.7), and eq. (5.8)) the calculated values for q_4 and q_6 parameters is not enough to distinguish between different structures.

$$q_l(i) = \left(\frac{4\pi}{2l+1} \sum_{m=-l}^{l} |q_{lm}(i)|^2 \right)^{1/2} \tag{5.7}$$

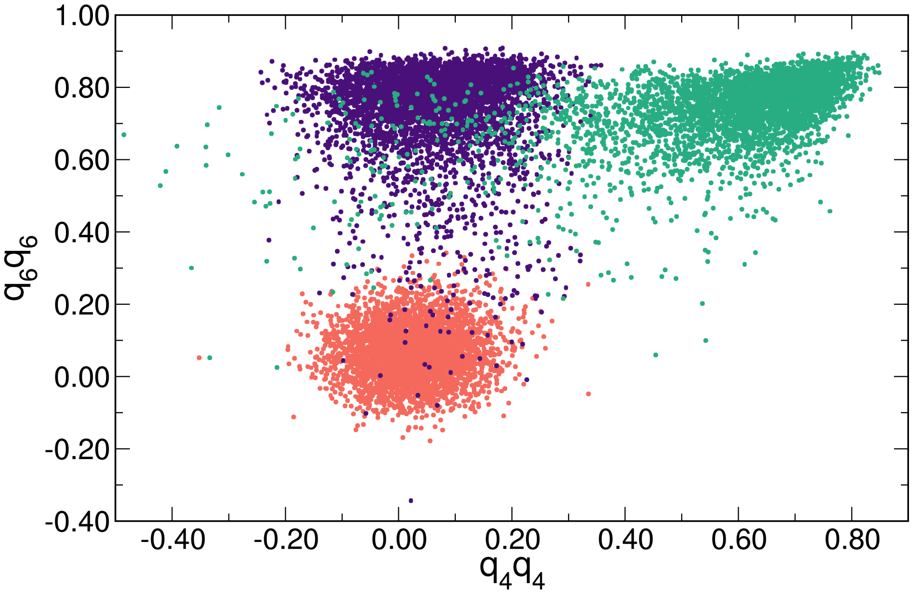

Figure 5.3: illustrates the $q_4q_4 - q_6q_6$ map (Ten Wolde, Ruiz-Montero, and Frenkel (1995)) calculated by considering the second minimum of radial distribution function for the bulk hard-core Yukawa systems with different phases. This pain is almost similar to the figure 5.2 which indicates that the first minimum of $g(r)$ is already a good choice for the neighborhood cut-off. The bulk systems in this figure are correspond to the densities of figure 5.1

where

$$q_{lm}(i) = \frac{1}{N_b(i)} \sum_{j=0}^{N_b(i)} Y_{lm}(\mathbf{r}_{ij}) \quad . \tag{5.8}$$

In other words, these local bond order parameters or Steinhardt order parameters are more useful in the case that one wants to distinguish between hexagonal and cubic structures. In figure 5.4, we have shown that a $q_4 - q_6$ map with the consideration of the first nearest neighbor shell is not sufficient to identify the structure of a system with three different phases. Even using second sell of neighboring particle did not help to get a better separation of the phases in the $q_4 - q_6$ map as one can see in figure 5.5. The second approach is slightly better than the last one but it is still not enough to give a clear separation between the phases.

So they have suggested that one can improve this distinguishing process via calculating the average of local bond order parameters. This average is defined as

$$\bar{q}_l(i) = \left(\frac{4\pi}{2l+1} \sum_{m=-l}^{l} |\bar{q}_{lm}(i)|^2 \right)^{1/2} \tag{5.9}$$

with

$$\bar{q}_{lm}(i) = \frac{1}{\tilde{N}_b(i)} \sum_{k=0}^{\tilde{N}_b(i)} q_{lm}(k) \quad . \tag{5.10}$$

The idea is to consider not only the particles which are the neighbors of particle i, but also one should consider the particle i as well. This method is similar to

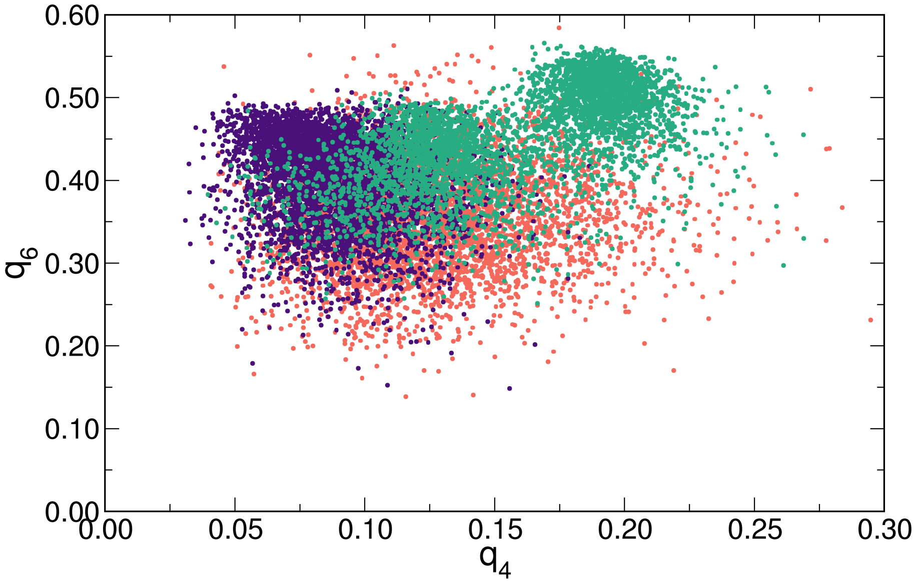

Figure 5.4: shows the $q_4 - q_6$ plain as a reference to determine the structure of the configurations with respect to the first shell of neighbors. As one can see in the case of hard-core Yukawa particles the local order parameters q_4 and q_6 are not a good choice to distinguishing between the structures. The bulk systems in this figure are correspond to the densities of figure 5.1

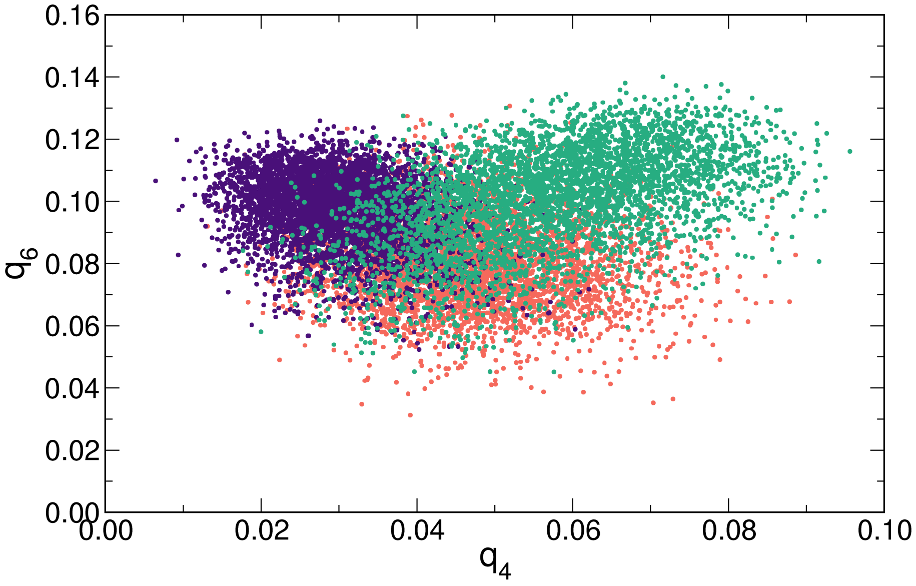

Figure 5.5: shows the $q_4 - q_6$ map of the local bond order parameters with respect to the second neighbors of hard-core Yukawa particles. Here we can observe that even by correcting the neighbor list of particles one can not rely on the local bond order parameters q_4 and q_6 which is also proven by Lechner and Dellago (2008). The bulk systems in this figure are correspond to the densities of figure 5.1

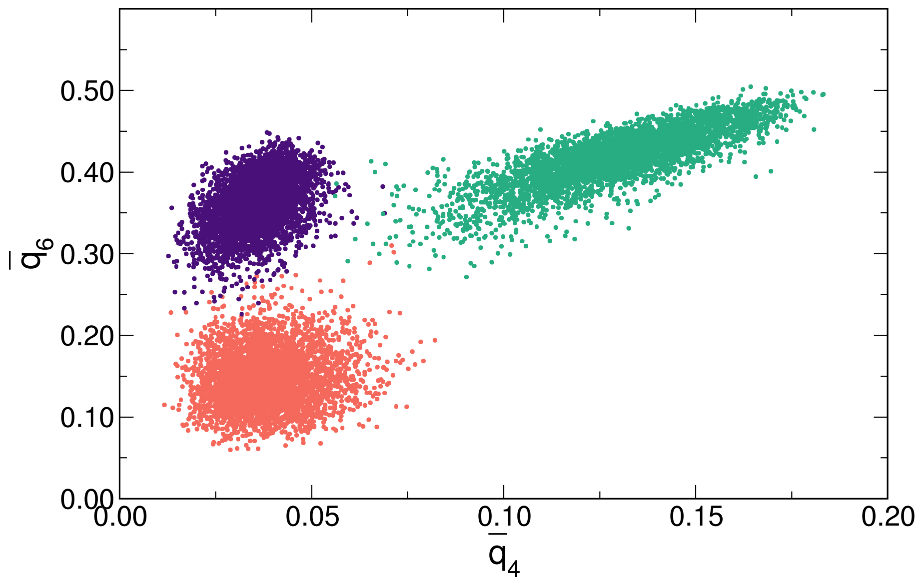

Figure 5.6: shows the calculated $\bar{q}_4 - \bar{q}_6$ map for hard-core Yukawa system of particles regarding the first minimum of $g(r)$ as cut-off. The resulted plain indicates that with respect to this map one can easily determine the structure of a given configuration at bulk via the average local bond order parameters $\bar{q}_4$ and $\bar{q}_6$. The bulk systems in this figure are correspond to the densities of figure 5.1

the one that is introduced in equation (5.10) but it already took the second shell of the neighbors into account. Figure 5.6 shows that if we just consider the first minimum of the radial distribution function $g(r)$ as the cut-off for calculation of the averaged local bond order parameter, it does already exhibit a good separation between different phases. But with changing of the cut-off from the first to the

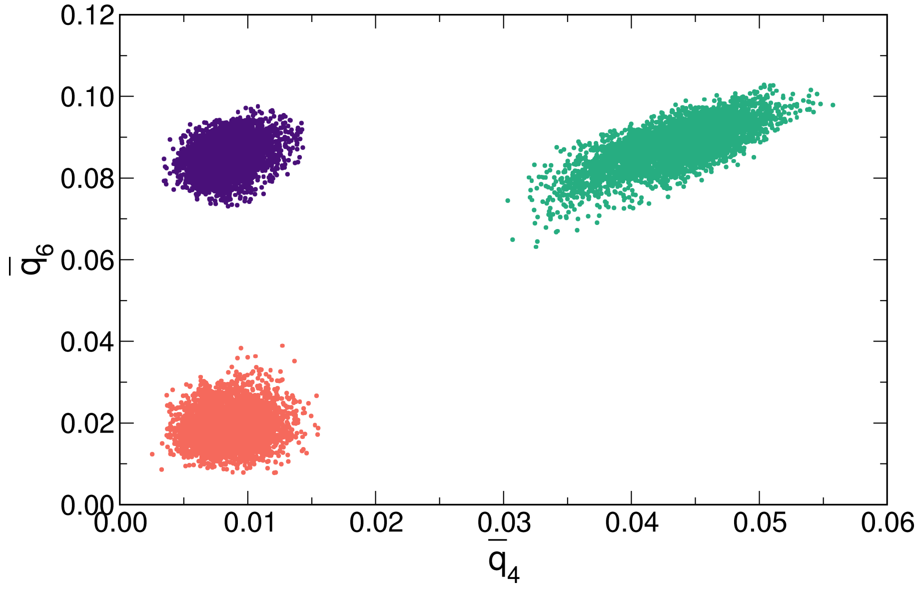

Figure 5.7: shows the $\bar{q}_4 - \bar{q}_6$ by considering the second shell of the neighbors as the cut-off. This plot proves that by considering the average local bond order parameters $\bar{q}_4$ and $\bar{q}_6$ and focusing on the second neighboring shell one can have clear vision about the structure of a given configuration. The bulk systems in this figure are correspond to the densities of figure 5.1

second minimum of the radial distribution function $g(r)$ (figure 5.7), same as the original idea of Lechner and Dellago (2008), it is even easier to determine the structure of the configuration.

5.1 Distinguish Between Structures Via Machine Learning (ML)

From the above description of local bond order parameter, we are able to make $\bar{q}_4 - \bar{q}_6$ and $q_4q_4 - q_6q_6$ planes which help us to determine the structure of different configurations. As it is possible to see from figures 5.2, 5.6 and 5.7 it is possible to distinguish between different bulk phases. But, as discussed in chapter 6, we are dealing with systems in confinement and if there is some transition and interfaces in these type of systems, then distinguishing between structures is not that easy. Based on the $\bar{q}_4 - \bar{q}_6$ and $q_4q_4 - q_6q_6$ maps one can make some cut-off to determine the structures by hand, so it is also not unique and depends on the definition of this criterion one can assign FCC, BCC or fluid order to a particle.

Now, we demonstrate that one can also use computer science techniques to deal with this issue. A field of computer science that can help us to overcome this problem is called machine learning (ML) which is described by the statement that is proposed by Samuel (1959) as the ability of a computer system to learn the pattern of a data set with no needs to be programmed. The machine learning algorithm can be divided two supervised and unsupervised learning categories (Russell and Norvig (2016)). In supervised learning, one does have a target variable which will be predicted through the given independent set of variables. The most common supervised learning algorithm are regression methods like linear regression and logistic regression, decision tree, random forest and K-nearest neighbors (KNN).

We can use the regression and other supervised machine learning algorithms when we have a clear target, and we want to optimize a lot of labeled data based on this target. But here we need to use a technique to explore the pattern within a data set that doesn’t have any clear target value.

Here we want to categorize our data set into several clusters (see fig. 5.8) . This type of learning is called unsupervised learning. There are multiple ways of clustering data but our focus is on centroid based clustering. This clustering algorithm works well when the clusters resemble circles with centers (or centroids) and the centroid represents the arithmetic mean of all of the data points in that cluster. One of the most common used and popular centroid based clustering algorithm is called K-means clustering which is proposed by MacQueen et al. (1967).

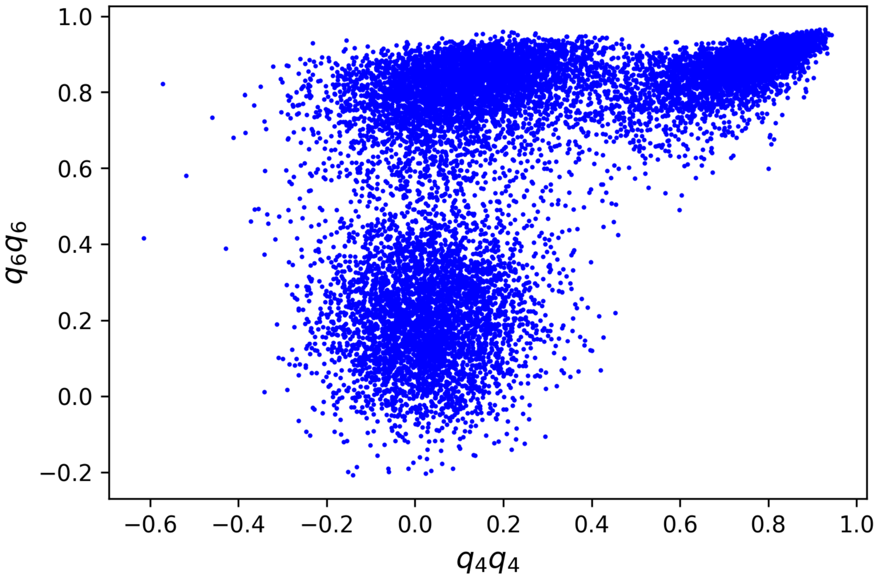

Figure 5.8: shows $q_4q_4 - q_6q_6$ plain of a set of hard-core Yukawa particles consist of BCC, FCC and fluid particles which are presented via blue points. At this point, machine does not have any idea about the structures and just have a set of unlabeled data. The bulk systems in this figure are correspond to the densities of figure 5.1

The K in K-Means refers to the number of clusters we want to segment our data into. The idea behind K-means clustering is that one should decide on how many clusters one wants to create with the given data. So the key part with K-Means is that we have to specify what K is. In our case we know in advance that we are dealing with hard-core Yukawa systems which consist of BCC, FCC and fluid phases so we will set K to three since we want K-Means to segment our data into three clusters.

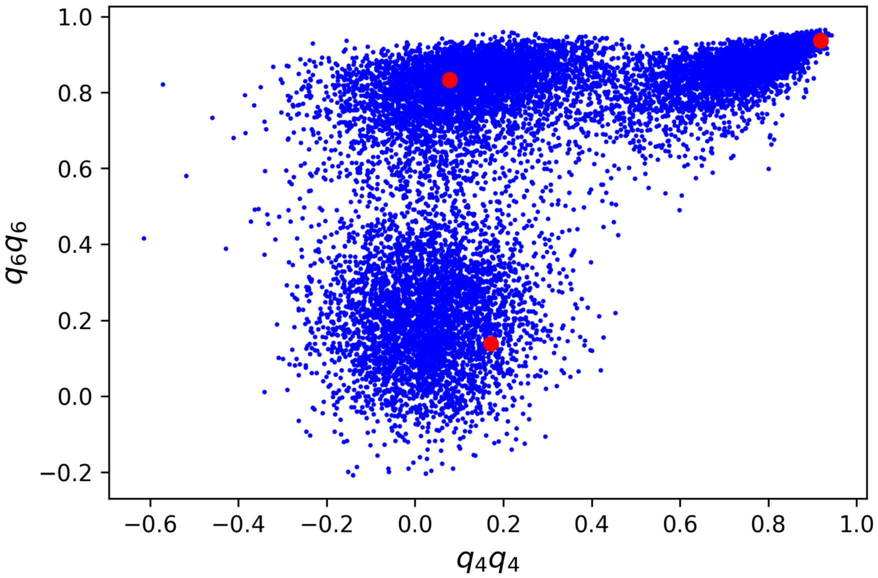

Figure 5.9: shows the randomly chosen K points (three particles in our case) as the initial centroids that create the initial K clusters. The bulk systems in this figure are correspond to the densities of figure 5.1

The starting point of the method is that we need to select k particles (three particles in our case) at random and assign their coordinates as the initial centroids of the just created clusters (fig. 5.9). Before we can assign particles to the clusters, we need a way to compare the q_4q_4 and q_6q_6 values of the particles with each cluster's centroids. Euclidean distance is the most common technique used in data science for measuring the distance between vectors and works extremely well in 2 and 3 dimensions. Then for each particle, calculate the Euclidean distance between that particle's coordinates, or values for q_4q_4 and q_6q_6, and each of the centroids' coordinates. Euclidean distance is defined as

$$d = \left((q_1 - p_1)^2 + (q_2 - p_2)^2 + \cdots + (q_n - p_n)^2\right)^{1/2} \quad . \tag{5.11}$$

Now we can assign the particle to the cluster whose centroid is the closest to, or has the lowest Euclidean distance to the particle's values. Then for each cluster, we compute the new centroid by calculating the arithmetic mean of all of the particles in that cluster. We calculate the arithmetic mean by taking the average of all of the X values (q_4q_4) and the average of all of the Y values (q_6q_6) of the particles in that cluster. Figure 5.10 shows the initial estimation of the clusters based on the given unlabeled data. But this initial result can be far from the reality and desired outcome so these steps should be repeated until the clusters are no longer moving and have converged (fig 5.11).

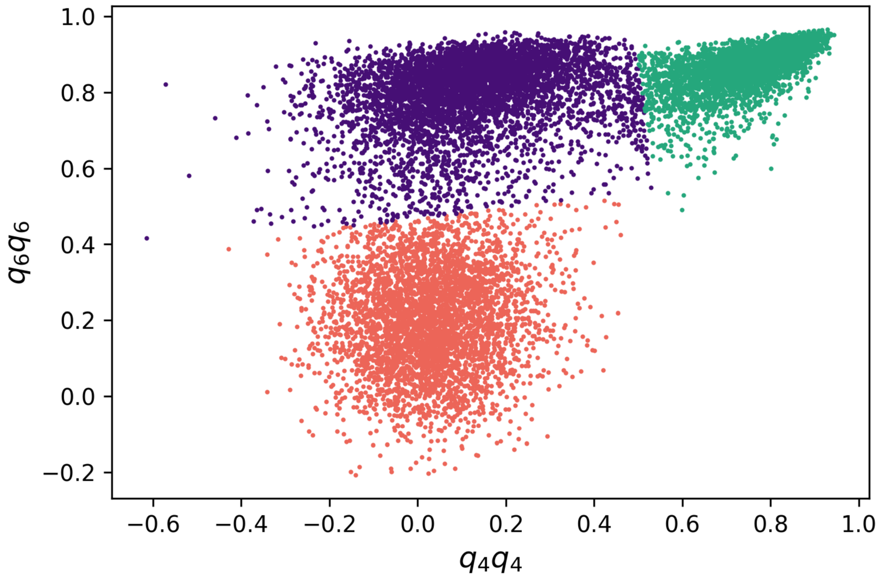

Figure 5.10: shows the initial estimation of structures based on the initial randomly chosen centroids. This initial estimation can be far from the desired results and one should repeat the steps of algorithm to to the point that the clusters are converged. The bulk systems in this figure are correspond to the densities of figure 5.1

One can also assign the order to the particle via combining the average local bond order parameters $\bar{q}_4$ and $\bar{q}_6$ to the K-Means clustering technique. In fact this technique in combination with local bond order parameters can give us an

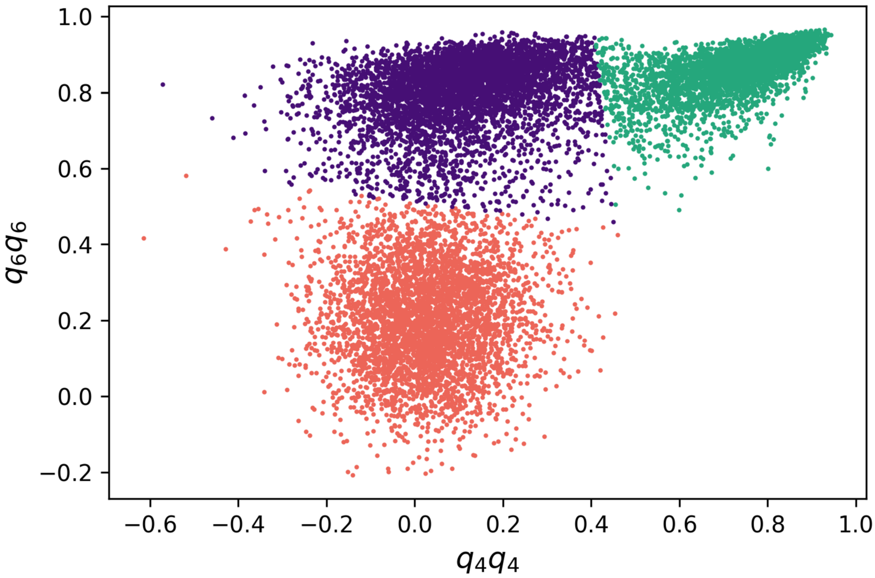

Figure 5.11: shows the final estimation of the clusters inside the given configuration. This result can be different if one consider different feature beside the q_4q_4 and q_6q_6. The alternative feature for this calculation can be average local order parameters $\bar{q}_4$ and also $\bar{q}_6$. Moreover one can combine these features together to get a more accurate result. The bulk systems in this figure are correspond to the densities of figure 5.1

optimum threshold for distinguishing different phases and assigning a more accurate order to the particles of a system.

6 Results

In this chapter, we present the results that we have obtained from the study of the charged colloids in confinement. As mentioned in chapter 2, we have modeled the charged colloids via a hard-core Yukawa potential. Here, we present the simulation results for the different hard-core Yukawa phases (BCC, FCC, fluid) in confinement. First, we explore the effect of hard flat walls on the charged colloids, followed by the investigation of the behavior of the charged colloids between charged walls. All the simulation in this work have been done via a modifed LAMMPS (Plimpton (1995)) that is tailored for this specific problem. Moreover all the snapshots that are presented in this chapter are made by OVITO software Stukowski (2009).

6.1 Hard Walls Confinement

As we already discussed in previous chapters, Davidchack and Laird (2003) and Fortini and Dijkstra (2006) have observed the pre-freezing of hexagonal layers in confined hard-sphere fluids induced by the hard walls even slightly lower than the coexistence densities. In this part, we try to understand the behavior of the hard-core Yukawa systems which are confined between two parallel flat walls. We address the question about the possibility of a pre-freezing transition and we compute the excess energy to form an interface between crystal and walls as well as fluid and walls. The molecular dynamics (MD) simulation at constant temperature (NVT) has been done to study the phase behavior of FCC, BCC and corresponding fluids at confinement. We are dividing this section into two part. In the first part, we are discussing the behavior of the FCC crystal and corresponding fluid at flat hard wall confinement, and in the second part, we will discuss the result for the confined BCC crystals, and the corresponding fluids.

6.1.1 FCC-Fluid coexistence

Now, we consider states at $\kappa\sigma = 5.1738$ around FCC-fluid coexistence in the bulk phase diagram of the hard-core Yukawa system. Figure 6.1 represents the different systems of particles of FCC and fluid phases that we have considered. The calculation of the coexistence density has been done via the mapping scheme of equations (2.24) and (2.25), as proposed by Hynninen and Dijkstra (2003). These coexistence points correspond to packing fractions $\eta^{fl}_{coex} = 0.1366$ and $\eta^{FCC}_{coex} = 0.1397$ and they are presented in figure 6.1. Moreover, to get a clear idea about the behavior of these systems at coexistence, we approach them from lower and higher packing fractions η.

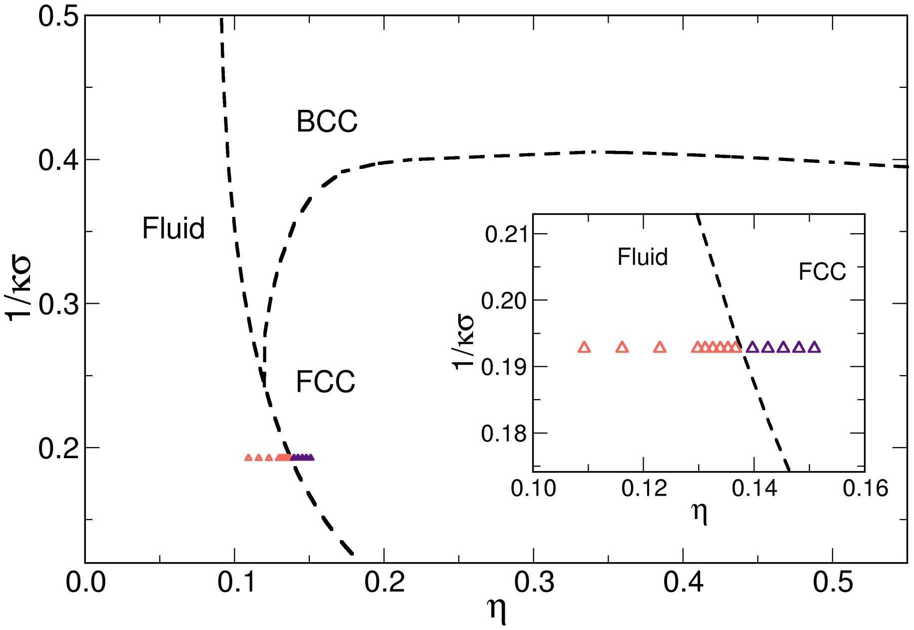

Figure 6.1: shows the phase diagram of hard-core Yukawa particles at $\beta\varepsilon = 81$, as introduced by Hynninen and Dijkstra (2003). This phase diagram consists of FCC, BCC and fluid phases. In the subset of the figure, one can see the systems that we have considered alongside the FCC-fluid boundary line for a constant value of $\kappa\sigma = 5.1738$ for a wide range of packing fraction η.

Moreover, to verify the accuracy of this calculation, we have performed Molecular Dynamics (MD) simulations in the canonical (NVT) ensemble for the bulk hard-Yukawa FCC phase and the corresponding coexistence fluid. The calculated values for the total pressure indicate that these two phases have the same pressure and exhibits that the calculated coexistence point due to the equality of bulk pressure is the accurate coexistence points. Figure 6.2 shows the calculated total pressure for the bulk FCC and fluid phases. The inset illustrates that the bulk pressure of the chosen state points are equal.

After confirming the value of the packing fraction η for coexisting densities, now we can investigate the behavior of these systems in the presence of hard walls. To this end, we are approaching the coexisting densities from both sides

Phases	η	N	$L_x \times L_y \times L_z$
Fluid	0.1366	56784	$45.6741 \times 42.5976 \times 112.6382$
	0.1352		$45.8273 \times 42.7405 \times 113.0136$
	0.1339		$45.9827 \times 42.8854 \times 113.3941$
	0.1325		$46.1402 \times 43.0323 \times 113.7799$
	0.1311		$46.2998 \times 43.1812 \times 114.1709$
	0.1298		$46.4617 \times 43.3322 \times 114.5675$
	0.1229		$47.3067 \times 44.1202 \times 116.6372$
	0.1161		$48.2166 \times 44.9689 \times 118.8661$
	0.1093		$49.2009 \times 45.8869 \times 121.2771$
FCC	0.1397	56784	$45.3364 \times 42.2827 \times 111.8290$
	0.1425		$45.0381 \times 42.0045 \times 111.1064$
	0.1453		$44.7475 \times 41.7335 \times 110.4026$
	0.1480		$44.4643 \times 41.4693 \times 109.7189$
	0.1508		$44.1881 \times 41.2117 \times 109.0504$

Table 6.1: Shows the packing fractions, size, and geometries of different simulated hard-core Yukawa fluid and FCC systems which are in confinement by a pair of parallel walls. The systems correspond to the triangles of figure 6.1.

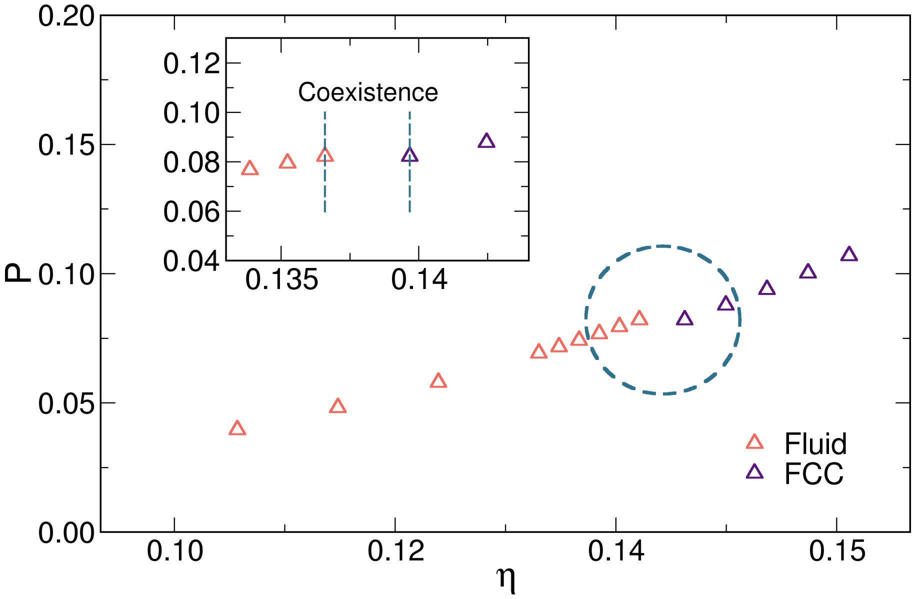

Figure 6.2: Shows the pressure of the bulk FCC crystals and corresponding fluids as a function of packing fraction η at a constant value of $\kappa\sigma = 5.1738$. As one can expect the figure indicates that by the increment of packing fraction, the values of pressure p are increasing. The subset also verfies that the considered coexistence densities have the same pressure as we expect.

(see figure 6.1). To study the behavior of these systems in the presence of a pair of parallel flat hard walls, we put the walls at the z-boundaries of the simulation boxes and switch off the periodic boundary conditions in this direction.

Table 6.1 gives the packing fraction, particle number and box dimensions of the considered systems in the fluid and FCC state. The considered FCC crystal in this study has the (111) orientation along the z-plane and the fluids obtained from the melting of the corresponding crystals.

Now, we have confined the FCC crystal at the coexistence density as well as four higher densities (up to 20% higher than coexistence from table 6.1) between a pair of parallel flat hard walls. By performing MD simulation at constant temperature for 2×10^6 MD steps, we were able to calculate a number density profile in z-direction $\rho(z)$ which is averaged over 1000 different configurations for each density. To keep the temperature constant, we have applied the Berendsen thermostat with damping frequency of $500\mathrm{dt}$, in which $\mathrm{dt} = 0.001\tau$ is the time step of the simulation ($\tau = \sqrt{m\sigma^2/\varepsilon}$).

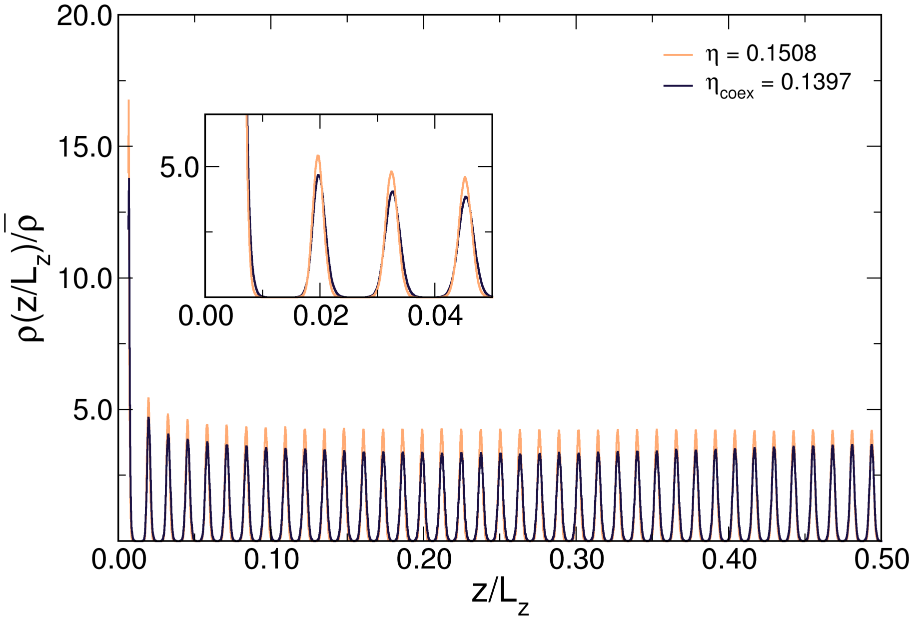

Figure 6.3: shows the density profiles for the coexisting FCC crystal $\eta^{FCC}_{coex} = 0.1397$ and considered nost dense system $\eta = 0.1508$. The density profiles indicate the changes in lattice constant but the density in between remains equal to the density of the bulk.

Figure 6.3 represents the FCC crystal at coexistence with packing fraction $\eta^{FCC}_{coex} = 0.1397$ and the most dense considered FCC with packing fraction $\eta = 0.1508$. These density profiles show forming of high density layers next to the hard walls, but in fact, FCC crystals in hard walls confinement are stable FCC crystals. This dense layer is due to the change of the lattice constant in FCC crystals in very first layers, but in the middle of the system, the density is equal to the density of the bulk crystal. However, we did not show the systems between $\eta^{FCC}_{coex} = 0.1397$ and $\eta = 0.1508$, but our study shows that the behavior at those densities for the FCC crystal is entirely the same.

When we are confining some systems between the walls, the critical question is whether the order of the system will change or not? In other words will the system experience a transition or not? To answer this question, we have employed the local bond order parameter schemes which are proposed by Ten Wolde, Ruiz-Montero, and Frenkel (1995) and Lechner and Dellago (2008) (see chapter 5).

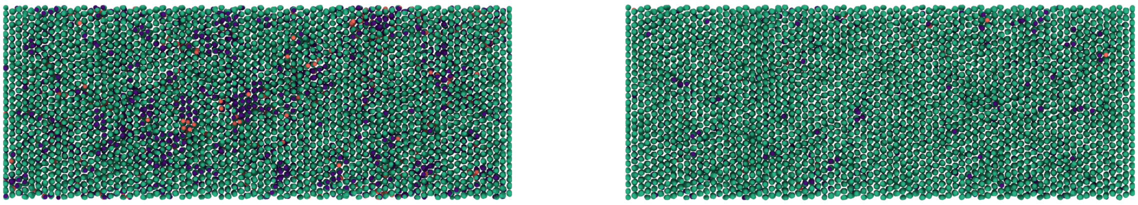

(a) $\eta^{FCC}_{coex} = 0.1397$, Ten Wolde, Ruiz-Montero, and Frenkel (1995) approach

(b) $\eta = 0.1508$, Ten Wolde, Ruiz-Montero, and Frenkel (1995) approach

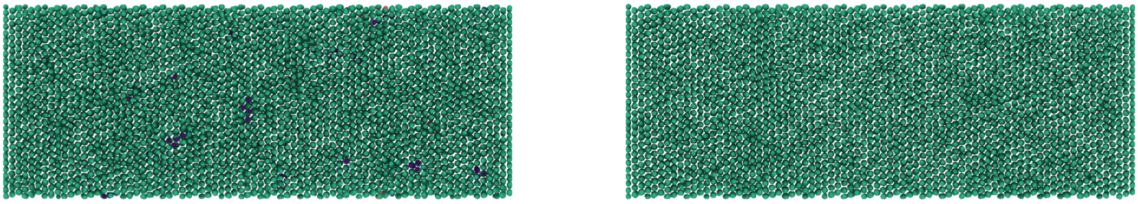

(c) $\eta^{FCC}_{coex} = 0.1397$, Lechner and Dellago (2008) approach

(d) $\eta = 0.1508$, Lechner and Dellago (2008) approach

Figure 6.4: Shows the structure analysis of the confined FCC crystals with $\eta^{FCC}_{coex} = 0.1397$ and $\eta = 0.1508$ between parallel flat hard walls. These results verify that there is no transition in confined FCC crystals. Moreover, the figures indicate that the structure analysis via calculation of $\bar{q}_4$ and $\bar{q}_6$ has the minor advantage than the one with q_4q_4 and q_6q_6 calculation.

In figure 6.4, we compare the two densities $\eta^{FCC}_{coex} = 0.1397$ and $\eta = 0.1508$ by considering the $q_4q_4 - q_6q_6$ as well as the $\bar{q}_4 - \bar{q}_6$ plane. It turns out as we can also conclude from the density profiles in figure 6.3 that the FCC crystal do not experience any change in structure beside the minor change in the lattice constants. Regarding the local bond order parameter, one can also conclude that both approaches are good enough in the case of the FCC crystals.

To be more precise, one can also take a closer look at the first layer of the FCC crystals in the vicinity of the hard walls. Figure 6.5 shows the structure of first layer for both $\eta^{FCC}_{coex} = 0.1397$ and $\eta = 0.1508$ which are calculated for both structure analysis approaches (Ten Wolde, Ruiz-Montero, and Frenkel (1995) and Lechner and Dellago (2008)). However the difference between the upper part of the figure which is calculated via q_4q_4 and q_6q_6 and the bottom part that is calculated by $\bar{q}_4$ and $\bar{q}_6$ is minor, but one can say that the q_4q_4 and q_6q_6 has some minor calculation error which can lead to non-accurate identification of orders in some part of the system. This means that the Lechner and Dellago (2008) approach so far has a bit higher accuracy to the one proposed by Ten Wolde, Ruiz-Montero, and Frenkel (1995).

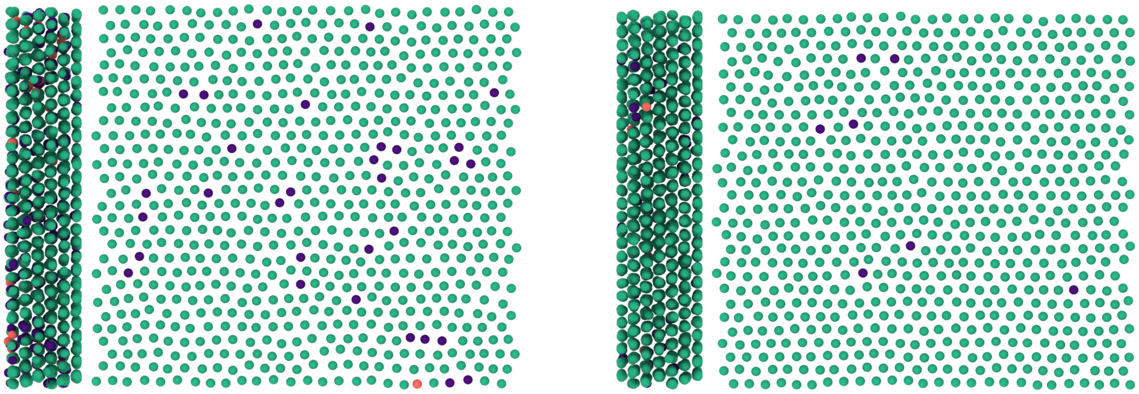

(a) $\eta = 0.1397$, Ten Wolde, Ruiz-Montero, and Frenkel (1995) approach

(b) $\eta = 0.1508$, Ten Wolde, Ruiz-Montero, and Frenkel (1995) approach

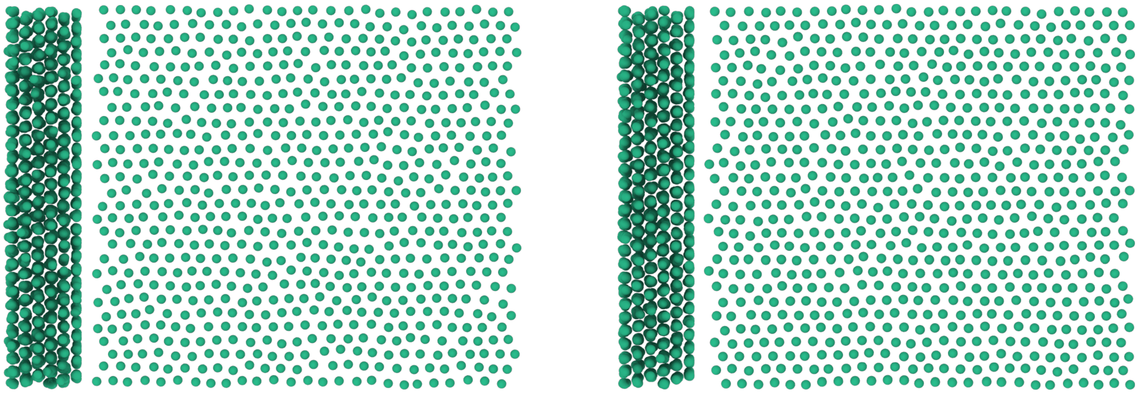

(c) $\eta = 0.1397$, Lechner and Dellago (2008) approach

(d) $\eta = 0.1508$, Lechner and Dellago (2008) approach

Figure 6.5: shows a slice of FCC crystal with a width of $\sim 10\sigma$ as well as the first layer of the crystal close to the hard walls. The upper part (a and b)of the plot exhibits the system at coexistence, and a higher density which is analyzed via $q_4q_4 - q_6q_6$ plane and the bottom part (c and d) are the ones which their structures are studied by $\bar{q}_4 - \bar{q}_6$ plane. This comparison shows that the Lechner and Dellago (2008) approach is more efficient in the case of confined FCC crystals.

So far we understand that the FCC crystals with (111) orientation along the z-direction are stable in the presence of parallel flat hard walls and they do not experience any transitions. Now, we can approach the other coexisting point at $\eta^{fl}_{coex} = 0.1366$. To this end, we are studying the system with densities from 20% lower than the coexistence $\eta = 0.1093$ to the coexistence density $\eta^{fl}_{coex} = 0.1366$ (see table 6.1). Same as the FCC crystal case, we inserted two parallel flat hard walls at the boundaries of these fluids in z-direction and we performed MD simulations at constant temperature for 2×10^6 times steps.We calculated a number density profile in z-direction $\rho(z)$ which is averaged over 1000 different configurations for each density. To keep the temperature constant, we also applied the Berendsen thermostat with damping frequency of $500\mathrm{dt}$.

Figure 6.6 shows the density profile for the three different packing fractions $\eta^{fl}_{coex} = 0.1366$, $\eta = 0.1298$ and $\eta = 0.1093$ which correspond to the fluid at coexistence, and 5%, and 20% below the coexistence density, respectively. It is evident that some layers are formed close to the hard walls. These layers are

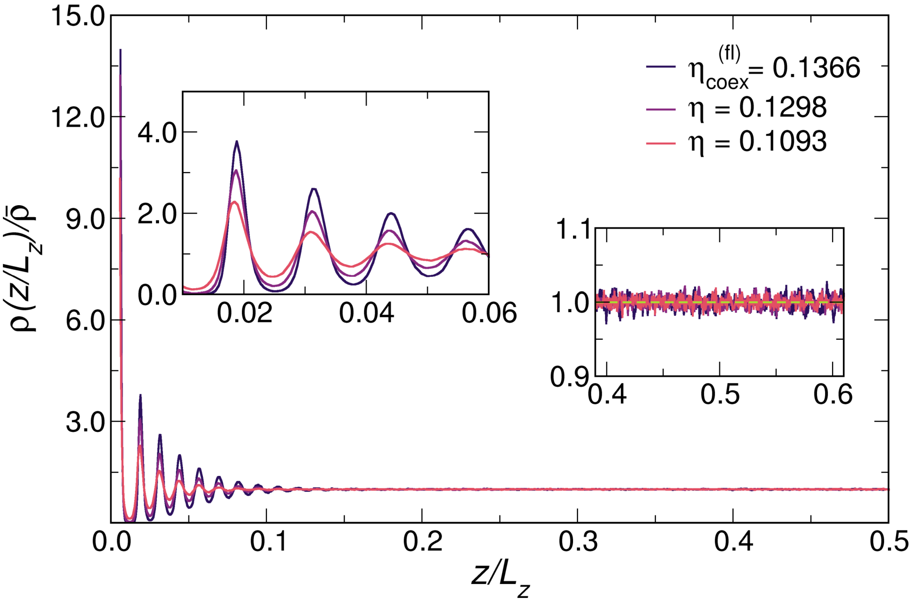

Figure 6.6: shows the density profile of fluids confined by the flat hard walls which consists of systems with packing fraction $\eta_{coex}^{fl} = 0.1366$, $\eta = 0.1298$ and $\eta = 0.1093$. All these three systems show the formation of layers close to the hard walls.

denser in the vicinity of the wall, and from the inset we can observe that the density of these layers is much higher than the bulk density and especially the first layer has the density around 13 times larger than the bulk density. Moreover, the right side inset indicates that the positions of the walls are well defined such that the density in the middle of the system is equal to the bulk density and this is the behavior that we expect.

By observing these high density layers in the vicinity of the wall, the question is arising about the specific structures within these layers. Or in other words do these layers indicate any transition from a fluid to an ordered structure? We try to answer these questions by calculation of local bond order parameters which we have introduced in chapter 5. This analysis can help us to understand the exact structure and order of the layers in the vicinity of the wall.

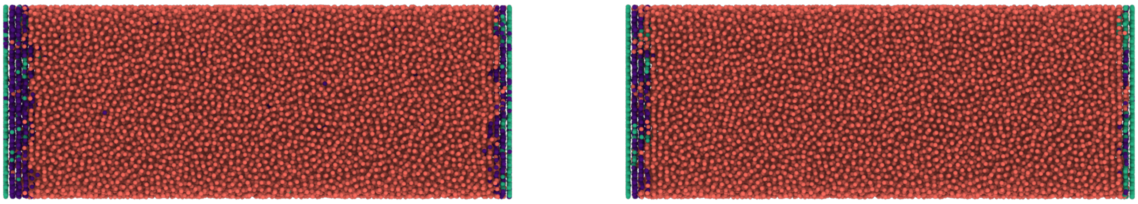

(a) $\eta = 0.1366$, Ten Wolde, Ruiz-Montero, and Frenkel (1995) approach

(b) $\eta = 0.1366$, Lechner and Dellago (2008) approach

Figure 6.7: shows the snapshots of the confined fluid at coexistence with packing fraction $\eta_{coex}^{fl} = 0.1366$. These snapshots which are resulted from structure analysis via local order parameters confirmed that the formed layers close to the flat hard walls have a specific FCC or BCC orders and it is the evidence of pre-freezing phenomena.

In figure 6.7 we show snapshots of the coexisting fluid with $\eta_{coex}^{fl} = 0.1366$ in flat hard wall confinement. We have analyzed the structure of this system using two different definitions of local bond order parameters. Figure 6.7a shows the snapshot of a fluid at coexistence density in confinement. Here the color map is based on the $q_4q_4 - q_6q_6$ plane analysis (figure 5.2), and it suggests that at least the first four layers close to the hard walls consist of particles with specific orders (FCC and BCC). As we have discussed in the case of the confined FCC crystal, it turns out that the structure analysis via the $\bar{q}_4 - \bar{q}_6$ plane is more efficient than the other approach. By this analysis, (figure 6.7b) we see that the first layer close to the wall has the FCC structure but it is not clear if the other layers are BCCs or just some amorphous layers which are a mixture of different type of particles.

These structured layers indicate that a pre-freezing has happened at coexistence which is previously observed in the case of a confined hard sphere fluid at coexistence by Davidchack and Laird (2003) and Fortini and Dijkstra (2006). In their case, the pre-freezing was not observed at densities lower than coexistence, and it can be an excellent exercise to examine the structure of lower density in confined hard-core Yukawa fluids.

To this end, we have studied the structure of the first layer for the system with packing fractions of $\eta^{\mathrm{fl}}_{\mathrm{coex}} = 0.1366$, $\eta = 0.1298$ and $\eta = 0.1093$ for which the corresponding density profiles are shown in figure 6.6.

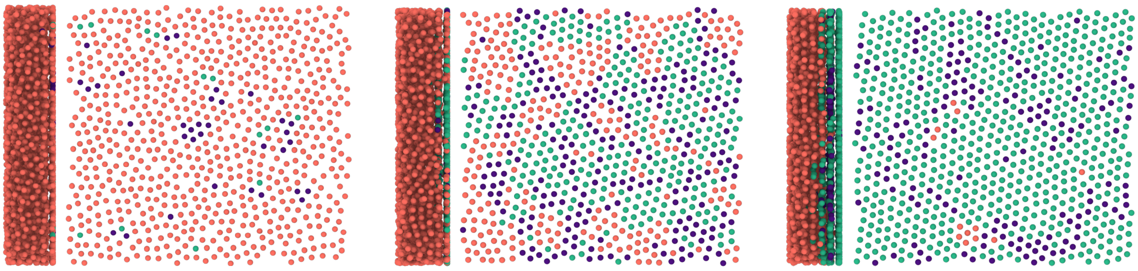

(a) $\eta = 0.1093$, Ten Wolde, Ruiz-Montero, and Frenkel (1995) approach

(b) $\eta = 0.1298$, Ten Wolde, Ruiz-Montero, and Frenkel (1995) approach

(c) $\eta = 0.1366$, Ten Wolde, Ruiz-Montero, and Frenkel (1995) approach

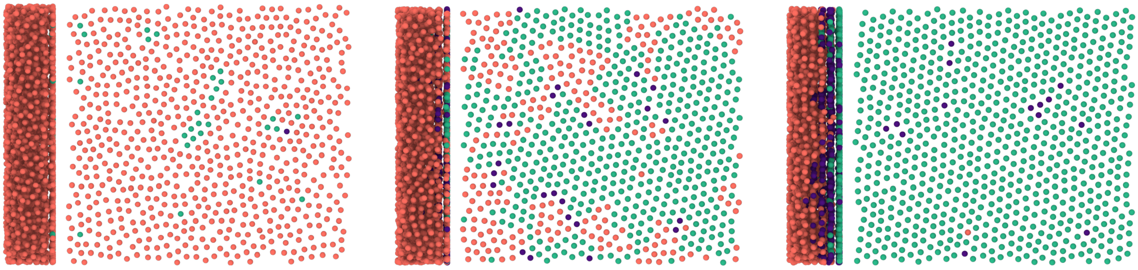

(d) $\eta = 0.1093$, Lechner and Dellago (2008) approach

(e) $\eta = 0.1298$, Lechner and Dellago (2008) approach

(f) $\eta = 0.1366$, Lechner and Dellago (2008) approach

Figure 6.8: shows the structure analysis of first layer of fluids in hard walls confinement for the system with packing fraction of $\eta^{\mathrm{fl}}_{\mathrm{coex}} = 0.1366$, $\eta = 0.1298$ and $\eta = 0.1093$. The top sub-figures are analyzed via $q_4q_4 - q_6q_6$ plane and the bottom sub-figure are studied by $\bar{q}_4 - \bar{q}_6$ calculations. In lowest density system $\eta = 0.1093$ the first layer is a amorphous layer, while at $\eta = 0.1298$ the first layer shows the transition from fluid to a hexagonal layers which is more pronounced at coexistence density $\eta^{\mathrm{fl}}_{\mathrm{coex}} = 0.1366$.

Figure 6.8 provides the 2D snapshots of the first layer of the fluid with packing fractions $\eta^{fl}_{coex} = 0.1366$, $\eta = 0.1298$ and $\eta = 0.1093$ as well as a 10σ slice of the system in z-direction. It turns out that in a system with a packing fraction of $\eta = 0.1093$ which is 20% lower than the coexistence density the first layer near the hard walls is an amorphous layer. This result confirms that at sufficiently low density system there is no evidence of pre-freezing. Also, for this density, there is an agreement between the $q_4q_4 - q_6q_6$ and the $\bar{q}_4 - \bar{q}_6$ plane structure analysis.

However with both approaches, from the calculation of the local bond order parameters, it turns out that at the packing fraction $\eta = 0.1298$ which is about 5% lower than the coexistence density, we can observe the formation of a hexagonal layer near the hard wall, i.e., there is pre-freezing. The exciting part of this result is that the pre-freezing happens at densities well below the coexistence density which has not been observed in the hard sphere fluid case, studied by Davidchack and Laird (2003) and Fortini and Dijkstra (2006). The structural analysis via $\bar{q}_4 - \bar{q}_6$ shows even a more pronounced hexagonal layer near the hard wall (see figure 6.8e). Figures 6.8c and 6.8f indicate that the first layer near the wall at coexistence with packing fraction $\eta^{fl}_{coex} = 0.1366$ has a hexagonal structure.

So far we have observed pre-freezing of hexagonal layers at the vicinity of the flat hard walls even at densities lower than coexistence which correspond to the dense layers that we can also observe in density profiles of figure 6.6. Now we can calculate the 2D packing fraction of the first layer η_{2D1st} of the fluids and compare them with the one for FCC crystals.

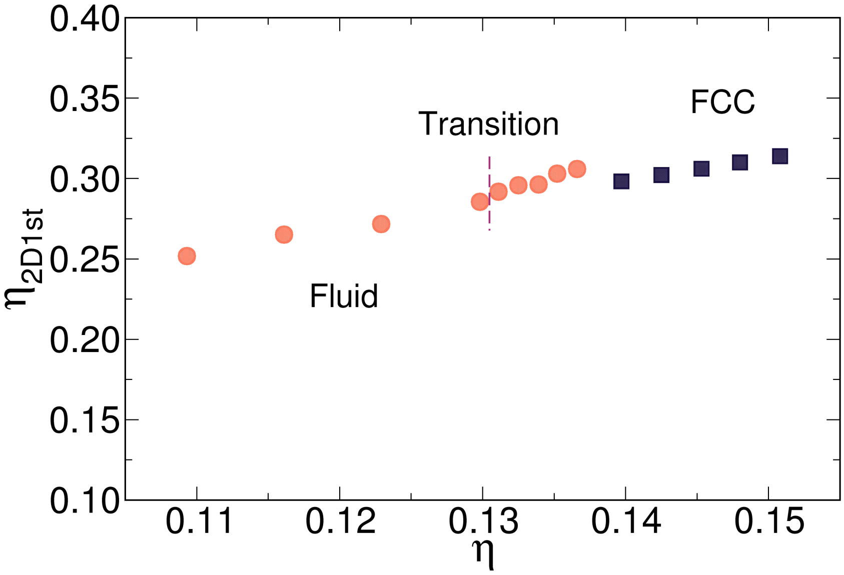

Figure 6.9: shows the 2D packing fraction of the first layer η_{2D1st} for both FCC and fluids as a function of bulk packing η. The packing fraction of the first formed layer from fluid near the wall at coexistence is higher than the one for FCC crystal because for the FCC. This layer is just one of its layers which has the bulk density, but for the fluid, it is a highly dense hexagonal layer which is now formed in the vicinity of hard walls.

Figure 6.9 shows the calculated values of 2D packing fraction of the first layer η_{2D1st} for both FCC and corresponding fluids. The values of η_{2D1st} are increasing by the increment of bulk packing fraction in both phases. However, one can observe that in the fluid systems with the evidence of pre-freezing the calculated values are even bigger than the FCC crystals.

Moreover, we can study the evolution of local bond order parameters such as q_6q_6 for the layer near the wall with respect to the pecking fraction η that enables us to identify the densities at which the phase transition occurs. Figure 6.10 shows the average of local bond order parameter q_6q_6 for FCC crystals and fluids and indicates the phase transition from a fluid to the hexagonal layers.

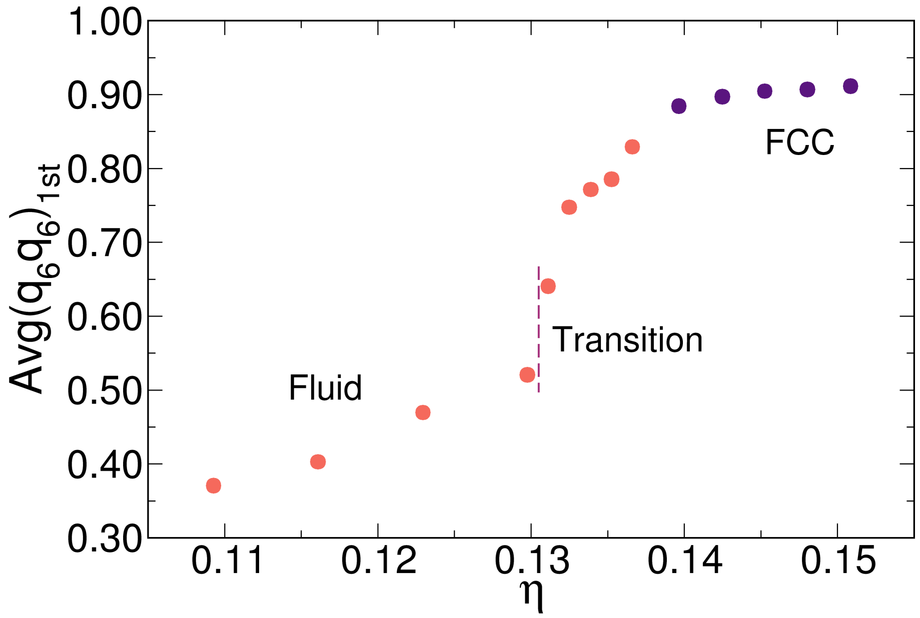

Figure 6.10: shows the average of q_6q_6 for the first layer in the vicinity of the wall for FCC crystals and corresponding fluids. The result is in agreement with transition line in figure 6.9.

As we have already mentioned, the interfacial free energy between crystal or liquid concerning the flat walls is a critical value that can help us to have a more clear idea about nucleation or wetting phenomena in confinement. Here, we calculated the fluid-wall γ_{fw} and crystal-wall γ_{cw} interfacial free energies for the corresponding systems in flat hard wall confinement. In chapter 4 we have introduced a modified thermodynamic integration method as our approach to calculating interfacial free energies.

As the first step, we consider a λ-dependent Hamiltonian of our system that has the following form

$$\mathcal{H}(\lambda) = \sum_{i=1}^{N} \frac{\vec{p}_i^{\,2}}{2m} + U_{p-p} + U_{p-im}(\lambda) + U_{p-fw}(\lambda) \quad . \tag{6.1}$$

The interaction between particles and image particles, $U_{p-im}(\lambda)$, can be described as

$$\begin{aligned} \mathrm{U}_{p-im}(\lambda) &= \sum_{i,im} u_{i,im}(\lambda, r_{i,im}) \\ u_{p-im}(\lambda, r) &= (1-\lambda)^2\, \varepsilon \left(\frac{\exp\left[-\kappa\sigma\left(r/\sigma - 1\right)\right]}{r/\sigma} + \left(\frac{\sigma}{r}\right)^{256} \right) \end{aligned} \tag{6.2}$$

and the interaction between particles and the flat wall can be described as

$$\begin{aligned} \mathrm{U}_{p-fw}\left(\lambda\right) &= \sum_{i} u_{p-fw}\left(\lambda, z_i\right) \\ u_{p-fw}\left(\lambda, z\right) &= \lambda^4\left(1-\lambda\right)^4 \varepsilon \left[\left(\frac{\sigma}{z}\right)^{12} + \left(\frac{\sigma}{L_z - z}\right)^{12} \right] \\ &\quad + \lambda^{128}\left(\frac{1+\lambda}{2}\right)^{196} \varepsilon \left[\left(\frac{\sigma}{z}\right)^{256} + \left(\frac{\sigma}{L_z - z}\right)^{256} \right] \end{aligned} \tag{6.3}$$

It is important to mention that the exponents in equations (6.2) and (6.3) is chosen such that the resulting integrands are smooth and reversible as it is explained in chapter 4.

To calculate the interfacial free energy of crystal and fluid regarding the flat hard wall one needs to calculate the partial derivative of the interaction terms. If we consider the term U_{p-im}, i.e., the total interaction of particles with image particles then the derivatives of each particle's contribution in this interaction can be written as

$$\frac{\partial \mathcal{H}}{\partial \lambda} = \frac{\partial \mathrm{U}_{p-im}\left(\lambda\right)}{\partial \lambda} + \frac{\partial \mathrm{U}_{p-w}\left(\lambda\right)}{\partial \lambda} \tag{6.4}$$

in which

$$\frac{\partial u_{p-im}(\lambda, r)}{\partial \lambda} = -2\left(1-\lambda\right) \left(\frac{\exp\left[-\kappa\sigma\left(r/\sigma - 1\right)\right]}{r/\sigma} + \left(\frac{\sigma}{r}\right)^{256} \right) \tag{6.5}$$

And finally, the partial derivative of the Hamiltonian can be written as

$$\begin{aligned} \frac{\partial u_{p-w}\left(\lambda, z\right)}{\partial \lambda} &= \left[4\lambda^3\left(1-\lambda\right)^3\left(2\lambda - 1\right)\right] \varepsilon \left[\left(\frac{\sigma}{z}\right)^{12} + \left(\frac{\sigma}{L_z - z}\right)^{12} \right] \\ &\quad + \left[128\lambda^{127}\left(\frac{1+\lambda}{2}\right)^{196} + \lambda^{128}\frac{196}{2^{196}}\left(1+\lambda\right)^{195} \right] \\ &\quad .\ \varepsilon \left[\left(\frac{\sigma}{z}\right)^{256} + \left(\frac{\sigma}{L_z - z}\right)^{256} \right] \end{aligned} \tag{6.6}$$

To calculate the fluid-wall γ_{fw} and the crystal-wall γ_{cw} interfacial free energies, we have considered the system of particles which are described in table 6.1. To have a smooth and reversible thermodynamic path from $\lambda = 0$ which corresponds to the bulk system to $\lambda = 1$ which indicates the completely confined system of particles, we have performed 51 independent simulations. Moreover, to get a smooth and reversible path the position of the wall is a function of λ

$$z\prime(w) = z_w + [(1-\lambda) z_w \alpha_w] \qquad \text{for } \lambda > 0 \tag{6.7}$$

where the $z_w = 0.4\sigma$ is the position of the hard walls at $\lambda = 1$ and $\alpha_w = 0.4$ controls where the wall is placed during the thermodynamics integration path.

To calculate the energies according to equations (6.5) and (6.6), we have run our MD simulation for $10^6 - 2 \times 10^6$ steps with time step $dt = 0.001\tau$ where $\tau = \sqrt{m\sigma^2/\epsilon}$ and $m = 1.0$. The simulations have been done at temperature $k_B T = 1/\beta\epsilon \approx 0.01234568$ using a Berendsen thermostat. With equations (6.5) and (6.6) we compute $\frac{\partial \mathcal{H}}{\partial \lambda}$ for each value of λ.

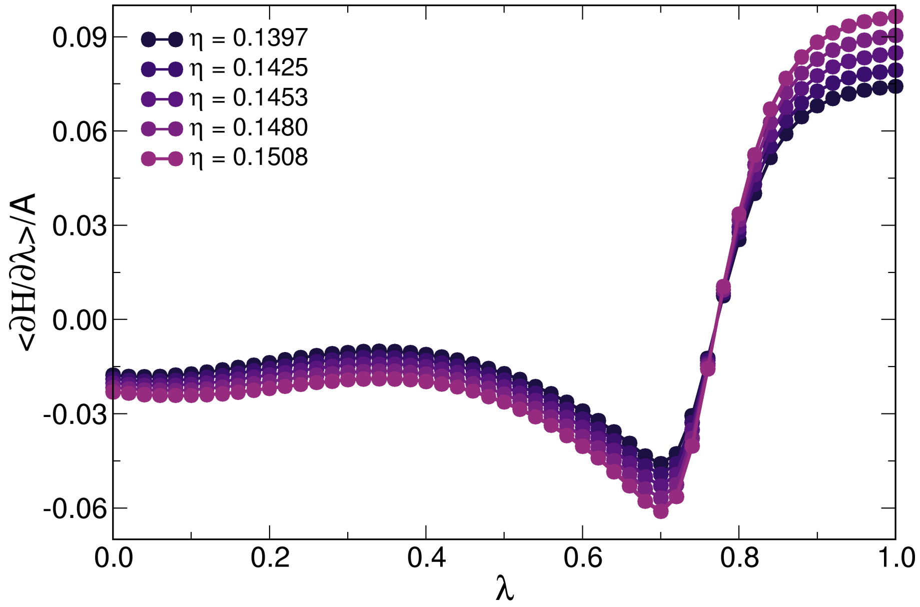

Figure 6.11: shows the corresponding smooth and reversible thermodynamic path for FCC crystal at coexistence and some density above that. Due to the strong particle-image contribution it shows negative value at $\lambda < 0.8$.

Figure 6.11 shows the resulting integrands of the confined FCC crystals for the systems between $\eta_{coex}^{FCC} = 0.1397$ and $\eta = 0.1508$. As one can see, the path between $\lambda = 0$ and $\lambda = 1$ is smooth for all the densities, and it is as we also expected from the behavior of the FCC crystal in confinement. The integrands for coexistence and higher densities are negative for $\lambda < 0.8$ which is due to the interaction with the image particles, described by equation (6.5).

The inset of this figure shows that in the path there is no jumps or any discontinuity, and the paths are smooth. However from $\eta = 0.1298$ to the coexistence $\eta_{coex}^{fl} = 0.1366$ by calculating the bond order parameters we are already aware of the phase transition of the fluids to hexagonal layers which means that the thermodynamic integration at these densities is not valid.

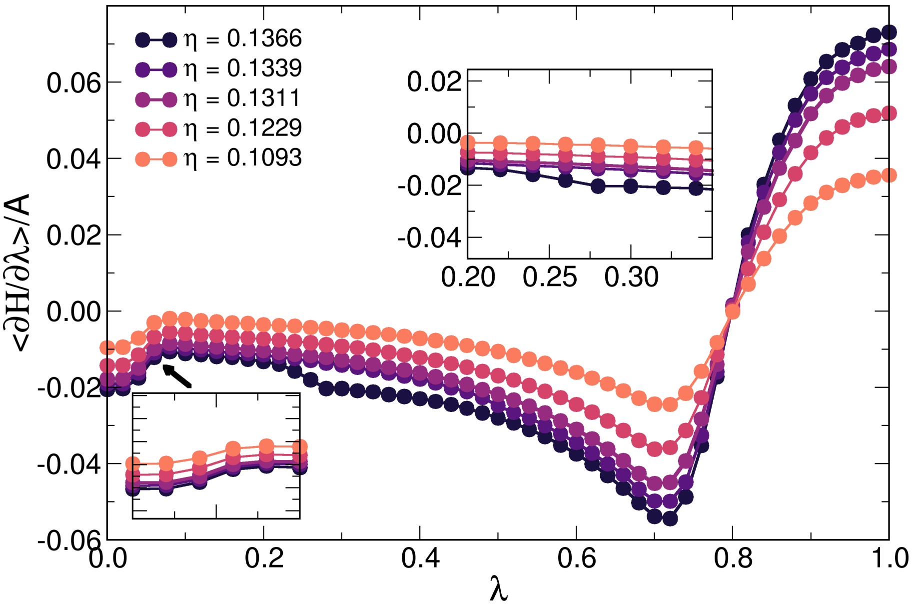

Figure 6.12: shows the calculated integrand for the fluid part of FCC-fluid path in the phase diagram. Insets make us sure that even at some shady points there is no evidence of discontinuity of any kink. Although, due to the transition of the fluid to hexagonal layers near the walls, the integrand for packing fraction higher than $\eta = 0.1289$ are not reliable.

From the calculated integrand of figures 6.11 and 6.12 we can calculate the free energy difference in these systems via

$$\Delta F = \int_0^1 \left\langle \frac{\partial \mathcal{H}}{\partial \lambda} \right\rangle_\lambda d\lambda \tag{6.8}$$

where $\langle \cdots \rangle_\lambda$ denotes the ensemble or time average over λ. And, finally, the

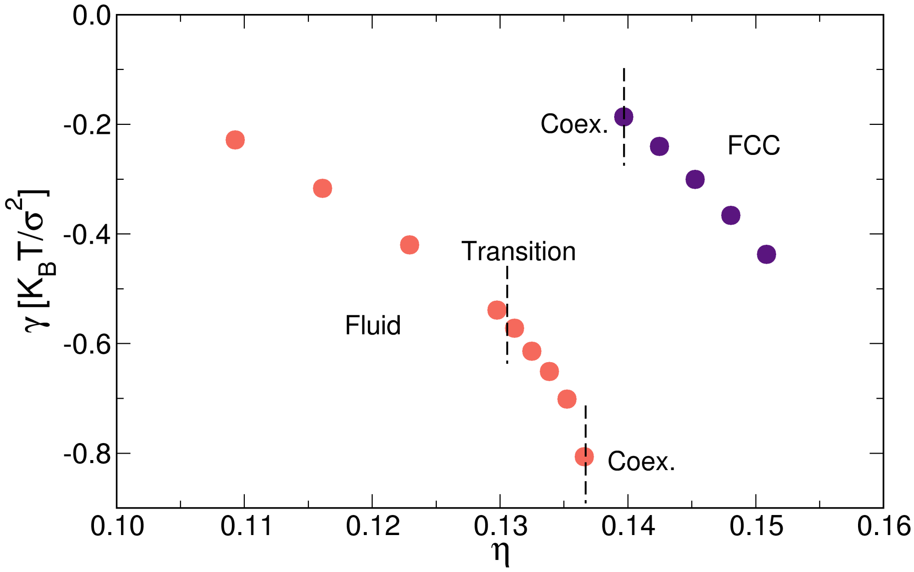

Figure 6.13: shows the calculated values for fluid-wall interfacial free energy γ_{fw} for the corresponding fluids of FCC-fluid path in the hard-core Yukawa phase diagram. It is important to know that due to the transition of the fluid to the hexagonal layers in the vicinity of the hard walls, the γ_{fw} value for packing fraction of $0.1298 \leqslant \eta \leqslant 0.1366$ are not reliable.

interfacial free energy of FCC and fluid with respect to the flat hard walls are calculated with

$$\gamma = \frac{\Delta F}{A} \tag{6.9}$$

with $A = 2L_xL_y$ as the total area of the interface.

Figure 6.13 represents the calculated values for the FCC-wall interfacial free energy γ_{cw} as well as fluid-wall interfacial free energy γ_{fw}. Since the contribution of equation (6.5) which corresponds to the interaction with the image particles is bigger than the particle-wall interactions, in total it makes the values of the interfacial free energies negative and this negativity raises by increasing of the packing fraction η in both FCC and fluid phases.

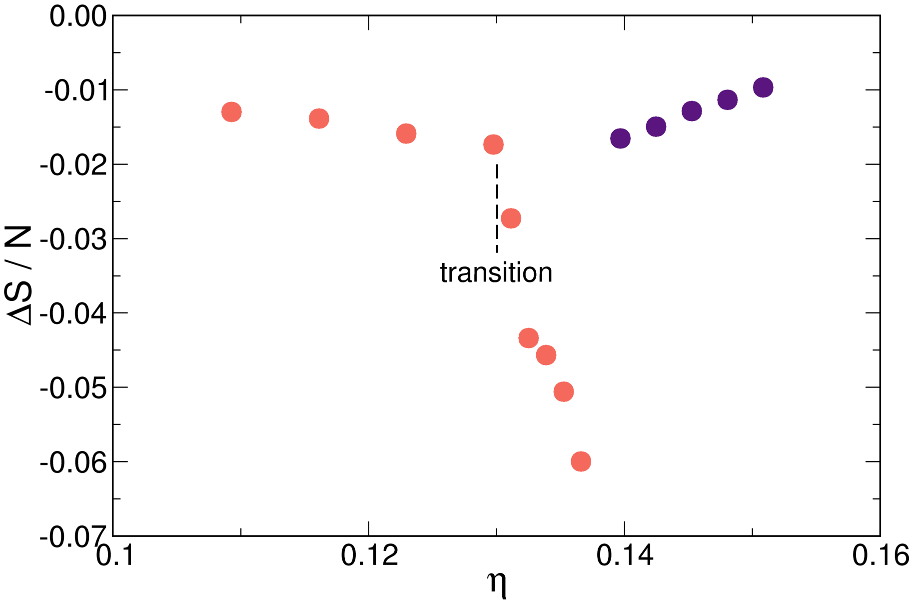

Figure 6.14: shows the difference of entropy between bulk system (FCC crystal and fluid) and confined system per particle. Same as the interfacial free energies γ_{fw} and γ_{cw}, $\Delta S/N$ are also negative but they are increasing by the increment of packing fraction η.

The difference of entropy between the bulk system (FCC crystal and fluid) and confined system per particle, $\Delta S = (\Delta E - \Delta F)/\Delta T$, can also help us to understand if our systems tend to be more ordered or disordered. Figure 6.14 shows ΔS as a function of packing fraction η. This figure indicates that the less ordered system has the bigger negativity of difference of entropy between the bulk system (FCC crystal and fluid) and confined system per particle, ΔS.

6.1.2 *BCC-Fluid coexistence Line*

As already mentioned, the phase diagram of the hard-core Yukawa systems (Hynninen and Dijkstra (2003)) consists of BCC, FCC, and fluid phases. We have studied the FCC crystal and corresponding fluids in the flat hard wall confinements. Now, as the next step of this study, we are considering another phase in the hard-core Yukawa phase diagram which is the BCC crystal. We have surveyed the behavior of the hard-core Yukawa system alongside the BCC-fluid coexistence in the flat hard wall confinement. Figure 6.15 shows the phase diagram of the hard-core Yukawa system and its inset specifies the different packing fractions that we have considered for a constant value of the $\kappa\sigma = 2.0616$.

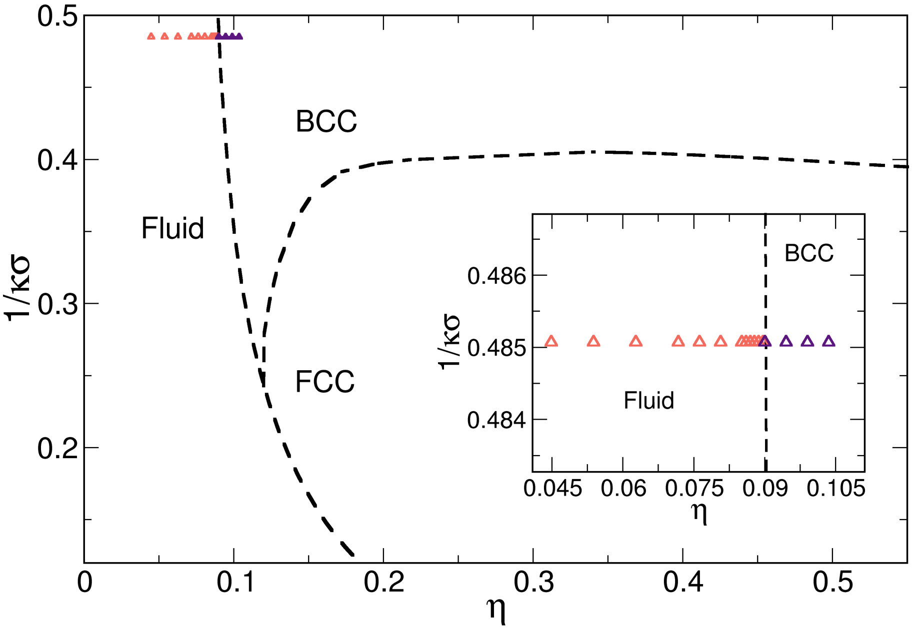

Figure 6.15: shows the phase diagram of the hard-core Yukawa system at contact value $\beta\varepsilon = 81$ which is proposed by Hynninen and Dijkstra (2003). The inset indicate the specific densities that we have considered in the BCC-fluid path at $\kappa\sigma = 2.0616$.

Phases	η	N	$L_x \times L_y \times L_z$
Fluid	0.0896	57344	$51.3499 \times 51.8820 \times 126.9811$
	0.0887		$51.5222 \times 52.0561 \times 127.4032$
	0.0878		$51.6969 \times 52.2326 \times 127.8310$
	0.0869		$51.8739 \times 52.4115 \times 128.2646$
	0.0860		$52.0534 \times 52.5928 \times 128.7043$
	0.0851		$52.2354 \times 52.7767 \times 129.1501$
	0.0806		$53.1854 \times 53.7365 \times 131.4770$
	0.0762		$54.2084 \times 54.7702 \times 133.9829$
	0.0717		$55.3150 \times 55.8882 \times 136.6935$
	0.0627		$57.8327 \times 58.4320 \times 142.8607$
	0.0538		$60.8820 \times 61.5130 \times 150.3299$
	0.0448		$64.6968 \times 65.3673 \times 159.6742$
BCC	0.0900	346800	$54.4759 \times 55.5029 \times 668.5363$
	0.0945		$53.5971 \times 54.6075 \times 657.7833$
	0.0990		$52.7724 \times 53.7673 \times 647.6927$
	0.1035		$51.9962 \times 52.9765 \times 638.1966$

Table 6.2: Size and geometries of the simulated fluid and BCC systems, confined between hard walls.

Table 6.2 shows the geometry of the BCC crystals and corresponding fluids that we have studied in confinement. In the following, we will describe the simulation that we performed and the results that we have got by studying these systems.

The calculation from the mapping method that Hynninen and Dijkstra (2003) have proposed indicates that the coexistence packing fraction for BCC and fluid is $\eta^{BCC}_{coex} = 0.0900$ and $\eta^{fl}_{coex} = 0.0896$, respectively. To confirm this calculation, similar to the FCC case, we have performed MD simulations in the NVT ensemble for bulk BCC and fluid around the expected coexistence packing fraction. We have calculated the total pressure of these systems which are presented in figure 6.16. The inset of this figure confirms that these coexistence values are accurate.

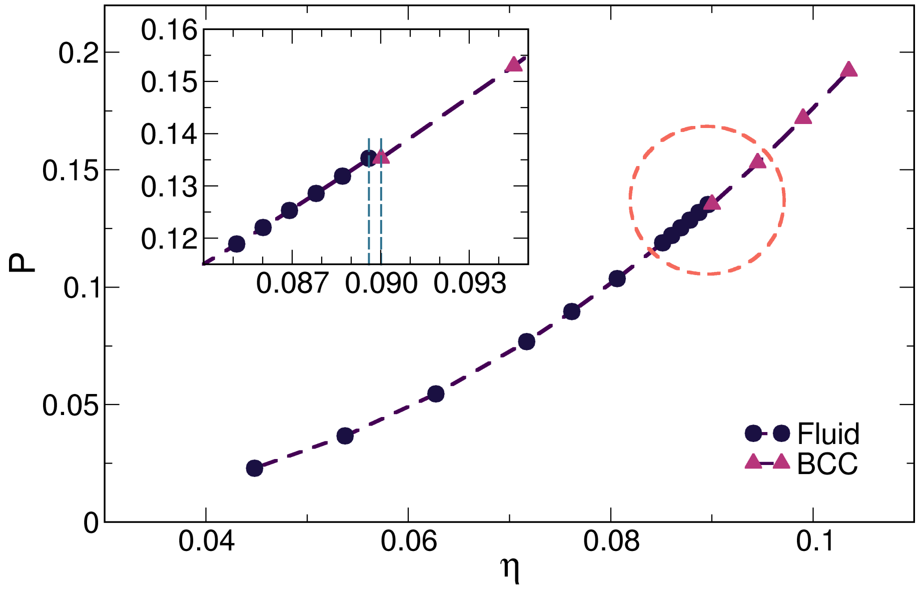

Figure 6.16: shows the calculated total pressure for bulk BCC and fluid systems of table 6.2. The inset indicates that two considered coexisting system have the same pressure and it means that our estimation of coexistence densities are correct.

So far, we have observed that the FCC crystals in confinement of flat hard walls are stable, while the corresponding fluids showed pre-freezing even at densities below coexistence. Now, we want to understand and study the behavior of the BCC crystals and fluids in a pair of parallel flat hard wall confinement. To this end, first, we consider BCC crystals with different densities equal to or higher than the coexistence density $\eta^{BCC}_{coex} = 0.0900$ for which we have already given the geometry in table 6.2. Two parallel flat hard walls are positioned at the boundaries of these systems in the z-direction. As in the confined FCC case, we defined the interaction between BCC particles and these hard walls via Eq. (3.2). To see if these confined systems are showing any phase transitions and study their behavior, we have produced the number density profile $\rho(z)$ for each density.

Figure 6.17 shows the normalized number density profiles $\frac{\rho(z/L_z)}{\bar{\rho}}$ for BCC(111) at coexistence $\eta^{BCC}_{coex} = 0.0900$ and a high density BCC crystal with $\eta = 0.1035$. In the upper part of the figure which belongs to the BCC crystal at coexistence,

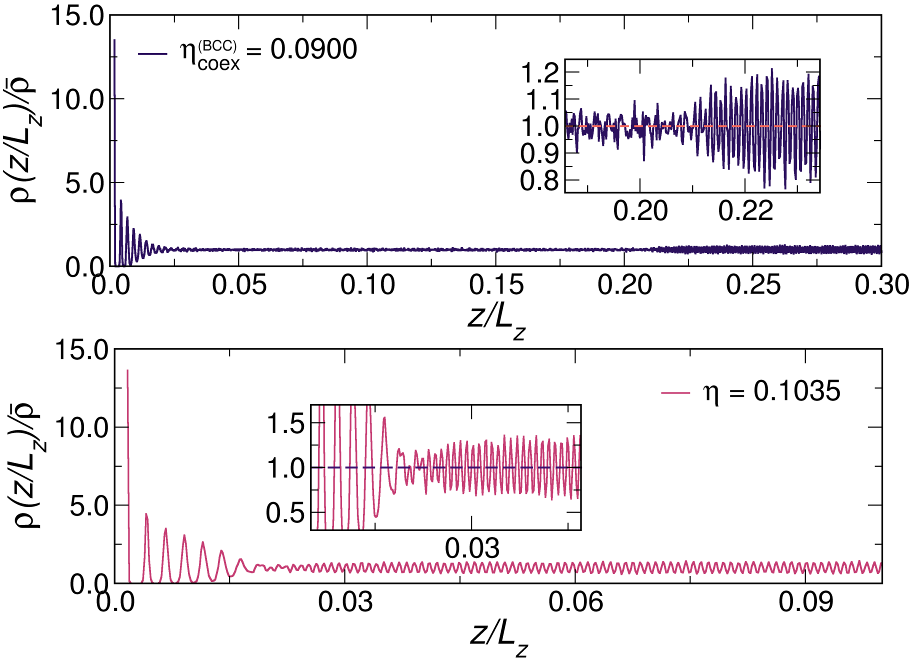

Figure 6.17: shows the normalized number density profile $\frac{\rho(z/L_z)}{\bar{\rho}}$ for coexistence BCC with $\eta^{BCC}_{coex} = 0.0900$ and a 15% higher density BCC crystal with $\eta = 0.1035$. Both profiles consist of high-density layers close the wall, BCC crystal in the middle and a melted area between them.

one can see that the layering has happened near the hard walls and the density of the first layer is extremely high. Later on, we should survey to see if the formation of this highly dense layer is due to a phase transition, or it is just an amorphous layer. Right after these layers, there is an area with a lower density corresponding to the density of the bulk fluid. In the middle of the profile the density becomes higher, and it is equal to the bulk BCC crystal density which suggests that in the middle of the box the BCC(111) crystal remains stable. The bottom part of figure 6.17 shows the density profile for a high-density of the BCC(111) crystal with $\eta = 0.1035$ (15% higher than coexistence), and we can see that at this specific density the area which has the density of the bulk fluid is smaller than the coexistence case and the big part of the BCC(111) crystal is still stable.

By now, we have understood that some transition has happened inside the confined BCC crystals and so the question about the nature of these transitions arises. We have calculated the local bond order parameters like q_4q_4, q_6q_6, $\bar{q}_4$ and $\bar{q}_6$ which help us to identify the structure and nature of these transitions for the BCC(111) crystals in confinement.

Figure 6.18 consists of snapshots which show the BCC(111) crystals for both coexistence $\eta^{BCC}_{coex} = 0.0900$ and the high density $\eta = 0.1035$ in confinement. We have examined each configuration via two different approaches for the calculation of bond order parameter, and we colored the particle according to the color maps of figures 5.5 and 5.5. From this figure (see figs. 6.18a and 6.18c), one can see that

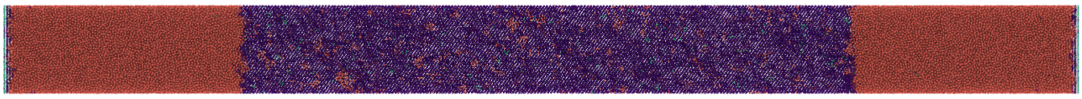

(a) $\eta = 0.0900$, Ten Wolde, Ruiz-Montero, and Frenkel (1995) approach

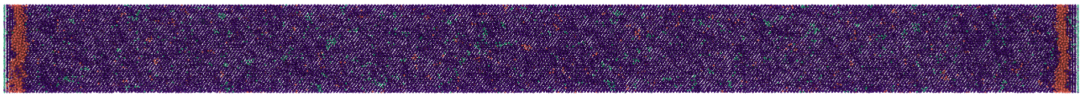

(b) $\eta = 0.1035$, Ten Wolde, Ruiz-Montero, and Frenkel (1995) approach

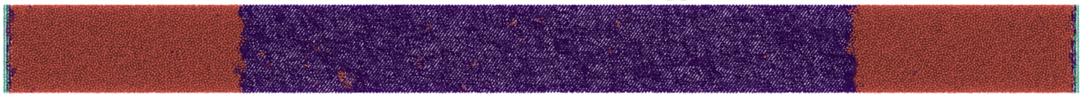

(c) $\eta = 0.0900$, Lechner and Dellago (2008) approach

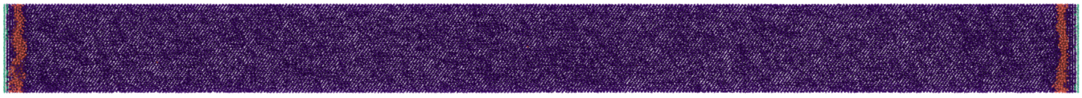

(d) $\eta = 0.1035$, Lechner and Dellago (2008) approach

Figure 6.18: shows the structure analysis of the BCC crystals confined between parallel flat hard walls.

our observation from the number density profiles is correct and there is a phase transition in the system. We can already see that in the confined coexistence BCC(111) there is a big area which corresponds to the low-density part of the density profile. These particles are red and identified as fluid particles according to the $q_4q_4 - q_6q_6$ and $\bar{q}_4 - \bar{q}_6$ maps. So the first transition is the phase transition from a BCC(111) crystal to a fluid, approximately with the bulk density. This transition happened at densities higher than the melting point, so we call this phenomenon pre-melting. As we have already understood from the number density profiles, there is layering in the vicinity of the hard walls. The structure analysis via calculation of bond order parameters shows that some of these layers have a FCC structure which we show as green particles, but later we will study these layers closely to see if they have any specific structure or they are just a combination of different phases. Moreover, in the middle of the configuration, the particles are violet which means that the BCC crystal in the center is stable. Figs. 6.18b and 6.18d show the snapshots of a high-density BCC crystal and indicate that for higher density the melted part of the system will be narrower and as a result, the BCC part is more stable. Same as the coexistence, there is evidence of pre-freezing at the wall which will be discussed in more detail below.

Since we have observed a transition in the vicinity of the wall, the next analysis is to look at the first layer close to the hard walls. To this end, we have illustrated the 2D snapshots of the first layers close the wall as well as pictures of a slice of the configuration in z-direction with width of 10σ which consists of the layers. These figures help us to understand the structure of the layers close to the hard walls and more specifically how the particles are ordered in the first layers.

Figure 6.19 shows a slice of the systems with width of 10σ and packing fractions of $\eta^{BCC}_{coex} = 0.0900$ and $\eta = 0.1035$ as well as a 2D snapshot of the first

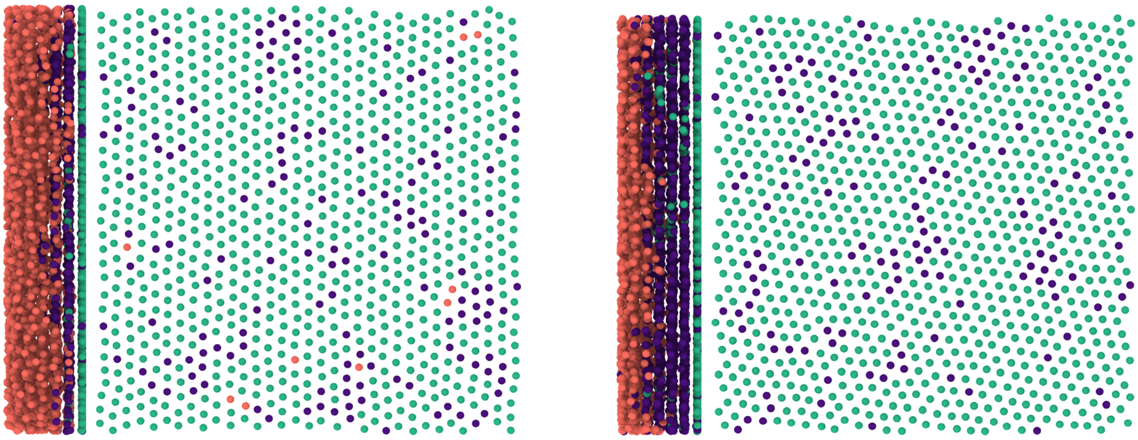

(a) $\eta = 0.1397$, Ten Wolde, Ruiz-Montero, and Frenkel (1995) approach

(b) $\eta = 0.1508$, Ten Wolde, Ruiz-Montero, and Frenkel (1995) approach

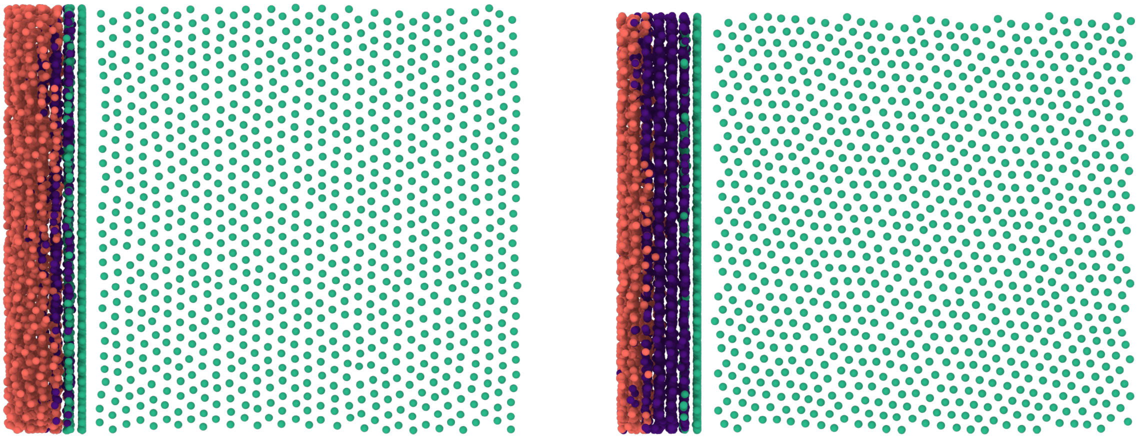

(c) $\eta = 0.1397$, Lechner and Dellago (2008) approach

(d) $\eta = 0.1508$, Lechner and Dellago (2008) approach

Figure 6.19: shows a slice of BCC crystal with width of $\sim 10\sigma$ as well as the first layer of the crystal close to the hard walls. the upper part (a and b)of the plot exhibits the system at coexistence and a higher density which are analyzed via $q_4q_4 - q_6q_6$ plane and the bottom part (c and d) are the one which their structures are studied by $\bar{q}_4 - \bar{q}_6$ plane. This comparison shows that the Lechner and Dellago (2008) approach is more efficient in the case of confined BCC crystals.

layer near the hard walls. Figures 6.19a and 6.19c show that for the coexistence BCC(111) with $\eta^{BCC}_{coex} = 0.0900$, we observe some BCC particles between the melted area and the walls, but by looking at the 2D snapshot we can see that the first layer is a hexagonal layer and the other layers are mostly combinations of different phases and so we consider these layers as amorphous layers. The impressive part is that in the high-density system with $\eta = 0.1035$, there are several layers of BCC crystals right after the narrow melted area (figures 6.19b and 6.19d) which indicates that after a time the melted area due to the high density of the system and their long-range interaction with image particles would crystallize back to the BCC structure. It means that in this system we have BCC-fluid and BCC-FCC interfaces. Moreover, the 2D snapshot confirms that at high density the first layer is entirely hexagonal.

In the FCC case, we have observed that the confined fluids between flat hard walls even for lower densities experience pre-freezing of the hexagonal layers in the vicinity of the walls. Moreover, in the confined BCC crystal the same phenomena at the wall happen. Now we study the fluids at the BCC-fluid coexistence line between a pair of flat hard walls. The main question is whether we observe any phase transition in this case and if yes, from where this transition will start and more important, what is the nature of that.

To this end, we have placed a pair of flat hard walls at the boundaries of the simulation box in z-direction. The position of these walls should be such that the density of the fluid in the middle should be equal to the bulk density. We have performed a series of molecular dynamics simulations for 2×10^6 step with a time step of $\delta = 0.001\tau$ ($\tau = \sqrt{m\sigma^2/\varepsilon}$) for each fluid system. For keeping the temperature constant, we have used the Berendsen thermostat with a time constant of 0.2τ. The geometry of these systems is presented in table 6.2.

To study the behavior of the fluid at the BCC-fluid coexistence path, we can investigate the density profiles of these systems. By averaging over 1000 configuration during each simulation, we can calculate the number density profile $\rho(z)$ in z-direction. Figure 6.20 shows the normalized density profiles of the fluids in z-direction $\frac{\rho(z/L_z)}{\bar{\rho}}$. By studying these density profiles, it turns out that similar to the FCC-fluid coexistence line some high dense layers form in the vicinity of the flat hard walls. Moreover, the left inset shows that the density of these layers increases by the increment of the packing fraction η. The right inset of the figure indicates that after the layering the density of the systems is equal to their bulk densities which rationalize our choice of the wall positions.

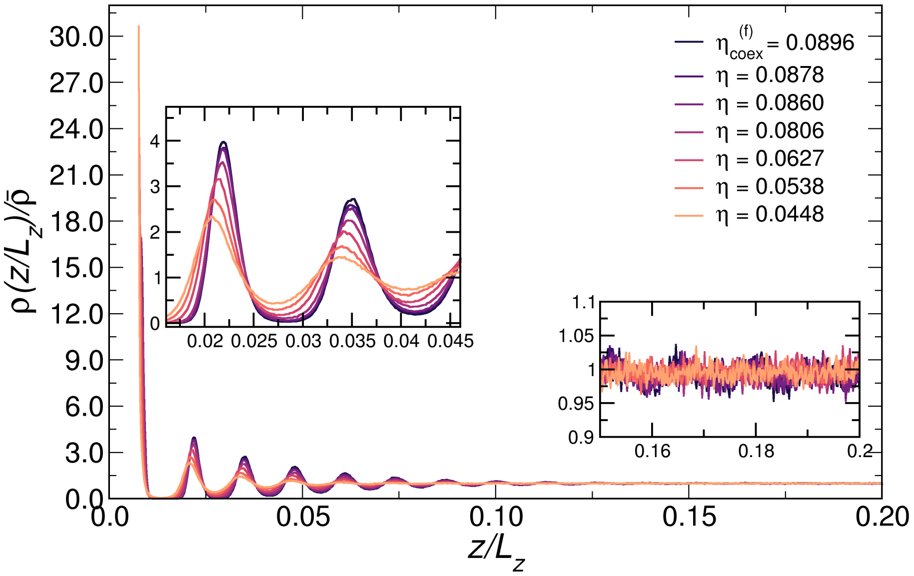

Figure 6.20: shows the density profiles for the BCC-fluid coexistence line (fluid part). These density profiles indicate the formation of dense layers in the vicinity of the hard walls and the inset shows that as we should expect the density at the middle of the system is equal to the bulk density.

The full snapshot of the coexistence fluid $\eta^{fl}_{coex} = 0.0896$ in figure 6.21 shows that the formation of the layers near the hard walls have some specific structures.

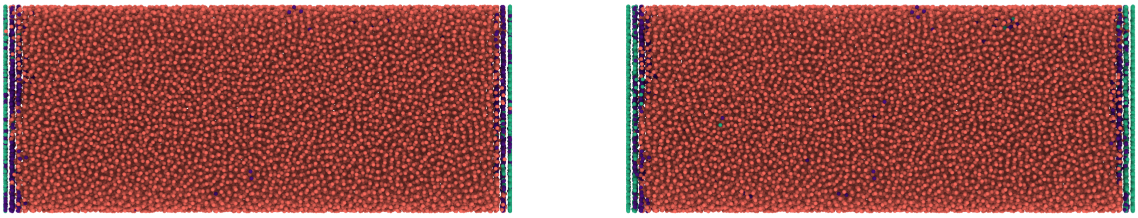

(a) $\eta = 0.1366$, Ten Wolde, Ruiz-Montero, and Frenkel (1995) approach

(b) $\eta = 0.1366$, Lechner and Dellago (2008) approach

Figure 6.21: shows the snapshots of the confined fluid at coexistence with packing fraction $\eta^{fl}_{coex} = 0.1366$. These snapshots which are resulted from structure analysis via local order parameters confirmed that the formed layers close to the flat hard walls have a specific FCC or BCC order.

Figure 6.21a is colored based on the $q_4q_4 - q_6q_6$ map and figure 6.21b corresponds to the $\bar{q}_4 - \bar{q}_6$ color map. From both approaches, one can understand that the hexagonal layer is formed in the vicinity of the hard walls but the second one indicates at least two hexagonal layers.

To obtain a better understanding of these transformations, we can look at the first layers which are formed in the vicinity of the walls. The inspection of the 2D snapshot of the first layers also confirms the previous observations. Figure 6.22c and 6.22f show the structure of the first layers at coexistence,

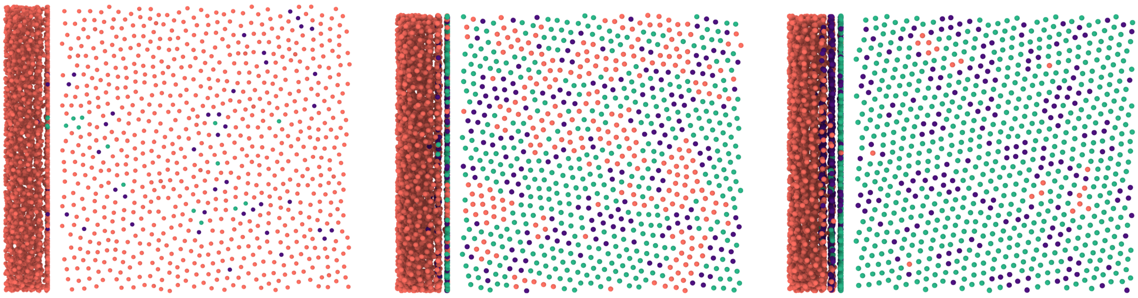

(a) $\eta = 0.0448$, Ten Wolde, Ruiz-Montero, and Frenkel (1995) approach

(b) $\eta = 0.0806$, Ten Wolde, Ruiz-Montero, and Frenkel (1995) approach

(c) $\eta^{fl}_{coex} = 0.0896$, Lechner and Dellago (2008) approach

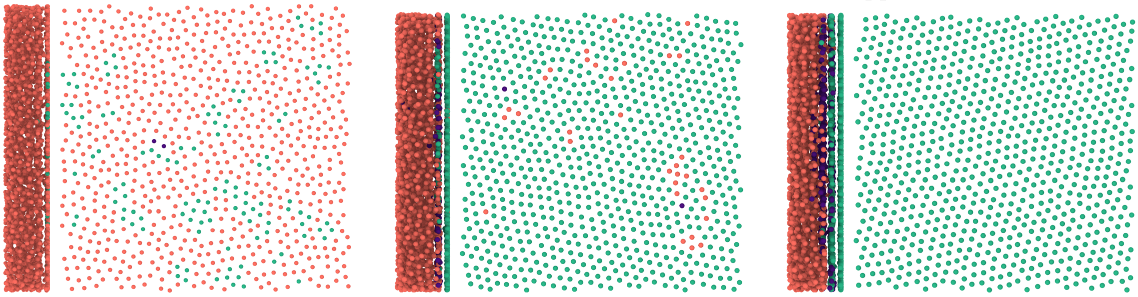

(d) $\eta = 0.0448$, Lechner and Dellago (2008) approach

(e) $\eta = 0.0806$, Lechner and Dellago (2008) approach

(f) $\eta^{fl}_{coex} = 0.0896$, Lechner and Dellago (2008) approach

Figure 6.22: shows the structure analysis of the first layer of fluid in hard walls confinement for the coexistence and systems with 10 and 50 % lower densities. The top snapshots belong to the calculation of $q_4q_4 - q_6q_6$ plane, and the bottom ones correspond to the $\bar{q}_4\bar{q}_6$. These snapshots indicate that at the coexistence $\eta^{fl}_{coex} = 0.0896$ and lower densities like $\eta = 0.0806$ the hexagonal layers are formed but around 50% lower than coexistence these layers are amorphous.

$\eta^{fl}_{coex} = 0.0896$. But even far from coexistence, one can observe these hexagonal layers. Figure 6.22b and 6.22e, show the hexagonal layer which is formed near the wall at a packing fraction of $\eta = 0.0806$ which is $\sim 10\%$ lower than the coexistence density. If we consider densities well below the coexistence, we can observe the amorphous layers in the vicinity of the hard walls. Figure 6.22a and 6.22d display 2D snapshots of the first layer at $\eta = 0.0448$ which is $\sim 50\%$ lower than the coexistence value. So one can see that these layers are amorphous.

Now that we have observed that the fluids in the fluid-BCC path are forming the hexagonal layers in the vicinity of the walls, we can investigate the 2D packing fraction η_{2D1st} of these layers and compare them with BCC crystals. These 2D packing fractions of the first layer η_{2D1st} which are illustrated in figure 6.23 indicate that the packing fraction of the first formed layer in the vicinity of the hard walls is increasing by the increment of the bulk packing fraction η. Note that η_{2D1st} in the case of formed hexagonal layers is close to η_{2D1st} for the BCC crystals.

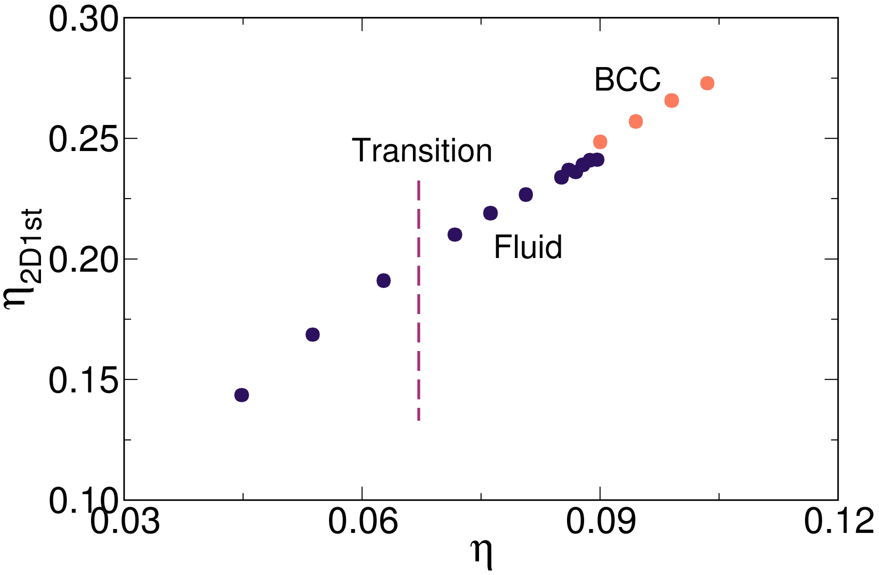

Figure 6.23: shows the 2D packing fraction of the first layer η_{2D1st} for BCC-fluid coexistence line at $\kappa\sigma = 2.0616$ and $\beta\varepsilon = 81$.

Moreover, by considering the average order parameter $q_6 q_6$ for the first formed layer (see figure 6.24)) we confirm the transition happens in densities which is already presented by figure 6.23.

To calculate interfacial free energies between fluid and wall, we have performed the thermodynamic integration scheme as introduced in chapter 4. As it has been already mentioned to employing thermodynamic integration, we need a system without phase transition along the thermodynamic path. So in the systems that are presented in figure 6.24 we can calculate interfacial free energies just for the system on the left-hand side of the transition line. These systems have

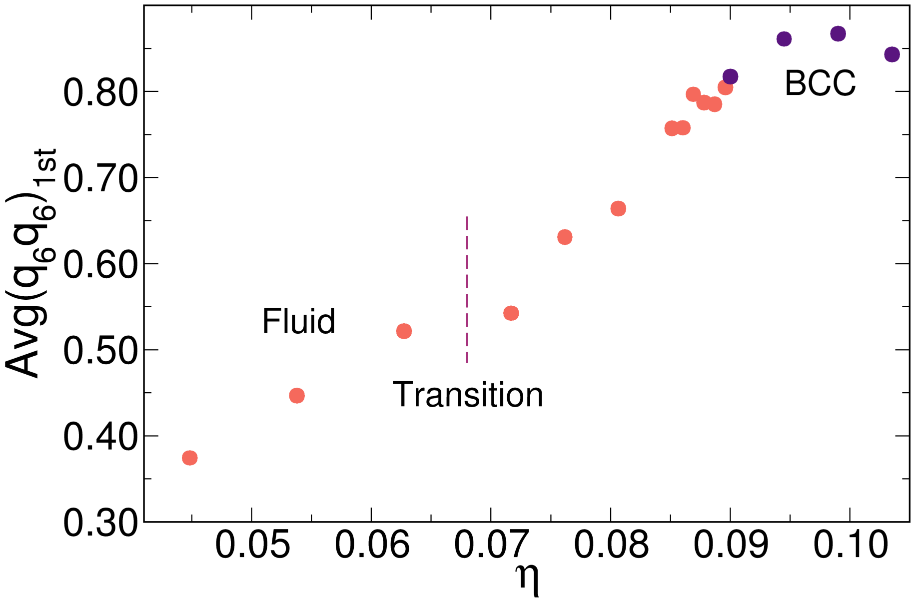

Figure 6.24: shows the average of $q_6 q_6$ for the first layer in the vicinity of the wall for BCC crystals and corresponding fluids. The result is in agreement with transition line in figure 6.23.

packing fractions of $\eta = 0.0627$, $\eta = 0.0538$, $\eta = 0.0448$ which are 30, 40 and 50% lower than the coexistence density, respectively. The Hamiltonian of these fluids

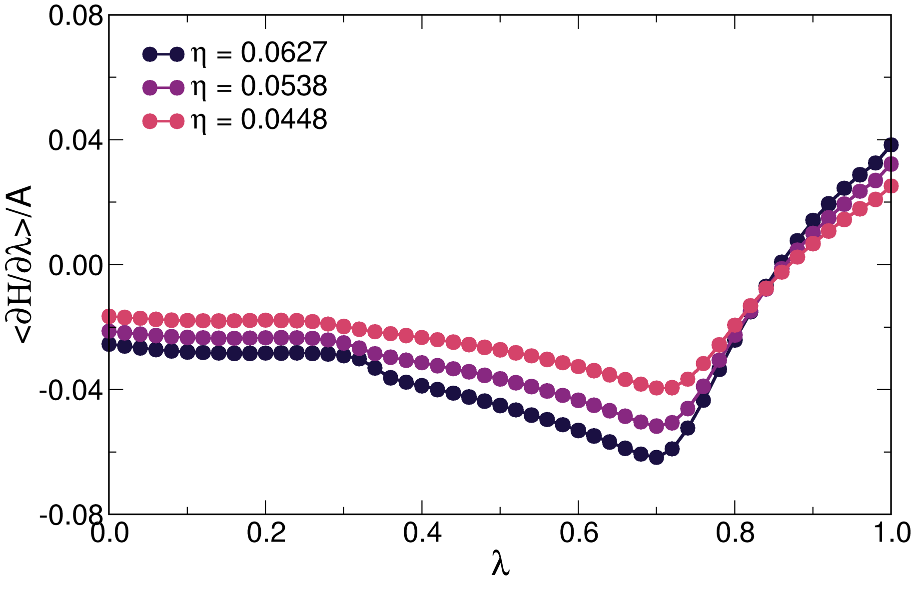

Figure 6.25: shows the calculated integrand for the fluids that does not show any transition in confinement. These smooth and reversible integrand show some negative values which can lead to the negative interfacial energies and are due to the competition between different type of interaction ranges.

in confinement of hard walls is given by

$$\mathcal{H}(\lambda) = \sum_{i=1}^{N} \frac{\vec{p}_i^{\,2}}{2m} + U_{p-p} + U_{p-im}(\lambda) + U_{p-fw}(\lambda) \quad . \tag{6.10}$$

where the $U_{p-im}(\lambda)$ describes the interaction of the bulk particles with image particles as follows

$$\begin{aligned} U_{p-im}(\lambda) &= \sum_{i,im} u_{i,im}(\lambda, r_{i,im}) \\ u_{p-im}(\lambda, r) &= (1-\lambda)^2 \, \varepsilon \left(\frac{\exp\left[-\kappa\sigma\left(r/\sigma - 1\right)\right]}{r/\sigma} + \left(\frac{\sigma}{r}\right)^{256} \right) \end{aligned} \tag{6.11}$$

and the interaction of the particles with flat hard walls U_{p-fw} which can be defined as

$$\begin{aligned} U_{p-fw}(\lambda) &= \sum_{i} u_{p-fw}(\lambda, z_i) \\ u_{p-fw}(\lambda, z) &= \lambda^4 (1-\lambda)^4 \, \varepsilon \left[\left(\frac{\sigma}{z}\right)^{12} + \left(\frac{\sigma}{L_z - z}\right)^{12} \right] \\ &+ \lambda^{128} \left(\frac{1+\lambda}{2}\right)^{196} \varepsilon \left[\left(\frac{\sigma}{z}\right)^{256} + \left(\frac{\sigma}{L_z - z}\right)^{256} \right] \end{aligned} \tag{6.12}$$

By calculating the partial derivative of the Hamiltonian with respect of λ we can calculate the corresponding integrand for each system.

$$\frac{\partial \mathcal{H}}{\partial \lambda} = \frac{\partial U_{p-im}(\lambda)}{\partial \lambda} + \frac{\partial U_{p-w}(\lambda)}{\partial \lambda} \tag{6.13}$$

These derivatives have two terms, the particle-image contribution,

$$\frac{\partial u_{p-im}(\lambda, r)}{\partial \lambda} = -2(1-\lambda) \left(\frac{\exp\left[-\kappa\sigma\left(r/\sigma - 1\right)\right]}{r/\sigma} + \left(\frac{\sigma}{r}\right)^{256} \right) \tag{6.14}$$

and the partial derivative of the particle-wall interaction,

$$\begin{aligned} \frac{\partial u_{p-w}(\lambda, z)}{\partial \lambda} &= \left[4\lambda^3 (1-\lambda)^3 (2\lambda - 1) \right] \varepsilon \left[\left(\frac{\sigma}{z}\right)^{12} + \left(\frac{\sigma}{L_z - z}\right)^{12} \right] \\ &+ \left[128\lambda^{127} \left(\frac{1+\lambda}{2}\right)^{196} + \lambda^{128} \frac{196}{2^{196}} (1+\lambda)^{195} \right] \\ &\times \varepsilon \left[\left(\frac{\sigma}{z}\right)^{256} + \left(\frac{\sigma}{L_z - z}\right)^{256} \right] \quad . \end{aligned} \tag{6.15}$$

The obtained integrands are shown in figure 6.25 and indicate that these paths are mostly located in the negative part of the y-axis ($\langle \frac{\partial H}{\partial \lambda} \rangle / A$).

By integration over the integrands of figure 6.25, we can calculate the interfacial free energy of the fluid for the hard walls, γ_{fw}. The calculated values of γ_{fw} are shown in figure 6.26. As we could expect from the integrands, these values are negative. The reason is that we have two different types of interaction ranges, long-ranged interactions in the bulk and short-range ones with the hard walls. To form the interface, the interaction between the bulk particle and image particles has a bigger contribution than hard wall interaction which causes the effective attraction by the walls and thus the negative values for γ_{fw} .

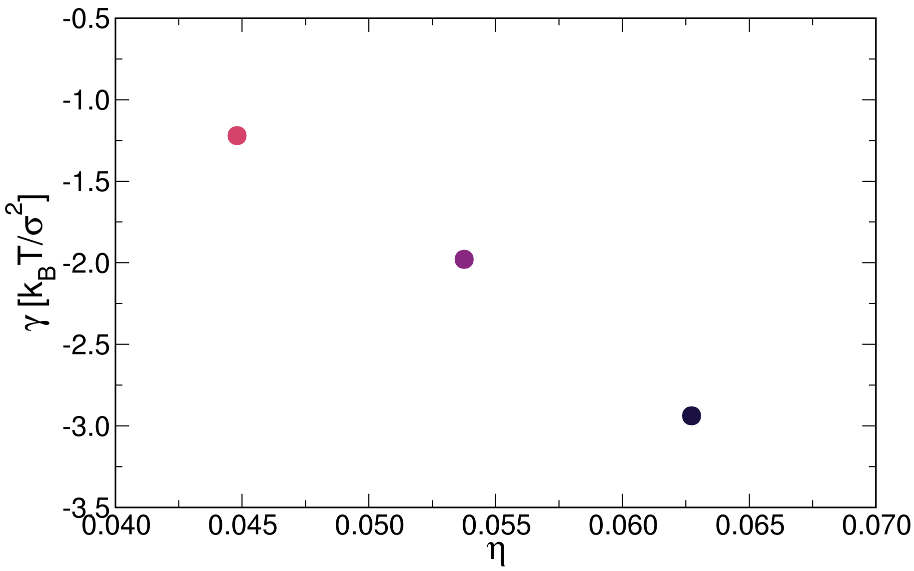

Figure 6.26: shows the calculated value for fluid-wall interfacial free energy γ_{fw} at packing fractions $\eta = 0.0627$, $\eta = 0.0538$ and, $\eta = 0.0448$. The values of γ_{fw} are negative because the particle-image contribution can overcome the share of particle-wall interaction in the forming of these interfaces.

6.2 Charged Walls Confinement

So far we have studied the FCC, BCC, and corresponding fluid phases in confinement of a pair of flat hard walls. We have observed that the FCC crystal is stable in confinement but the BCC crystals are melting in the vicinity of the hard walls and this phenomenon happens even slightly above the coexistence density. Moreover, in both cases for the fluid phase, we have observed the pre-freezing in terms of hexagonal layers. Now we can examine another type of the wall which has a longer interaction range. This type of wall is called a charged wall which is introduced by Karanikas, Dzubiella, Moncho-Jordá, and Louis (2008) and is defined as

$$u_{fw} = \begin{cases} \varepsilon \exp\left[-\kappa\left(z - \frac{\sigma}{2}\right)\right] & \text{for } r \geqslant \frac{\sigma}{2} \\ \infty & \text{for } r < \frac{\sigma}{2} \end{cases} \tag{6.16}$$

also, as it has already described in chapter 3, we substitute the hard-core interaction by an inverse power law potential as follows

$$\begin{aligned} u^{c}_{p-fw} = {} & \varepsilon \exp\left[-\kappa\left(L_z - z - \frac{\sigma}{2}\right) - \kappa\left(z - \frac{\sigma}{2}\right)\right] \\ & + \varepsilon\left[\left(\frac{\sigma}{z}\right)^{256} + \left(\frac{\sigma}{L_z - z}\right)^{256}\right] \end{aligned} \tag{6.17}$$

This section is divided into two parts. The first part belongs to the FCC-fluid path in the phase diagram of the hard-core Yukawa system (see figure 6.1) and we are confining these systems by a pair of parallel charged wall. In the second part, we will put the systems alongside the BCC-fluid path (see figure 6.14) between the same charged walls.

6.2.1 FCC-Fluid coexistence Line

Here, we considered the FCC crystal with packing fraction $\eta_{coex}^{FCC} = 0.1397$ and the crystals with up to 10% higher density than coexistence. The geometry of these systems is the same for the corresponding case of flat hard walls and shown in table 6.1.

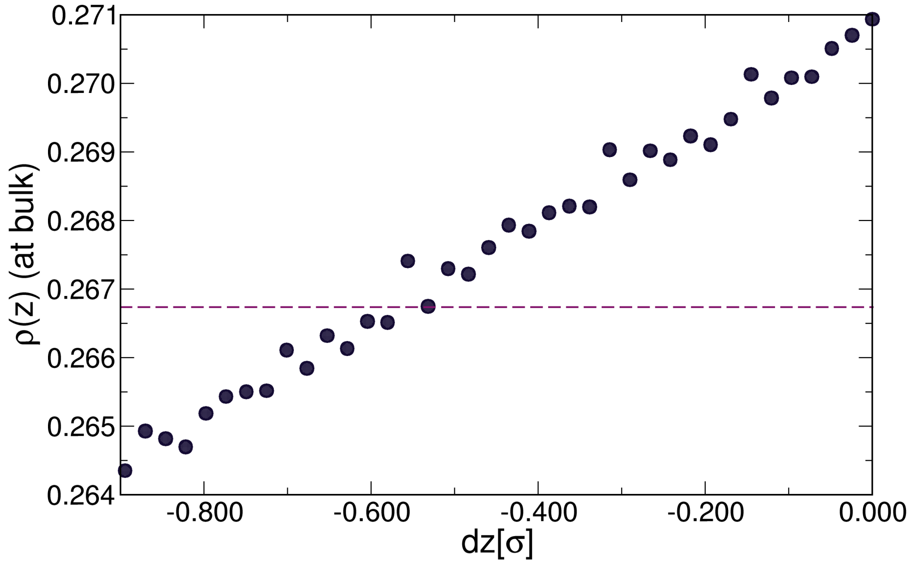

Figure 6.27: shows average density of the FCC crystal in the middle of the simulation box for the different value of wall position dz at coexistence $\eta_{coex}^{FCC} = 0.1397$. It turns out the best place for the placing of the charged walls is $dz = 0.53\sigma$, in which the average density of the system is equal to the bulk density.

To study the behavior of any system in confinement we need to place the walls such that the density of the system in the middle should be equal to the bulk density. Since the charged walls have a long interaction range, we have performed simulations to obtain the optimum position of the charged walls. We have examined a FCC(111) crystal consisting of $N = 19440$ particles with the length of $L_x = 31.3867\sigma$, $L_y = 30.2019\sigma$ and $L_z = 76.8815\sigma$ with different wall positions dz. We have run the independent MD simulation with NVT ensemble for 2×10^6 steps in each wall positions dz. As one can see in figure 6.27, it turns out if we put the walls in distance of $dz = 0.53\sigma$ then the density of the system in middle corresponds to the bulk density as $\eta_{coex}^{FCC} = 0.2667$.

By considering the above result for the positioning the wall, now we are considering the FCC(111) crystals of table 6.1 to study their behavior in confinement of parallel flat charged walls. We run the MD simulation for each packing fraction η for 1.5×10^6 steps with a time step of $dt = 0.001$, and we extract the resulting configuration every 1000 steps to be able to calculate the density profiles with high accuracy.

Figure 6.28 shows the density profiles of the coexistence FCC(111) crystal with packing fraction $\eta_{coex}^{FCC} = 0.1397$ as well as a FCC(111) crystal with the density 8%

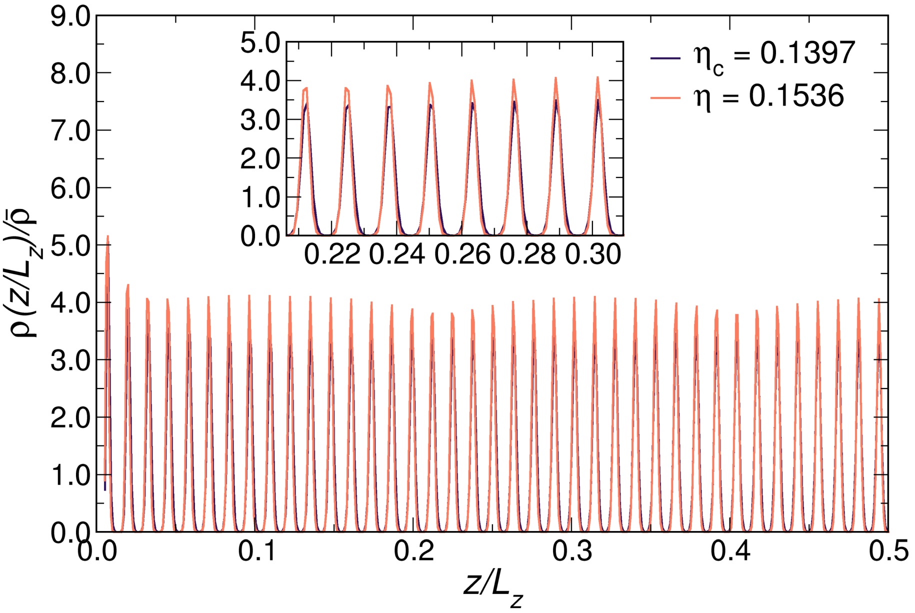

Figure 6.28: it shows the density profiles for the FCC(111) crystal confined by flat charged walls at coexistence $\eta^{\mathrm{FCC}}_{\mathrm{coex}} = 0.1397$ and a 8% higher density $\eta = 0.1508$. These profiles show that only the lattice distance in the vicinity of the wall has changed and the FCC is completely stable in this confinement.

higher than the coexistence density $\eta = 0.1508$. One can see that approximately the FCC(111) is stable in charged wall confinement and just the lattice distance is changed slightly in the vicinity of the charged walls.

Besides the density profile, we can use bond order parameters to observe what exactly happened in these confined FCC crystals. As we can understand and

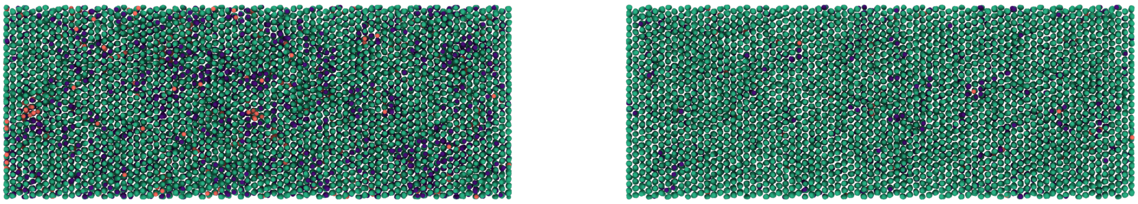

(a) $\eta^{\mathrm{FCC}}_{\mathrm{coex}} = 0.1397$, Ten Wolde, Ruiz-Montero, and Frenkel (1995) approach

(b) $\eta = 0.1508$, Ten Wolde, Ruiz-Montero, and Frenkel (1995) approach

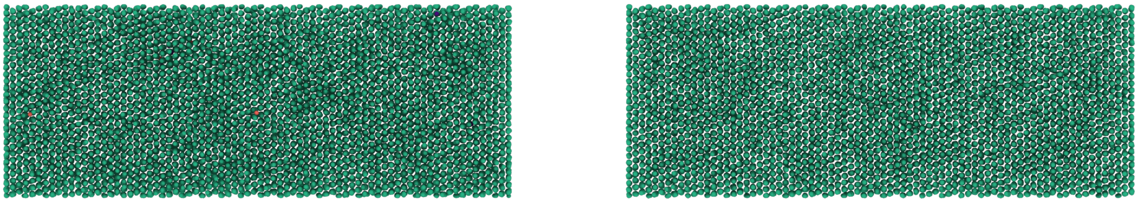

(c) $\eta^{\mathrm{FCC}}_{\mathrm{coex}}$, Lechner and Dellago (2008) approach

(d) $\eta = 0.1508$, Lechner and Dellago (2008) approach

Figure 6.29: It shows the structure analysis of the FCC(111) crystals confined between parallel flat charged walls. The snapshots indicate the $q_4q_4 - q_6q_6$ plane scheme shows some BCC and fluid at the coexistence configuration (sub-fig (a)) while the $\bar{q}_4 - \bar{q}_6$ identify that more than 99% of the particle has the FCC structure(sub-fig (c)). Sub-figs (b) and (d) are showing the structure of the highly compact system at $\eta = 0.1508$ which is just a relaxed FCC crystal.

expect from the density profiles of figure 6.28, by calculation of local bond order parameters and with consideration of $q_4q_4 - q_6q_6$ and $\bar{q}_4 - \bar{q}_6$ maps, the final configuration in both coexistence and high-density FCC crystal in flat charged walls confinement are stable. Figure 6.29 shows the structure of these confined crystals. Now we can take a look at the structure of these crystals in the vicinity of the charged walls.

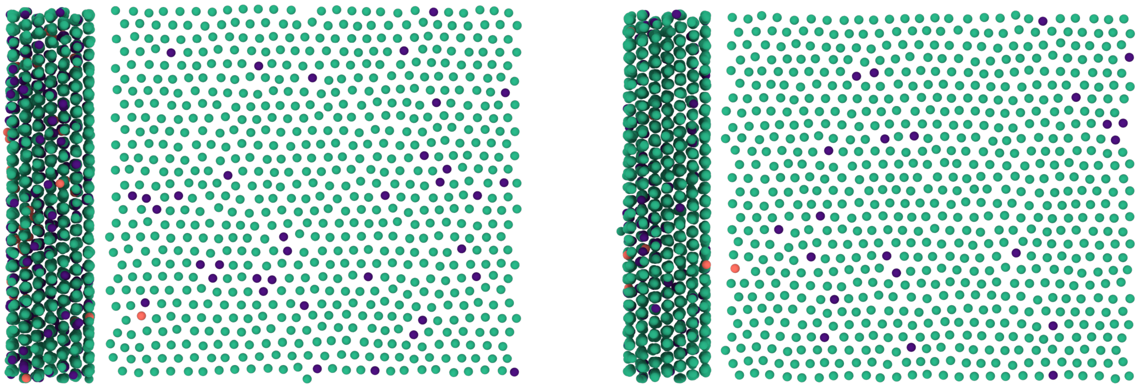

(a) $\eta_{coex}^{FCC} = 0.1397$, Ten Wolde, Ruiz-Montero, and Frenkel (1995) approach

(b) $\eta = 0.1508$, Ten Wolde, Ruiz-Montero, and Frenkel (1995) approach

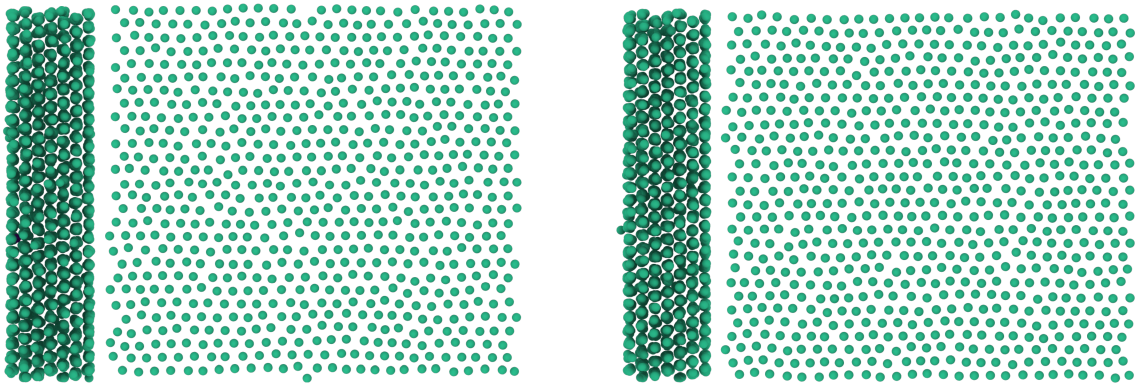

(c) $\eta_{coex}^{FCC} = 0.1397$, Lechner and Dellago (2008) approach

(d) $\eta = 0.1508$, Lechner and Dellago (2008) approach

Figure 6.30: It shows a slice of FCC(111) crystal with a width of ~ 10σ as well as the first layer of the crystal close to the hard walls. The upper part (a and b)of the plot exhibits the system at coexistence, and a higher density which is analyzed via $q_4q_4 - q_6q_6$ plane and the bottom part (c and d) are the ones which their structures are studied by $\bar{q}_4 - \bar{q}_6$ plane. This comparison shows that the Lechner and Dellago (2008) approach is more efficient in the case of confined FCC crystals.

Studying the structure of the first layers in the vicinity of the charged walls via local bond order parameters shows that these layers have a hexagonal structure. The top part of figure 6.30 belongs to the 2D snapshot of the first layer which is colored according to the $q_4q_4 - q_6q_6$ map, and the bottom part shows the same layer which is studied via the $\bar{q}_4 - \bar{q}_6$ map.

Now that we understand that the FCC crystals confined between the charged walls are showing the same behavior as the flat hard wall confinement, we like to investigate the behavior of the fluid phase in charged wall confinement. We have seen that these fluids are showing the formation of pre-freezing layers at flat hard walls, but the question is whether this is will happen in charged wall case?

To study the behavior of the fluid in flat charged wall confinement, same as the FCC case, we need to find out the best position for the charged walls. To analyze the finite size effects we have considered four different sizes (regarding the number of particles) of the fluid at coexistence with $\eta^{fl}_{coex} = 0.1366$. Table 6.3 gives the geometry of these systems.

Phase	N	η	$L_x \times L_y \times L_z$
Fluid	9408	0.1366	$25.9628 \times 25.6965 \times 63.5956$
	19440		$31.6205 \times 30.4269 \times 77.4541$
	34848		$38.6473 \times 36.5122 \times 94.6661$
	56784		$45.6741 \times 42.5976 \times 11.8782$
FCC	19440	0.1397	$31.3867 \times 30.2019 \times 76.8815$

Table 6.3: Packing fractions, size and geometries of different simulated hard-core Yukawa fluid and FCC systems which are in confinement by a pair of parallel walls.

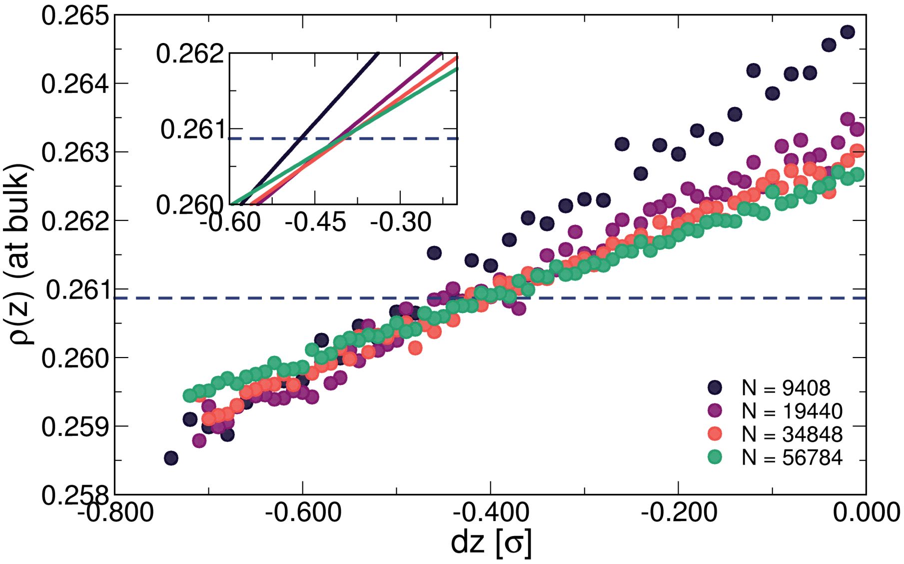

Figure 6.31: It shows average density of the fluid in the middle of the simulation box for the different value of wall position dz at coexistence $\eta^{fl}_{coex} = 0.1366$. The averages have been calculated for different system size. It turns out the best place for the placing of the charged walls is $dz \approx 0.4\sigma$, in which the average density of the system is equal to the bulk density.

Figure 6.31 shows the calculated value of the average density for several system sizes at coexistence with $\eta^{fl}_{coex} = 0.1366$. We have examined the position of the walls from $dz = 0.75$ to the boundary of the system ($dz = 0$). It turns out that if we increase the system size the accuracy of positioning the wall position is also increasing. The inset of figure 6.31 indicates that an optimum position for placing the charged wall would be $dz \approx 0.4\sigma$.

By knowing the optimum place of the flat charged walls, we have confined the fluid that is already described in table 6.1 by two parallel structureless charged walls. To this end, we performed the MD simulation in the NVT ensemble with constant temperature $k_BT = 0.01234568$. The simulations has been done for

1.5×10^6 steps with time step $dt = 0.001$. Again we store the configuration every 1000 steps to calculate the density profiles. The density profiles are shown in figure 6.32 and indicate that several layers are formed near the charged walls. The density of these layers are much lower than in the hard wall case, and they increase with increasing packing fraction η. Moreover, we can see that the density of the fluid in the middle is equal to the density of the bulk fluid (right inset), which rationalizes our choice of the position of the charged walls.

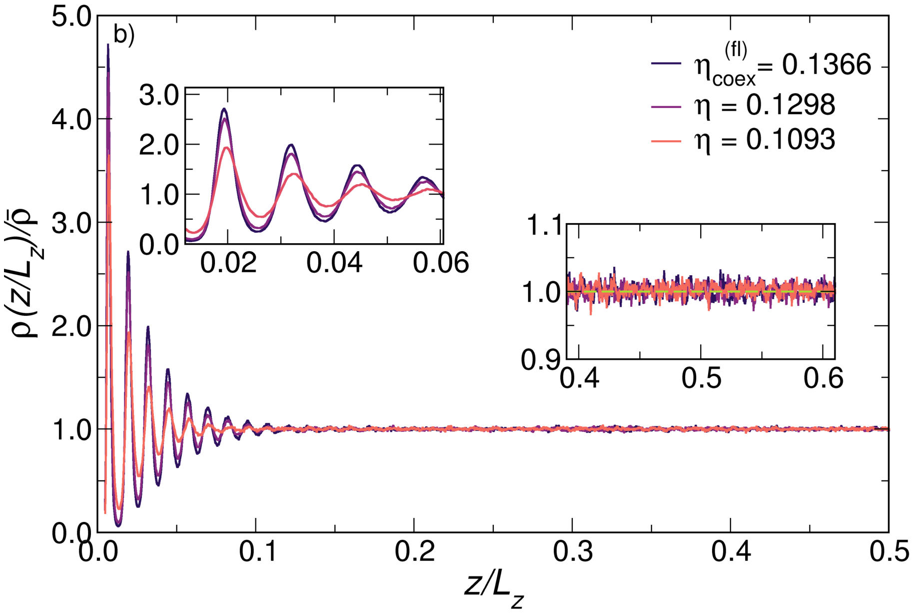

Figure 6.32: It shows the density profile of fluids confined by the flat charged walls which consists of systems with packing fraction $\eta_{coex}^{fl} = 0.1366$, $\eta = 0.1298$ and $\eta = 0.1093$. The profiles show the formation of several layers in the vicinity of the charged walls, but the density of these layers is much lower than the case of flat hard walls.

Now that we observed that there are some dense layers near the charged walls, we can see their exact structures via the bond order parameters. The snapshots of the fluid at coexistence $\eta_{coex}^{fl} = 0.1366$ in figure 6.33 show that as one can also see in figure 6.32, some layers are formed in the vicinity of the flat charged walls, but they do not have any specific orders.

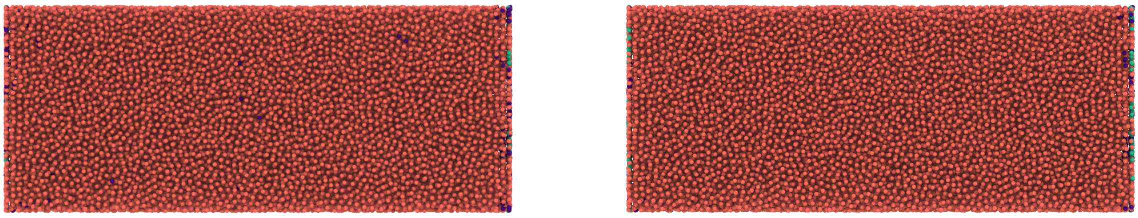

(a) $\eta = 0.1366$, Ten Wolde, Ruiz-Montero, and Frenkel (1995) approach

(b) $\eta = 0.1366$, Lechner and Dellago (2008) approach

Figure 6.33: shows the snapshots of the confined fluid at coexistence with packing fraction $\eta_{coex}^{fl} = 0.1366$. These snapshots which are resulted from structure analysis via local order parameters indicate that from this point of view, there are some BCC and FCC particles but to understand if the formed layers in the vicinity of the walls have an order or not, one should take a closer look to these layers.

To be specific about amorphous or ordered layers in the vicinity of the charged walls, the idea is to investigate them by calculation of bond order parameters and identify their structure via $q_4q_4 - q_6q_6$ and $\bar{q}_4 - \bar{q}_6$ maps. So, one should study the structure of the first layers which has been formed near the flat charged walls. In figure 6.34, we have shown that the first layer that is formed near the charged walls at $\eta = 0.1093$ is an amorphous layer (figures 6.34a and 6.34d) which is similar to the hard walls case. Here we are far from coexistence and particles are not strongly attracted to the walls. If we consider the system with density ($\eta = 0.1298$) below coexistence, for which we have seen pre-freezing in the presence of hard walls, we can see that the first layer of the system with charged walls is also an amorphous layer (figures 6.34b and 6.34e). One explanation for this phenomenon could be that now that we have a long-range particle-wall interaction, particles are not attracted to the walls which leads to less dense (in comparison to the hard wall confinement) and disordered layers. Surprisingly, even at coexistence 6.34c and 6.34f), we can still observe that the first layers consist of the same portion of fluid and hexagonal particles, which make this layer more amorphous than ordered.

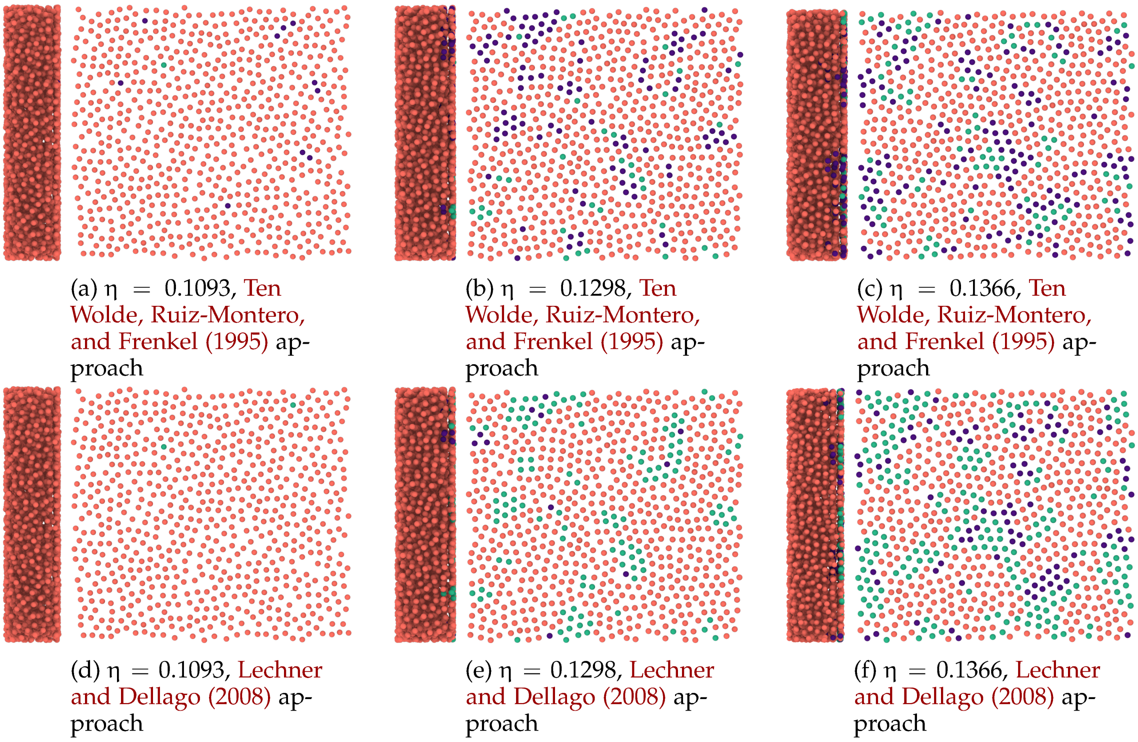
(a) $\eta = 0.1093$, Ten Wolde, Ruiz-Montero, and Frenkel (1995) approach

(b) $\eta = 0.1298$, Ten Wolde, Ruiz-Montero, and Frenkel (1995) approach

(c) $\eta = 0.1366$, Ten Wolde, Ruiz-Montero, and Frenkel (1995) approach

(d) $\eta = 0.1093$, Lechner and Dellago (2008) approach

(e) $\eta = 0.1298$, Lechner and Dellago (2008) approach

(f) $\eta = 0.1366$, Lechner and Dellago (2008) approach

Figure 6.34: It shows the structure analysis of first layer of liquids in confinement for the system with packing fraction of $\eta^{fl}_{coex} = 0.1366$, $\eta = 0.1298$ and $\eta = 0.1093$. The top sub-figures are analyzed via $q_4q_4 - q_6q_6$ plane and the bottom sub-figure are studied by $\bar{q}_4 - \bar{q}_6$ calculations.In lowest density system $\eta = 0.1093$ the first layer is a amorphous layer, while at $\eta = 0.1298$ the first layer shows some hexagonal networks but in total the layer is amorphous and even at coexistence density $\eta^{fl}_{coex} = 0.1366$ there is no evidence of hexagonal layers.

So far we have understood that the layers close to the hard walls do not have any specific orders. Now we can calculate the 2D packing fraction η_{2D1st} for this to see if this calculation confirms our findings from bond order parameters. We have calculated the 2D packing fraction of this layer, η_{2D1st}, and compared

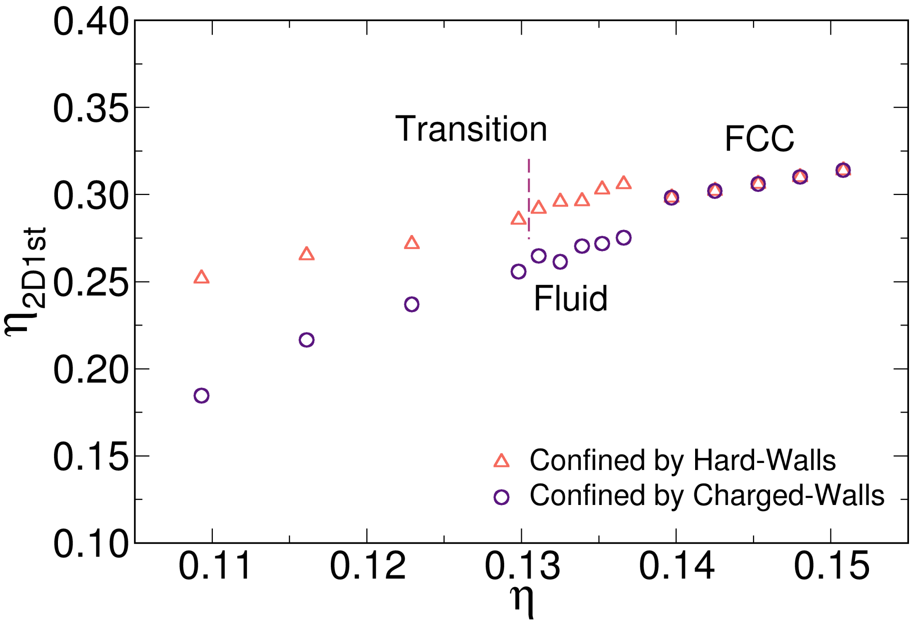

Figure 6.35: shows the 2D packing fraction of the first layer η_{2D1st} for both FCC and fluids as a function of bulk packing η for both hard and charged walls confinement. It indicates that the density of the first layer for the FCC(111) crystal is not changing while for the fluid the density of the first layer in charged walls confinement is considerably lower than the hard walls case.

it with a similar system which is confined by flat hard walls. This comparison (figure 6.35) shows that the density of the first layer both near the hard and charged walls for the FCC(111) crystals are similar and it does make sense since FCC(111) crystal is stable in both confinements. Moreover, one can see that the density of the first layer in the fluid case decreases for the charged wall confinement. This can explain that we can observe the hexagonal layers for hard walls case in charged wall confinement and it shows that the hard walls are more attractive for the fluid particles than the charged walls.

Moreover, one can examine these amorphous layers by calculation of an average of local order parameter q_6q_6 for them. Figure 6.36 shows the average values of q_6q_6 for the first layer near the wall and indicates that these layers should have similar structures and are disordered.

Now that by studying the structure of the FCC and fluid we are sure that there is no evidence of any transition, we can use our thermodynamic integration method to calculate the interfacial energy of FCC-wall interfaces γ_{cw}, and fluid-wall interfaces, γ_{fw}. The Hamiltonian of the FCC(111) crystal which is confined by two parallel charged walls is defined as

$$\mathcal{H}(\lambda) = \sum_{i=1}^{N} \frac{\vec{p}_i^{\,2}}{2m} + U_{p-p} + U_{p-im}(\lambda) + U_{p-fw}(\lambda) \quad . \tag{6.18}$$

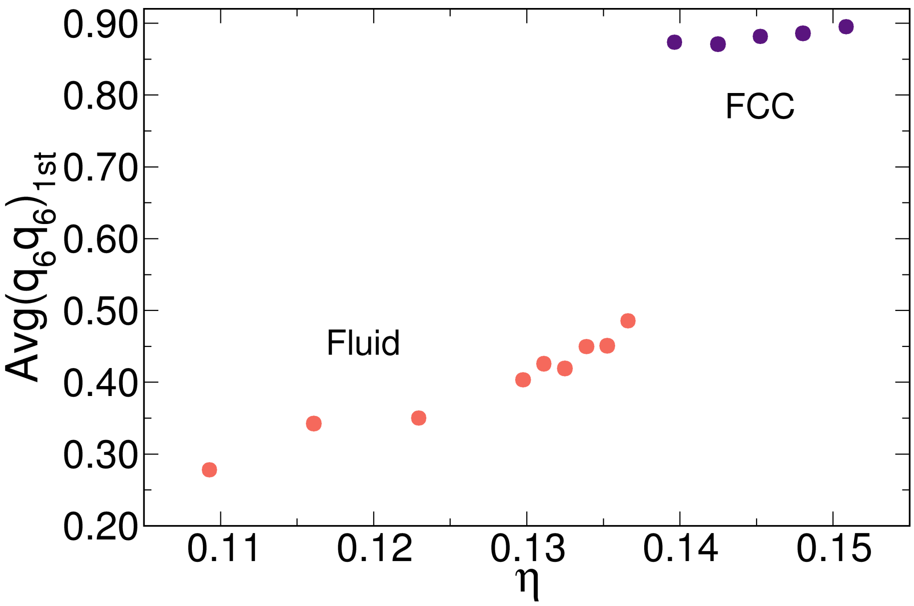

Figure 6.36: shows the average of $q_6 q_6$ for the first layer in the vicinity of the charged wall for FCC crystals and corresponding fluids. The result is in agreement with transition line in figure 6.35.

where the interaction between bulk particles and image particles can be described by

$$\begin{aligned} U_{p-im}(\lambda) &= \sum_{i,im} u_{i,im}(\lambda, r_{i,im}) \\ u_{p-im}(\lambda, r) &= (1-\lambda)^2 \,\varepsilon \left(\frac{\exp\left[-\kappa\sigma\left(r/\sigma - 1\right)\right]}{r/\sigma} + \left(\frac{\sigma}{r}\right)^{256} \right) \end{aligned} \tag{6.19}$$

and the interaction of the particles with flat charged wall is formulated as follows

$$\begin{aligned} U_{p-fw}\left(\lambda\right) &= \sum_{i} u_{p-fw}\left(\lambda, z_i\right) \\ u_{p-fw}\left(\lambda, z\right) &= \lambda^4 \left(1-\lambda\right)^4 \varepsilon \left[\left(\frac{\sigma}{z}\right)^6 + \left(\frac{\sigma}{L_z - z}\right)^6 \right] \\ &+ \lambda^4 \left(\frac{1+\lambda}{2}\right)^4 \varepsilon \left[\exp\left[-\kappa\left(L_z - z - \frac{\sigma}{2}\right) - \kappa\left(z - \frac{\sigma}{2}\right)\right] + \left[\left(\frac{\sigma}{z}\right)^{256} + \left(\frac{\sigma}{L_z - z}\right)^{256} \right] \right] \end{aligned} \tag{6.20}$$

By calculating the partial derivative of the Hamiltonian with respect to λ and then integrating its average over λ from the $\lambda = 0$ which corresponds to the bulk state and $\lambda = 1$ which describes the confined system, we can have access to the free energy difference between two steps. This partial derivative can be written as

$$\frac{\partial \mathcal{H}}{\partial \lambda} = \frac{\partial U_{p-im}\left(\lambda\right)}{\partial \lambda} + \frac{\partial U_{p-w}\left(\lambda\right)}{\partial \lambda} \tag{6.21}$$

So the partial derivative of the particle-image interaction is given by

$$\frac{\partial u_{p-im}(\lambda, r)}{\partial \lambda} = -2\left(1-\lambda\right) \left(\frac{\exp\left[-\kappa\sigma\left(r/\sigma - 1\right)\right]}{r/\sigma} + \left(\frac{\sigma}{r}\right)^{256} \right) \tag{6.22}$$

And the partial derivative of the interaction between bulk particles and charged walls is calculated as

$$\begin{aligned}\frac{\partial u_{p-fw}(\lambda, z)}{\partial \lambda} &= \left[4\lambda^3 (1-\lambda)^3 (2\lambda - 1)\right] \varepsilon \left[\left(\frac{\sigma}{z}\right)^6 + \left(\frac{\sigma}{L_z - z}\right)^6\right] \\ &+ \left[4\lambda^3 \left(\frac{1+\lambda}{2}\right)^4 + \lambda^4 \frac{4}{2^4} (1+\lambda)^3\right] \\ &\times \varepsilon \left[\exp\left[-\kappa\left(L_z - z - \frac{\sigma}{2}\right) - \kappa\left(z - \frac{\sigma}{2}\right)\right] + \left[\left(\frac{\sigma}{z}\right)^{256} + \left(\frac{\sigma}{L_z - z}\right)^{256}\right]\right] \quad .\end{aligned} \tag{6.23}$$

By using equations (6.22) and (6.23) we have performed thermodynamic integration simulations for the systems that are described in table 6.1. The simulation for each packing fraction has been done from the bulk state ($\lambda = 0$) and confined state ($\lambda = 1$) for 51 different values of λ. We have run these systems for 1.1×10^6 steps with a time step of $dt = 0.001$. After equilibration we have collected the data every 100 steps to calculate the corresponding values for $\frac{\partial \mathcal{H}}{\partial \lambda}$.

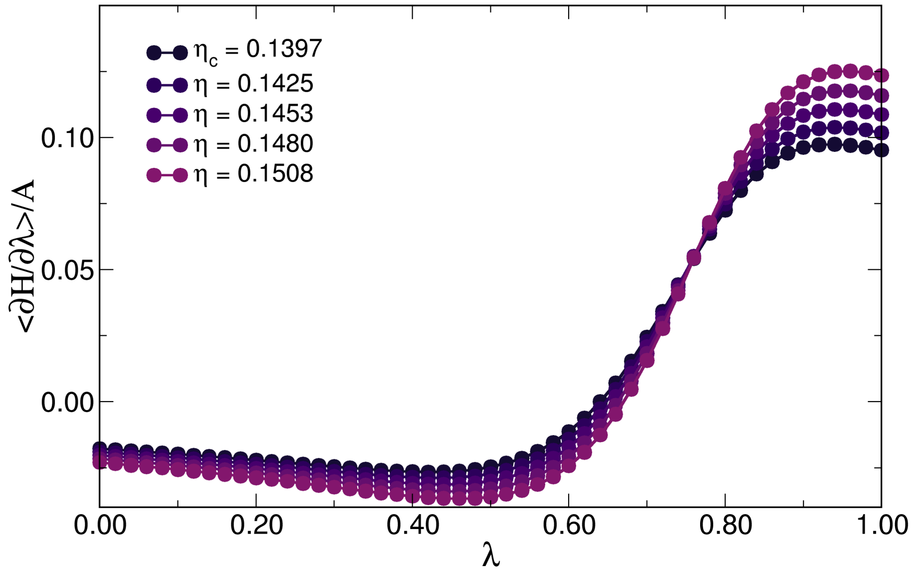

Figure 6.37: shows the calculated integrand for the FCC(111) crystal in confinement of flat charged walls. The major part of the integrands are positive and have direct dependency to increasing of packing fraction η.

These integrands for FCC(111) are shown in figure 6.37. In contrast to the hard wall case, here the major part of the integrands $\frac{\partial \mathcal{H}}{\partial \lambda}$ are positive, and they increase with increasing of the packing fraction η. In fact, since both interactions are long-ranged, now the particle-wall contribution has a higher contribution and particles are not attracted effectively to the walls which leads to the positive value of the integrands.

The parameterization of the thermodynamic integration for the fluid follows the same way as the FCC(111). However, here to get a smooth and reversible path we needed to optimize the position of the charged walls for each independent value of λ. Equation 6.24 shows the way that the charged wall are placed for the fluids.

$$z\prime(w) = z_w + [(1-\lambda)z_w\alpha_w] \qquad \text{for } \lambda > 0 \tag{6.24}$$

in which $\alpha_w = 0.1$ and z_w is the value that we have obtained from figure 6.31.

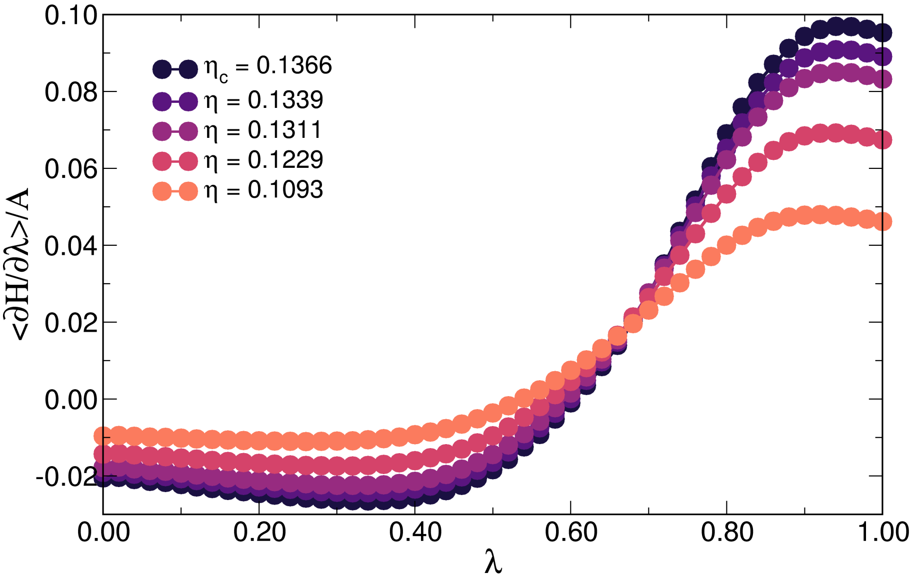

Figure 6.38: shows the calculated integrand for the fluid in confinement of flat charged walls. The major part of the integrands are positive and have direct dependency to increasing of packing fraction η.

The corresponding integrands for the fluids confined by the charged wall are presented in figure 6.38. Similarly, the significant value of these integrands is positive which is because the bulk particle-wall interaction has a large contribution of forming the interface between the fluid and charged walls.

Now we can calculate the free energy difference in both FCC(111) crystal and corresponding fluids from the integrand of figures 6.37 and 6.38, respectively.

Figure 6.39 represents the calculated values for FCC-wall energy, γ_{cw}, and fluid-wall energy, γ_{fw}. Since there is no evidence of the transition in flat charged walls confinement, the calculated values are reliable. Moreover, as we can also see in figures 6.37 and 6.38 the calculated values for γ_{cw} and γ_{fw} are positive.

As we have already mentioned, in addition to calculating the interfacial free energies, we can calculate the difference in entropy between the bulk system (FCC crystal and fluid) and confined system per particle ΔS. This value can lead us to understand if our systems tend to be more ordered or disordered since the discontinuity in entropy is a sign of a first order phase transition.

Figure 6.40 shows calculated the difference of entropy per particle $\Delta S/N$ for FCC(111) and fluid systems. This figure indicates that the difference in entropy between the bulk system (FCC crystal and fluid) and the confined system per particle, ΔS, is decreasing with increasing of packing fraction η, and it shows no discontinuity.

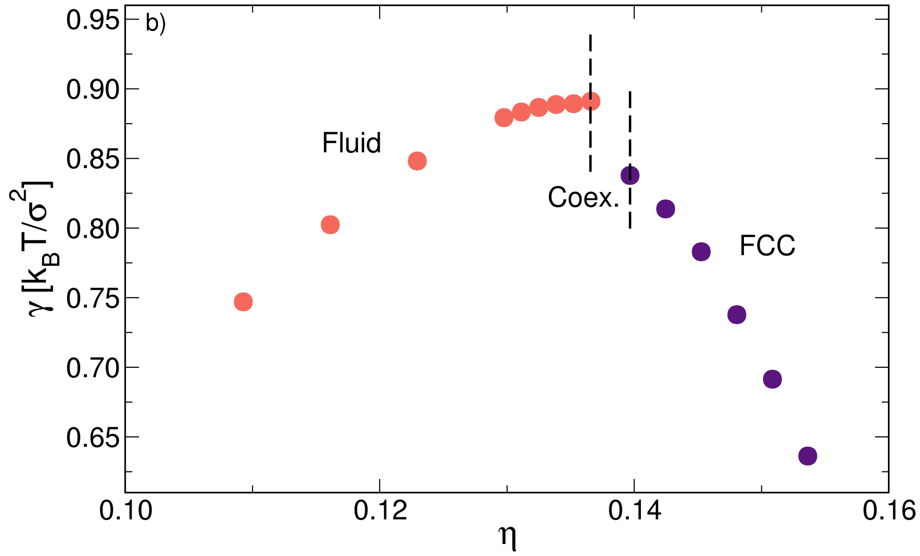

Figure 6.39: shows the calculated values for FCC-wall γ_{cw} and fluid-wallγ_{fw} interfacial free energy γ_{fw} for the corresponding fluids of FCC-fluid path in the hard-core Yukawa phase diagram. Since there is no evidence of transition, then all the values of γ_{cw} and γ_{fw} are reliable. Moreover, the interfacial free energy values are positive.

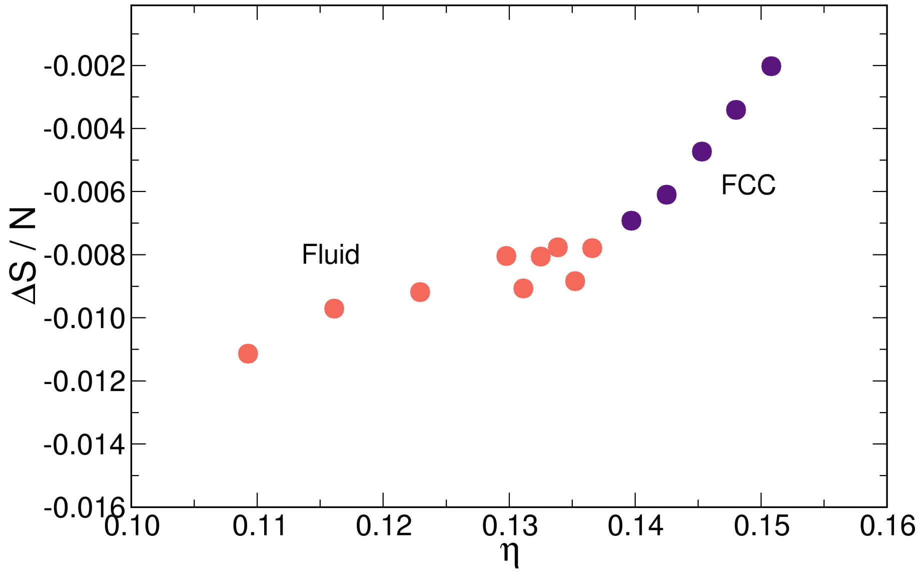

Figure 6.40: shows the difference of entropy between bulk system (FCC(111) crystal and fluid) and confine system per particle.

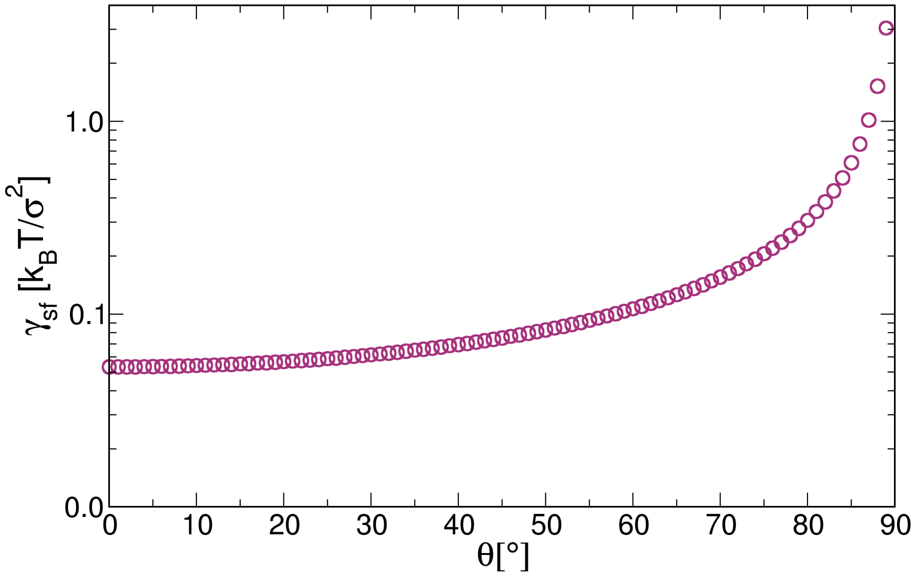

Figure 6.41: shows a rough estimation of relation between crystal-fluid interfacial free energy γ_{cf} and contact angle θ

So far, for the flat charged wall confinement we have seen that there is no evidence of pre-freezing and we could calculate the FCC(111)-wall and fluid-wall interfacial free energies. So regarding the Young's equation as follows

$$\gamma_{cf} \cos\theta = \gamma_{fw} - \gamma_{cw} \tag{6.25}$$

we can have a rough estimation about the relation between γ_{cf} and $\cos\theta$ which are crystal-fluid interfacial free energy and contact angle, respectively (see figure 6.41).

6.2.2 BCC-Fluid coexistence Line

So far we have seen that by confining the BCC(111) crystal between two parallel hard walls, some part of the crystal in the vicinity of the wall is melting and from this melted part hexagonal layers are formed at the wall.

Now, we consider the same system of BCC(111) particles, but we confine them by a pair of flat charged walls. The position of the walls is chosen such that the density of the BCC(111) crystal in the middle of the system will be equal to the bulk density and it is right before the first layer of the image particles. The geometry of these systems is described in table 6.4.

We have performed MD simulations in the NVT ensemble at the temperature $k_B T = 0.01234568$ and $\kappa\sigma = 2.0616$. The simulation has been done for 1×10^6 MD steps after the equilibration. Moreover, we have collected the configuration every 1000 steps to calculate an accurate density profile $\rho(z)$. The calculated density profiles for the BCC(111) at coexistence ($\eta_{coex}^{BCC} = 0.0900$) and the crystal with the density 20% higher than coexistence are presented in figure 6.42.

Phases	η	N	$L_x \times L_y \times L_z$
Fluid	0.0896	57344	51.3499 × 51.8820 × 126.9811
	0.0887		51.5222 × 52.0561 × 127.4032
	0.0878		51.6969 × 52.2326 × 127.8310
	0.0869		51.8739 × 52.4115 × 128.2646
	0.0860		52.0534 × 52.5928 × 128.7043
	0.0851		52.2354 × 52.7767 × 129.1501
	0.0806		53.1854 × 53.7365 × 131.4770
	0.0762		54.2084 × 54.7702 × 133.9829
	0.0717		55.3150 × 55.8882 × 136.6935
	0.0627		57.8327 × 58.4320 × 142.8607
	0.0538		60.8820 × 61.5130 × 150.3299
	0.0448		64.6968 × 65.3673 × 159.6742
BCC	0.0900	69360	54.4759 × 55.5029 × 668.5363
	0.0945		53.5970 × 54.6074 × 131.2852
	0.0990		52.7728 × 53.7677 × 129.2664
	0.1035		51.9962 × 52.9765 × 127.3642
	0.1080		51.2634 × 52.2299 × 125.5692

Table 6.4: Size and geometries of the simulated fluid and BCC systems, confined between charged walls.

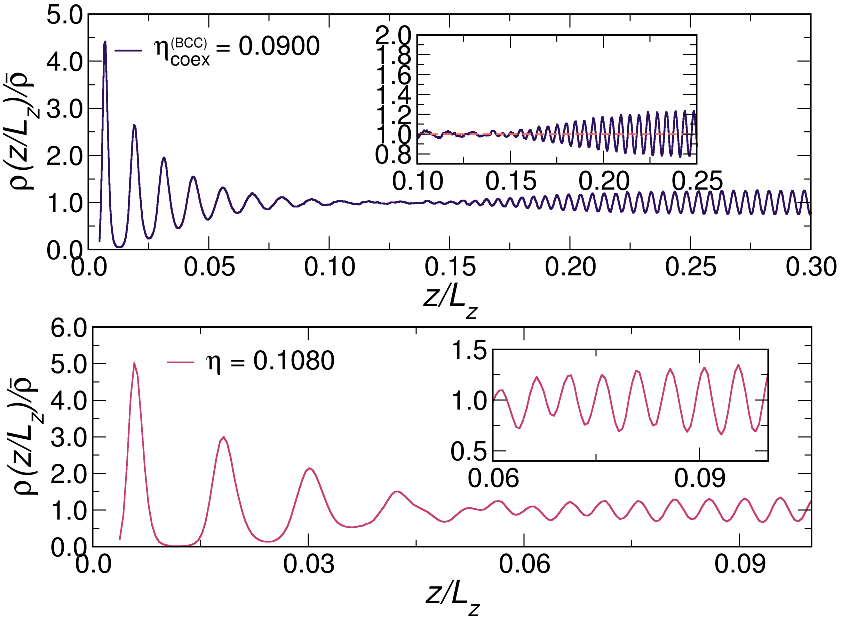

Figure 6.42: It shows the density profile of coexistence BCC(111) crystal with $\eta^{BCC}_{coex} = 0.0900$ and a high-density system with $\eta = 0.1080$ which both are confined by a pair of flat charged walls. At the coexistence on can see a melted area between the BCC crystal and the layers that are formed in the vicinity of the walls. This area for higher density becomes narrower.

The density profile of the BCC(111) with packing fraction $\eta^{BCC}_{coex} = 0.0900$ shows that the BCC crystal is melted in the area near the charged walls and apparently some layers which their density is higher than the bulk density are formed in the vicinity of the walls, and the rest of the BCC crystal remains stable in the middle of the system. Moreover, one can see that the density of the melted area is equal to that of the bulk fluid, $\eta^{fl}_{coex} = 0.0896$.

For higher density ($\eta = 0.1080$) the melted area is quite narrow, and it is not possible to calculate its density, but we can also see that the small number of layers with densities higher than the bulk density are formed near the charged walls and the rest is just BCC(111) crystal. The insets in both densities indicate that the density of the system in the middle is equal to the density of the bulk BCC crystal and shows that our choice for the position of the walls is accurate.

Now by using the local bond order parameter, we can understand each part of density profiles such as melted area and dense layers. Figure 6.43 shows the full snapshots of BCC(111) crystals with packing fraction of $\eta^{BCC}_{coex} = 0.0900$ and $\eta = 0.1080$. In the coexistence system, even from this point of view, it is evident that the formed layers in the vicinity of the charged walls are amorphous. However, at $\eta = 0.1080$ it seems that there are some hexagonal particles in the first layer, but it could also be a combination of different phases.

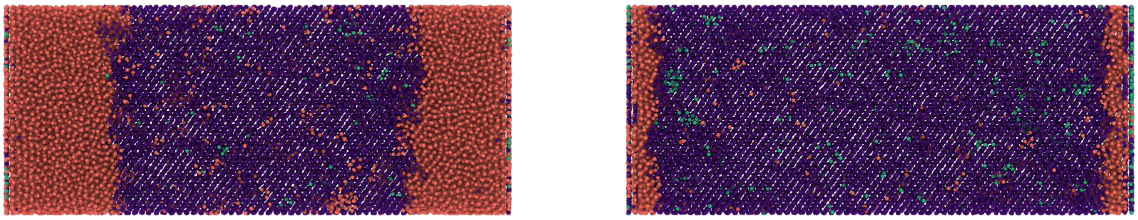

(a) $\eta^{BCC}_{coex} = 0.0900$, Ten Wolde, Ruiz-Montero, and Frenkel (1995) approach

(b) $\eta = 0.1080$, Ten Wolde, Ruiz-Montero, and Frenkel (1995) approach

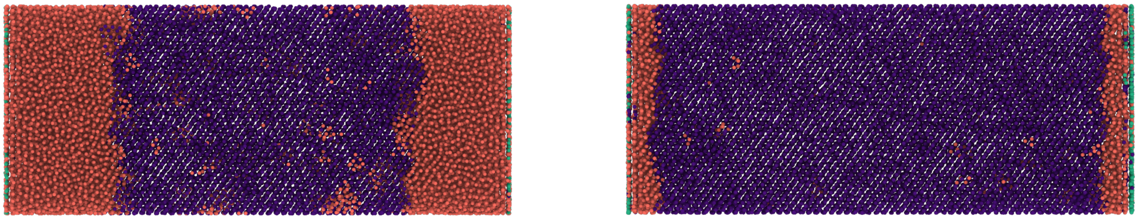

(c) $\eta^{BCC}_{coex} = 0.0900$, Ten Wolde, Ruiz-Montero, and Frenkel (1995) approach

(d) $\eta = 0.1080$, Lechner and Dellago (2008) approach

Figure 6.43: shows the structure analysis of the BCC crystals confined between parallel charged hard walls.

By looking at the 2D snapshot of the first layer which is formed in the vicinity of the charged walls in figure 6.44 we can understand that this layer at coexistence ($\eta^{BCC}_{coex} = 0.0900$) does not have any specific order and it is like an amorphous layer. However, at the packing fraction $\eta = 0.1080$, the $q_4q_4 - q_6q_6$ order parameters map indicates that the layer is just an amorphous one but if we analyze it with

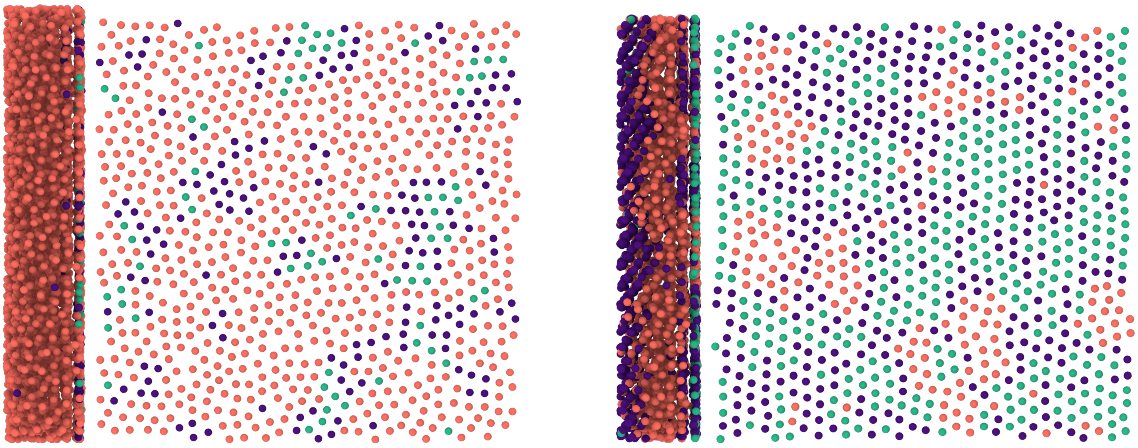

(a) $\eta = 0.0900$, Ten Wolde, Ruiz-Montero, and Frenkel (1995) approach

(b) $\eta = 0.1080$, Ten Wolde, Ruiz-Montero, and Frenkel (1995) approach

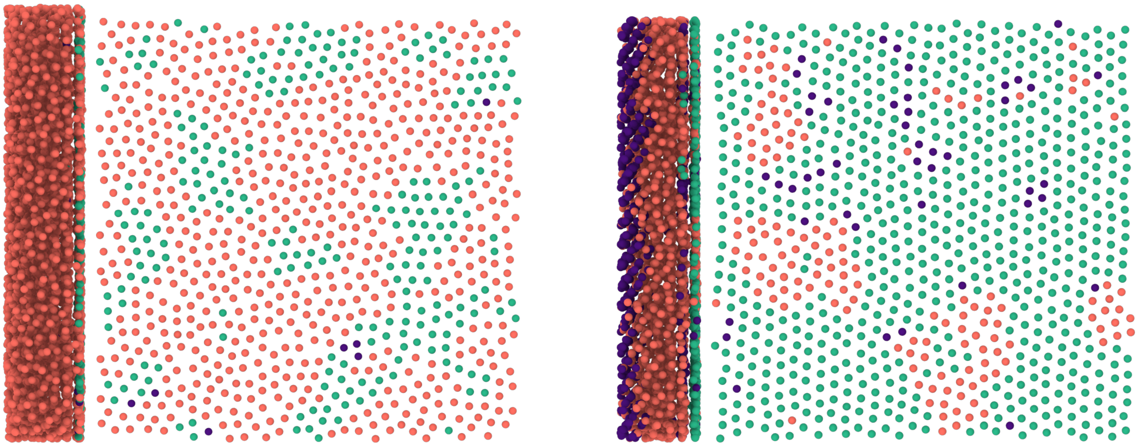

(c) $\eta = 0.0900$, Lechner and Dellago (2008) approach

(d) $\eta = 0.1080$, Lechner and Dellago (2008) approach

Figure 6.44: It shows a slice of BCC(111) crystal with a width of $\sim 10\sigma$ as well as the first layer of the crystal close to the flat charged walls. The upper part (a and b) of the plot exhibits the system at coexistence, and a higher density which is analyzed via $q_4 q_4 - q_6 q_6$ plane and the bottom part (c and d) are the ones which their structures are studied by $\bar{q}_4 - \bar{q}_6$ plane.

the calculation of $\bar{q}_4 - \bar{q}_6$, we can see that some part of this layer has a hexagonal structure.

If we go through the fluid part of BCC-fluid path and confine them between two parallel flat charged walls, we can still observe the formation of several layers near these walls. Figure 6.45 shows the density profiles of these fluid systems in contact with flat hard walls. In these density profiles, the formation of dense layers is confirmed, but this layer has less density than the ones in hard walls confinement. Moreover, from the inset, one can see that after these layers the density of the system is equal to the bulk density.

In figure 6.46 we present the snapshots of the confined fluid at coexistence $\eta^{fl}_{coex} = 0.0896$. These snapshots confirm that there are some particles with FCC or BCC structure inside the system and even in the layers that are formed in the vicinity of the walls, but from this perspective, it is not possible to extend them to the whole layer.

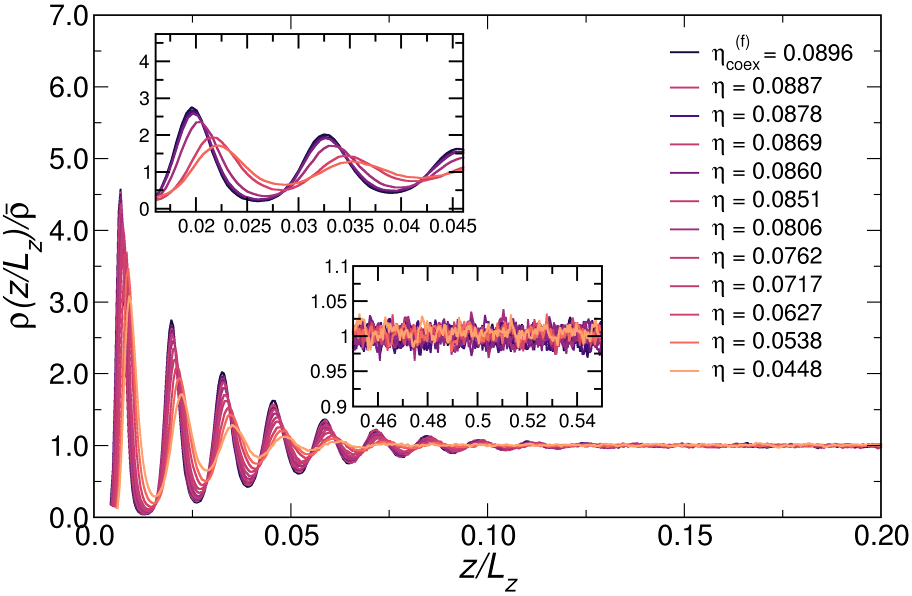

Figure 6.45: shows the density profiles for the BCC-fluid coexistence line (fluid part). These density profiles indicate the formation of dense layers in the vicinity of the charged walls and the inset shows that as we should expect the density at the middle of the system is equal to the bulk density.

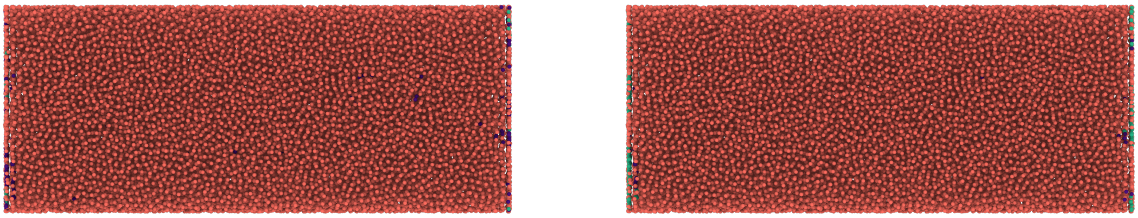

(a) $\eta = 0.1366$, Ten Wolde, Ruiz-Montero, and Frenkel (1995) approach

(b) $\eta = 0.1366$, Lechner and Dellago (2008) approach

Figure 6.46: shows the snapshots of the confined fluid at coexistence with packing fraction $\eta^{fl}_{coex} = 0.0896$. These snapshots which are resulted from structure analysis via local order parameters shows that in the formed layers close to the flat charged walls there are some ordered particles, but it is not obvious if one can extend this to the whole layer or not.

To have a better idea about the structure of the system, we can calculate the local bond order parameters for the first layer near the charged walls. Figure 6.47 shows a slice of the confined fluid with the width of 10σ for different density from coexistence to a system with a density that is 50% lower than the coexistence density as well as the snapshots of the first layers in the vicinity of the flat charged walls. As one can see in these snapshots even at coexistence, the first layer is an amorphous layer, and for lower density, this is even more pronounced.

Also, we can calculate the packing fraction of these layers η_{2D1st} as a function of η. These packing fractions are shown in figure 6.48. It turns out that the increment of the bulk density increases the density of the first layer and it shows that this density for the fluid is lower than the hard wall confinement while for the BCC(111) crystal it is equal to the hard wall one.

Same as FCC case we can confirm the results that we have obtained from

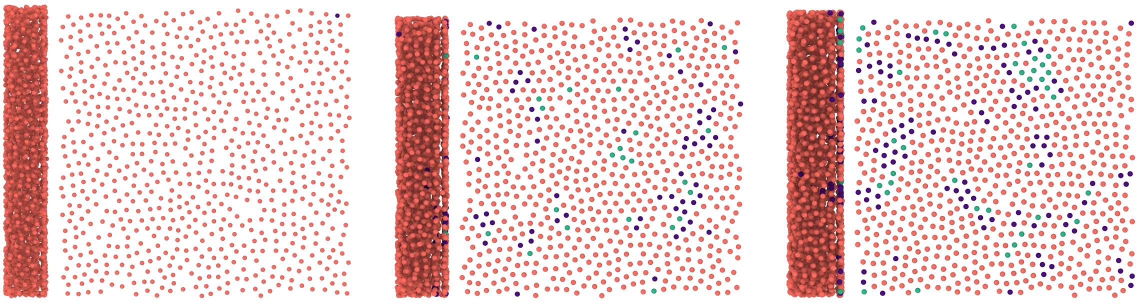

(a) $\eta = 0.0448$, Ten Wolde, Ruiz-Montero, and Frenkel (1995) approach

(b) $\eta = 0.0806$, Ten Wolde, Ruiz-Montero, and Frenkel (1995) approach

(c) $\eta = 0.0896$, Ten Wolde, Ruiz-Montero, and Frenkel (1995) approach

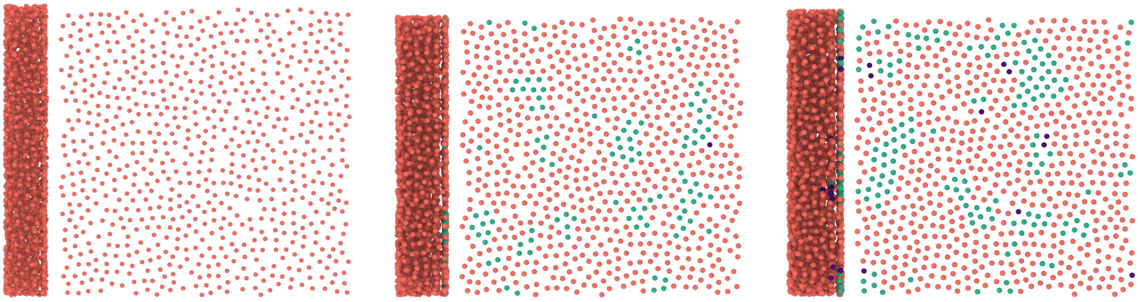

(d) $\eta = 0.0448$, Lechner and Dellago (2008) approach

(e) $\eta = 0.0806$, Lechner and Dellago (2008) approach

(f) $\eta = 0.0896$, Lechner and Dellago (2008) approach

Figure 6.47: shows the structure analysis of the first layer of fluid in hard walls confinement for the coexistence and systems with 10 and 50 % lower densities. The top snapshots belong to the calculation of $q_4q_4 - q_6q_6$ plane, and the bottom ones correspond to the $\bar{q}_4\bar{q}_6$. These snapshots indicate that at the coexistence $\eta^{fl}_{coex} = 0.0896$ and lower densities like $\eta = 0.0806$ the hexagonal layers are formed but around 50% lower than coexistence these layers are amorphous.

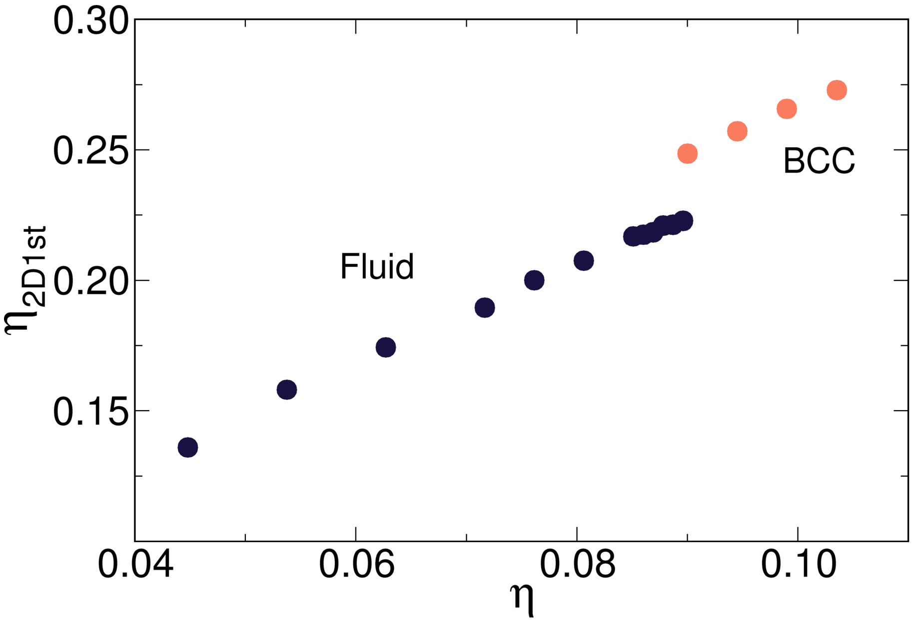

Figure 6.48: show the 2D packing fraction of the first layer η_{2D1st} for BCC-fluid coexistence line at $\kappa\sigma = 2.06155$ and $\beta\varepsilon = 81$.

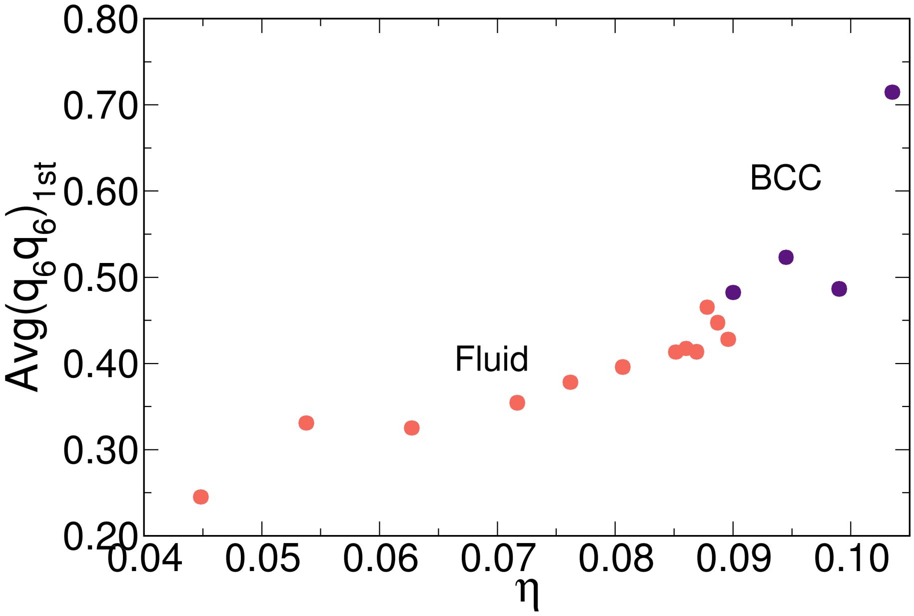

Figure 6.49: shows the average of q_6q_6 for the first layer in the vicinity of the charged wall for BCC crystals and corresponding fluids. The result is in agreement with transition line in figure 6.48.

figure 6.48 by calculating the average values of local order parameter q_6q_6 for the first layer near the walls. Figure 6.49 shows the averaged q_6q_6 and indicates that there is no evidence of transition in these systems.

By studying the structure of the fluid in charged wall confinement, we have found out that there is no evidence of transitions in these systems. So now we can calculate the fluid-wall interfacial free energies γ_{fw} for these systems. Here, we need to consider the Hamiltonian of the fluid which is confined by two parallel flat charged walls as follows

$$\mathcal{H}(\lambda) = \sum_{i=1}^{N} \frac{\vec{p}_i^{\,2}}{2m} + U_{p-p} + U_{p-im}(\lambda) + U_{p-fw}(\lambda) \quad . \tag{6.26}$$

where the interaction between bulk particles and image particles can be described by

$$U_{p-im}(\lambda) = \sum_{i,im} u_{i,im}(\lambda, r_{i,im}) \tag{6.27}$$

$$u_{p-im}(\lambda, r) = (1-\lambda)^2 \, \varepsilon \left(\frac{\exp\left[-\kappa\sigma\left(r/\sigma - 1\right)\right]}{r/\sigma} + \left(\frac{\sigma}{r}\right)^{256} \right)$$

and the interaction of the fluid particles with flat charged walls is formulated as follows

$$U_{p-fw}(\lambda) = \sum_i u_{p-fw}(\lambda, z_i)$$

$$u_{p-fw}(\lambda, z) = \lambda^4 (1-\lambda)^4 \varepsilon \left[\left(\frac{\sigma}{z}\right)^6 + \left(\frac{\sigma}{L_z - z}\right)^6 \right] \tag{6.28}$$

$$+ \lambda^4 \left(\frac{1+\lambda}{2}\right)^4 \varepsilon \left[\exp\left[-\kappa\left(L_z - z - \frac{\sigma}{2}\right) - \kappa\left(z - \frac{\sigma}{2}\right)\right] + \left[\left(\frac{\sigma}{z}\right)^{256} + \left(\frac{\sigma}{L_z - z}\right)^{256} \right] \right]$$

By calculating the partial derivative of the Hamiltonian concerning the λ and then integrating its average over λ from the $\lambda = 0$ which corresponds to the bulk state and $\lambda = 1$ which describes the confined step, we can have access to the free energy difference between two steps. This partial derivative can be written as

$$\frac{\partial \mathcal{H}}{\partial \lambda} = \frac{\partial U_{p-im}(\lambda)}{\partial \lambda} + \frac{\partial U_{p-w}(\lambda)}{\partial \lambda} \tag{6.29}$$

So the partial derivative of the particle-image interaction can be given by

$$\frac{\partial u_{p-im}(\lambda, r)}{\partial \lambda} = -2(1-\lambda) \left(\frac{\exp\left[-\kappa\sigma\left(r/\sigma - 1\right)\right]}{r/\sigma} + \left(\frac{\sigma}{r}\right)^{256} \right) \tag{6.30}$$

And partial derivative of the interaction between bulk particles and charged walls is calculated as

$$\frac{\partial u_{p-fw}(\lambda, z)}{\partial \lambda} = \left[4\lambda^3 (1-\lambda)^3 (2\lambda - 1)\right] \varepsilon \left[\left(\frac{\sigma}{z}\right)^6 + \left(\frac{\sigma}{L_z - z}\right)^6 \right] \tag{6.31}$$

$$+ \left[4\lambda^3 \left(\frac{1+\lambda}{2}\right)^4 + \lambda^4 \frac{4}{2^4} (1+\lambda)^3 \right]$$

$$. \, \varepsilon \left[\exp\left[-\kappa\left(L_z - z - \frac{\sigma}{2}\right) - \kappa\left(z - \frac{\sigma}{2}\right)\right] + \left[\left(\frac{\sigma}{z}\right)^{256} + \left(\frac{\sigma}{L_z - z}\right)^{256} \right] \right]$$

By using this calculation and considering the fluids that are described in table 6.3 we have performed the thermodynamic integration scheme to calculate interfacial free energy of the fluid with the charged walls. To this end, we have performed MD simulation in the NVT ensemble for 51 independent values of λ from 0 to 1. Each simulation has been done for 1.1×10^6 steps with time-step of $dt = 0.001$, and we have collected the thermodynamic properties in each 100 step to calculate the integrand. The calculated smooth and reversible integrands are shown in figure 6.46.

Now, from the integrand of figure 6.50 we can calculate the fluid-wall interfacial free energy γ_{fw}. Figure 6.51 shows the calculated fluid-wall interfacial free energies γ_{fw} for the fluids that are confined between parallel flat charged walls. In contrast to the hard walls case, the values of the interfacial free energy, γ_{fw}, are positive. The reason for this positive value is because the range of fluid-wall and

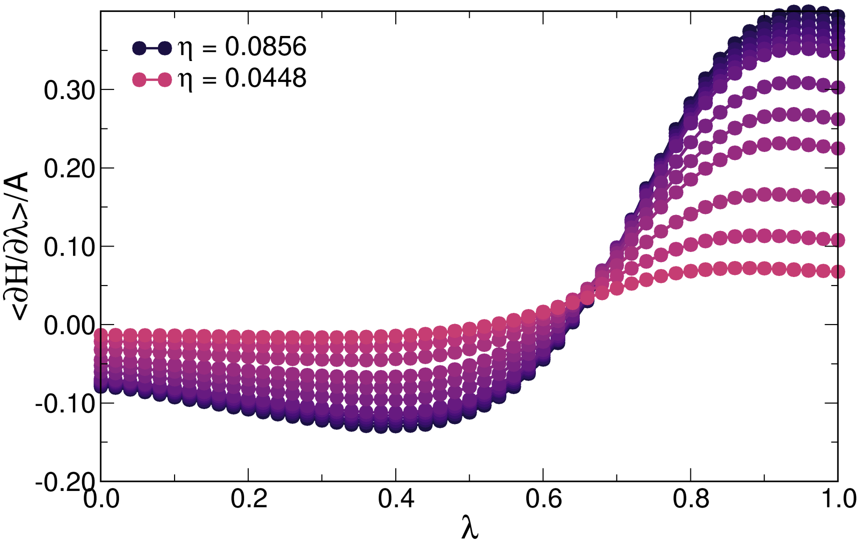

Figure 6.50: shows the calculated integrand for the fluids confined by two parallel flat charged walls. These smooth and reversible integrands show some positive values which can lead to the positive interfacial energies which are in contrast to the hard wall confinement case.

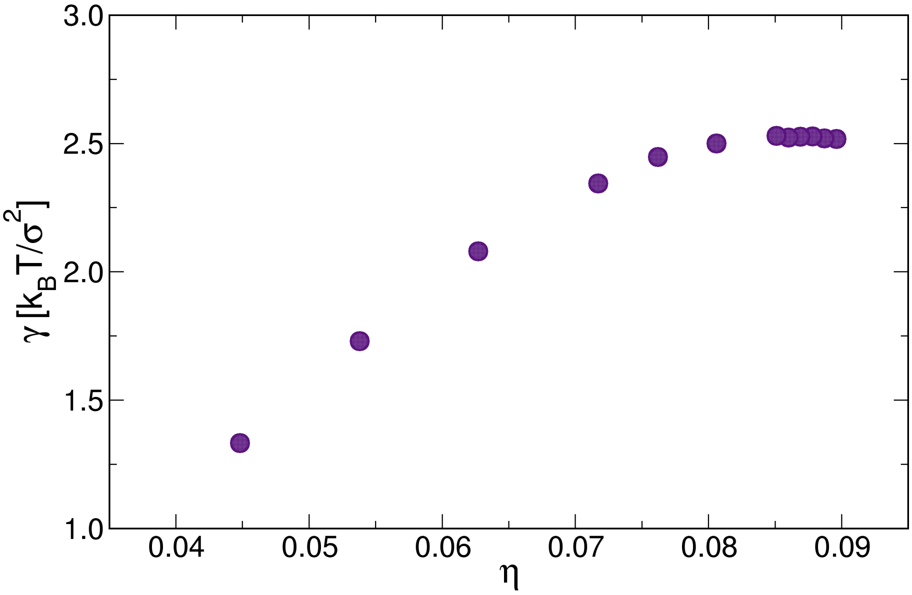

Figure 6.51: shows the calculated value for fluid-wall interfacial free energy γ_{fw} at different packing fractions equal and below the coexistence. The values of γ_{fw} are positive because the particle-image contribution now has been overcome by the fluid-wall interaction contribution.

fluid-fluid interactions are approximately the same and the fluid-wall interactions have a more significant contribution to forming the interface between fluids and flat charged walls.

6.3 Crystal-Fluid Interface

Previously we have shown in figure 6.41 that via equation (6.28) one can have some rough estimation about solid-fluid interfacial free energy. In this section we present the result of the study that we have done on the crystal-fluid interface. We have investigated the FCC(100)-fluid interface at coexistence. By using Thermodynamic integration that is introduced in chapter 4 we have tried to directly calculate the interfacial free energy of solid-fluid interface.

6.3.1 FCC-Fluid Coexistence

To calculate the FCC-fluid interfacial free energy we have performed the thermodynamic integration scheme (see chapter 4). In the first step we have confined the fluid at $\kappa\sigma = 5.1738$ and $\eta^{fl}_{coex} = 0.1366$ with a pair of short-range Gaussian walls. In this step of the thermodynamic integration, the Gaussian walls are gradually turned on at the boundaries of the system in z-direction but periodic boundary conditions are valid in all three spatial directions. The λ-dependent Hamiltonian of this step can be written as

$$\mathcal{H}_1(\lambda) = \sum_{i=1}^{N} \frac{\vec{p}_i^2}{2m} + U_{p-p} + U_{p-fw}(\lambda) \quad . \tag{6.32}$$

in which interaction between fluid particles and the Gaussian wall can be described as

$$U_{p-fw}(\lambda) = \sum_i u_{p-fw}(\lambda, z_i) \tag{6.33}$$

$$u_{p-fw}(\lambda, z) = \lambda^2 A \left(\exp\left[-\left(\frac{z}{B}\right)^2 \right] + \exp\left[-\left(\frac{L_z - z}{B}\right)^2 \right] \right)$$

where z is the distance of particle from the wall, $A = 25/\beta\varepsilon$ and $B = 0.02739\sigma$. Same process has been done for a system of FCC(100) crystal at $\kappa\sigma = 5.1738$ and $\eta^{FCC}_{coex} = 0.1396$. So the Hamiltonian for this can be written as

$$\mathcal{H}_2(\lambda) = \sum_{i=1}^{N} \frac{\vec{p}_i^2}{2m} + U_{p-p} + U_{p-fw}(\lambda) \quad . \tag{6.34}$$

Figure 6.52 show the calculated integrand for first two steps of thermodynamic integration. The corresponding free energy for these two steps are calculated

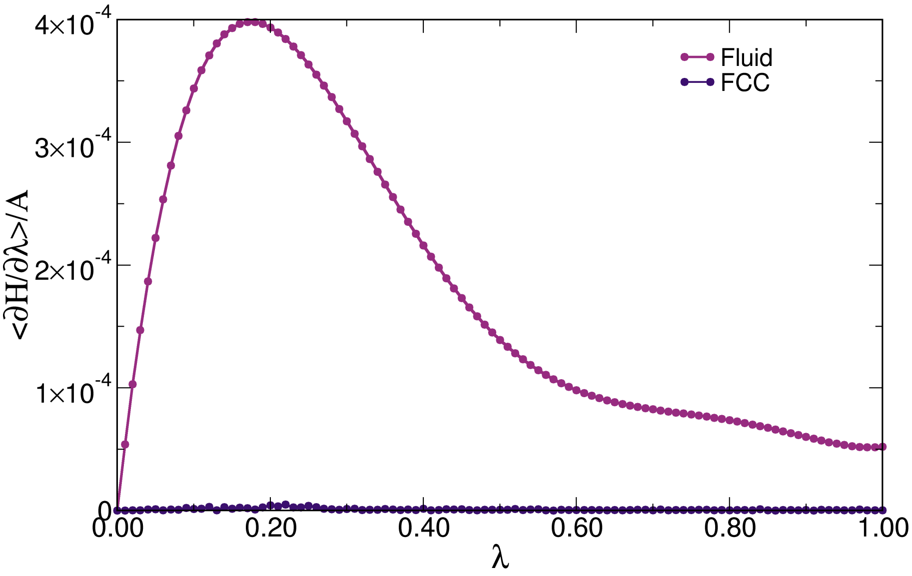

Figure 6.52: shows the calculated integrands for fluid-Gaussian wall (step1) and FCC-Gaussian wall (Step2) at at $\kappa\sigma = 5.1738$, $\eta^{fl}_{coex} = 0.1366$ and $\eta^{FCC}_{coex} = 0.1396$.

as $\Delta F_1/A = 1.806 \times 10^{-4}$ and $\Delta F_2/A = 1.064 \times 10^{-6}$. As one can see the value of the contribution of the short-range in these two steps is too small which can be neglected in the final value of FCC-fluid interfacial free energy.

In step three, we consider a fluid at $\eta^{fl}_{coex} = 0.1366$ which is confined by its own frozen version. To this end we consider several layers of the fluid from step 1 with width of 7σ from each end of the system. Then we place the walls as we have discussed in chapter 3 (see figure 4.1). In this step we gradually turn on the interaction of the bulk particles with frozen walls and in meantime turn off the particle-image interactions. The λ-dependent Hamiltonian of this step can be written as

$$\mathcal{H}_3(\lambda) = \sum_{i=1}^{N} \frac{\vec{p}_i^{\,2}}{2m} + U_{p-p} + U_{p-im}(\lambda) + U_{p-pw}(\lambda) \quad . \tag{6.35}$$

where the interaction between bulk particles and image particles can be described by

$$U_{p-im}(\lambda) = \sum_{i,im} u_{i,im}(\lambda, r_{i,im}) \tag{6.36}$$
$$u_{p-im}(\lambda, r) = (1-\lambda)^{12}\,\varepsilon \left(\frac{\exp\left[-\kappa\sigma\,(r/\sigma - 1)\right]}{r/\sigma} + \left(\frac{\sigma}{r}\right)^{256} \right)$$

and interaction between particles and structured wall (frozen fluid wall) can be written as

$$U_{p-pw}(\lambda) = \sum_{i,pw} u_{i,pw}(\lambda, r_{i,pw}) \tag{6.37}$$
$$u_{p-pw}(\lambda, r) = \lambda^{12}\varepsilon \left(\frac{\exp\left[-\kappa\sigma\,(r/\sigma - 1)\right]}{r/\sigma} + \left(\frac{\sigma}{r}\right)^{256} \right)$$

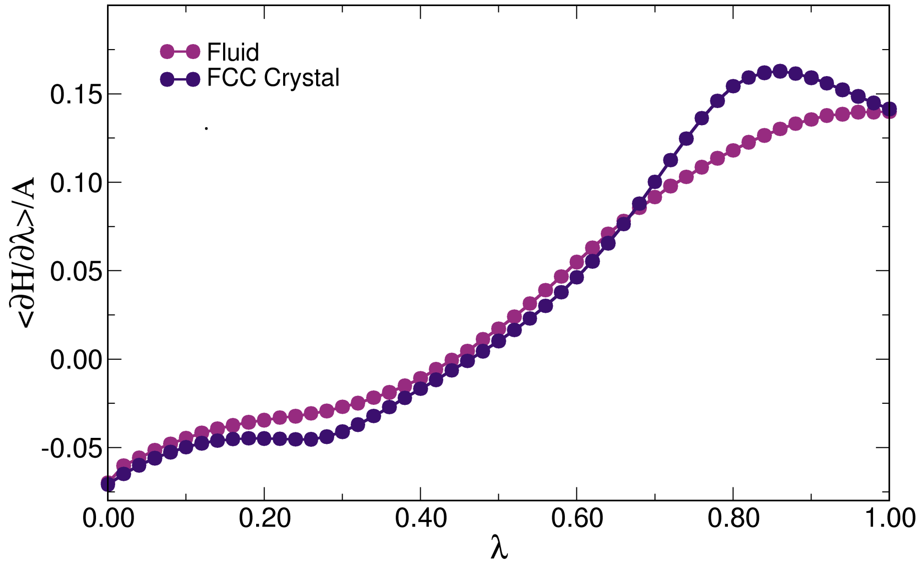

Figure 6.53: shows the calculated integrands for step 3 and Step 4 at $\kappa\sigma = 5.1738$, $\eta^{fl}_{coex} = 0.1366$ (step 3), and $\eta^{FCC}_{coex} = 0.1396$ (step 4)

Step four is same as the step three but with this difference that we are confining the final configuration of the FCC crystal with $\eta^{FCC}_{coex} = 0.1396$ from step two with its frozen version. This frozen version is made by several layers of the FCC crystal with a width of 7σ. To simultaneously turning off the periodic boundary condition in z-direction and turning on the interaction with structured walls, the λ-dependent Hamiltonian can be written as

$$\mathcal{H}_4(\lambda) = \sum_{i=1}^{N} \frac{\vec{p}_i^{\,2}}{2m} + U_{p-p} + U_{p-im}(\lambda) + U_{p-pw}(\lambda) \quad . \tag{6.38}$$

in which the interaction between bulk particles and image particles can be written as

$$\begin{aligned} U_{p-im}(\lambda) &= \sum_{i,im} u_{i,im}(\lambda, r_{i,im}) \\ u_{p-im}(\lambda, r) &= (1-\lambda)^{12}\,\varepsilon \left(\frac{\exp\left[-\kappa\sigma\left(r/\sigma - 1\right)\right]}{r/\sigma} + \left(\frac{\sigma}{r}\right)^{256} \right) \end{aligned} \tag{6.39}$$

and one can describe interaction between particles and structured wall (frozen FCC wall)

$$\begin{aligned} U_{p-pw}(\lambda) &= \sum_{i,pw} u_{i,pw}(\lambda, r_{i,pw}) \\ u_{p-pw}(\lambda, r) &= \lambda^{12}\varepsilon \left(\frac{\exp\left[-\kappa\sigma\left(r/\sigma - 1\right)\right]}{r/\sigma} + \left(\frac{\sigma}{r}\right)^{256} \right) \end{aligned} \tag{6.40}$$

The calculated integrands for Step three and four is presented in figure 6.53. Moreover, values for free energy difference regarding step 3 and 4 are calculated as $\Delta F_3/A = 1.431 \times 10^{-2}$ and $\Delta F_4/A = 1.149 \times 10^{-2}$.

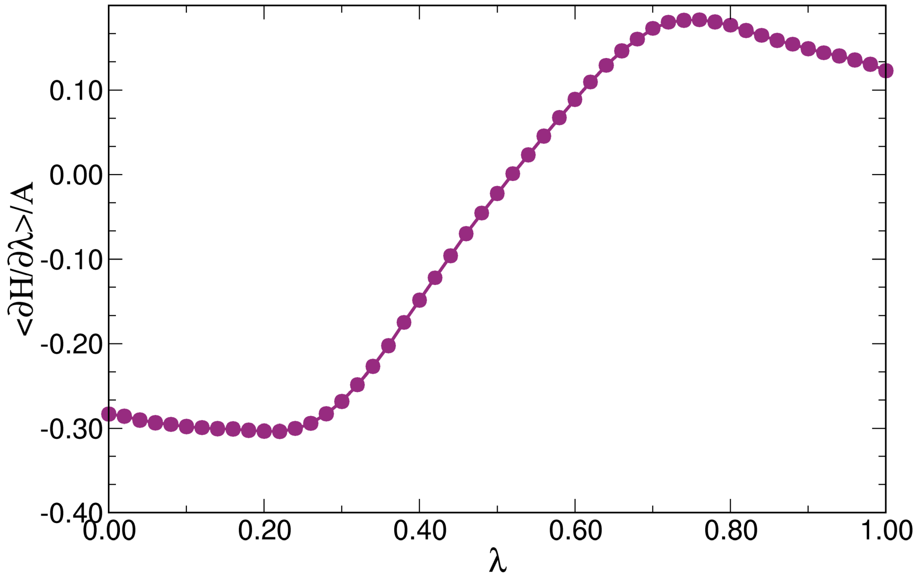

Figure 6.54: shows the calculated integrands for step 5 at $\kappa\sigma = 5.1738$, $\eta^{fl}_{coex} = 0.1366$, and $\eta^{FCC}_{coex} = 0.1396$

.

In step 5, we brought final configurations of steps 3 and 4 together. In this step via thermodynamic integration scheme, we gradually turn off the interaction of bulk FCC and fluid with their corresponding frozen walls and in the meantime the interaction between FCC and fluid is turning on, i.e, when $\lambda = 0$ the bulk FCC and fluid does not have any interactions and in $\lambda = 1$ there is no interaction between bulk particles and frozen walls.

However, we were able to calculate the integrand for step 5 (see figure 6.54), but the final configuration of this step indicates the formation of crystalline layers in fluids in contact with FCC crystal (see figure 6.55). So due to this crystallization, the obtained values do not make much sense and our thermodynamic integration scheme does not work to calculate free energy of FCC-fluid interface. This crystallization can be because of the sensitivity of the coexistence densities regarding finite size effect.

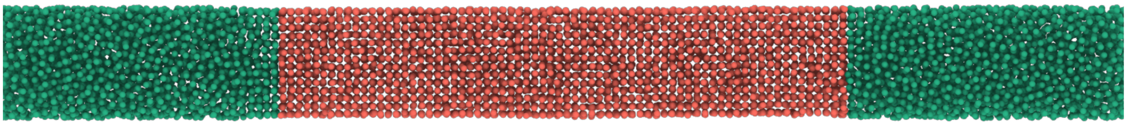

Figure 6.55: shows the snapshot of the final configuration of step 5 which indicates the crystallization fluids in contact with FCC crystal.

7 Conclusions & Outlook

In this work, we have studied the phase behavior of hard-core Yukawa BCC, FCC, and fluid phases in confinements. We have investigated two different types of confinements; a) flat hard walls, and b) flat charged walls. For these two types of confinements, we considered states around BCC-fluid and FCC-fluid coexistence, separately.

For the confined FCC(111) crystal confined between a pair of flat hard walls, the calculated density profiles show that the FCC(111) crystal with coexistence density $\eta_{\mathrm{coex}}^{\mathrm{FCC}} = 0.1369$ is stable in the hard wall confinement. The behavior of the higher density FCC(111) crystals (up to 20% higher than coexistence) also have been investigated, and we observed the same behavior as coexistence FCC(111). Not only from the calculated density profiles it is obvious that FCC(111) crystals are stable in confinement and there is no evidence for any transition in these systems, but also the structure analysis of confined FCC(111) crystals via calculation of local bond order parameters q_6q_6, q_4q_4, $\bar{q}_6$ and $\bar{q}_4$ confirms this assumption. Furthermore, we have employed a thermodynamic integration method to calculate the FCC-wall interfacial free energies γ_{cw}. These interfacial free energies are negative. The reason for this negativity is that due to the significant contribution of particle-interactions, particles tend to be attracted to the flat hard walls.

We have also investigated the phase behavior of the fluid (corresponding to FCC(111)) at coexistence $\eta_{\mathrm{coex}}^{\mathrm{fl}} = 0.1366$ as well as densities below the coexistence density. We have calculated the density profiles for these fluids. These density profiles indicate that some dense layers are formed in the vicinity of the walls. These layers appear to be denser than the bulk density, and the density of the first layer in the vicinity of the wall is increasing by the increment of packing fraction η. Moreover, the number of formed layers are growing by the packing fraction. In the first sight, we can observe that the 2D packing fraction of the first layer near the wall at coexistence is even higher than the one for FCC(111) coexistence density. This statement is valid also for densities well below coexistence. The structure analysis via q_6q_6, q_4q_4, $\bar{q}_6$ and $\bar{q}_4$ as local bond order parameters for the coexistence fluid showed that there is a transition from fluid to hexagonal order in the vicinity of the wall. This phenomenon, known as pre-freezing, was also observed for hard-sphere fluid in hard wall confinement. However, in the case of hard-core Yukawa fluid, we have also observed the pre-freezing phenomenon at densities well below coexistence. Calculation of an average local bond order parameter for the first layers q_6q_6 in the vicinity of the hard wall confirms that the transition is happening from a density around $\eta = 0.1298$ and below this density the layers in the vicinity of the walls are amorphous. Moreover, by performing a thermodynamic integration method, we calculated the free energy of the fluid-wall interface. Since the hard walls are attractive for the bulk hard-core Yukawa particles, there is a trend of particles near the walls, these interfacial free energies are negative. However, the obtained values for the systems with phase transition are not reliable.

We have also studied the phase behavior of BCC(111) crystal at flat hard wall confinement. We considered BCC(111) crystal at coexistence density $\eta^{BCC}_{coex} = 0.0900$ up to densities 20% above coexistence. At coexistence, we observed the formation of several layers in the vicinity of the wall and structure analysis via the local bond order parameter showed that the layer near the hard walls has hexagonal order. Right after these layers, we observed a melting which is a sign of pre-melting. Also, the rest of the particles remain with the BCC structure. We have observed the pre-melting also for higher densities, but the only difference is the width of the melted area which is decreasing by the increment of packing fraction η. Moreover, by having phase transitions for these confined systems, we were not able to perform thermodynamic integration to calculate the free energy of the BCC-wall interface.

By confining the fluid at coexistence density $\eta^{fl}_{coex} = 0.0896$ with a pair of flat hard walls, we have studied the phase behavior and structure of this system. This fluid showed the pre-freezing phenomenon and formation of a hexagonal layer near the hard wall. Besides, we have studied fluids with densities up to 50% below coexistence. These systems, up to $\eta = 0.0717$ which is 20% below the coexistence, showed a transition from a of fluid to a hexagonal layers in the vicinity of the hard walls. For the sufficiently low-density fluids (from 30% below the coexistence) the layers near the hard walls are amorphous. Calculation of local bond order parameters as well as the calculation of an average q_6q_6 for the first layer near the wall confirms that the transition has happened from $\eta = 0.0717$. Due to the phase transition in the confined fluid systems we were able to perform a thermodynamic integration only for the low-density fluids. The calculated values for the free energy of the fluid-wall interface are negative.

To study the phase behavior of the hard-core Yukawa systems including BCC, FCC, and fluids we have used a pair of flat charged walls. We have confined the FCC(111) crystal at coexistence, $\eta^{\mathrm{FCC}}_{\mathrm{coex}} = 0.1396$, as well as crystals with densities up to 20% above coexistence by a pair of flat charged walls. Our observation of density profiles and calculation of a 2D packing fraction for the layer in the vicinity of the walls confirm that the FCC(111) crystals are stable for the charged wall confinement which we have also observed for the hard wall case. These observations are also verified by a structure analysis via calculation of local bond order parameters. By performing the thermodynamic integration scheme, we were able to calculate the free energy of the FCC-wall interface. In contrast to the hard wall case, these calculated values of free energy are positive. The reason is now the range of both particle-particle, and particle-wall interactions are long, and their contribution makes the walls less attractive than in the hard wall case.

Moreover, we studied the phase behavior of fluid at coexistence $\eta^{\mathrm{fl}}_{\mathrm{coex}} = 0.1366$ as well as densities well below the coexistence in charged wall confinement. However, same as the hard wall confinement, we have observed the formation of several layers in the vicinity of the walls, but from the density profiles and calculation of 2D packing fraction of these layers η_{2D1st} one can see that these layers have a lower density than the ones for the hard wall case. Structure analysis via calculation of local bond order parameters such as q_6q_6, q_4q_4, $\bar{q}_6$ and $\bar{q}_4$ showed that these layers in the vicinity of the charged walls are amorphous and there is no evidence of a phase transition in these systems. So, we could perform the thermodynamic integration scheme to calculate the free energy of the fluid-wall interface for the density at coexistence and densities below the coexistence density. Same as the confined FCC(111) case, here the charged walls are less attractive for the particles, and it makes the positive values for interfacial free energies.

We have confined BCC(111) crystals at coexistence and up to 20% above coexistence between a pair of charged walls. The density profiles of these crystals at confinement show that similar to the hard wall case the systems are divided into three regions, several layers near the charged walls, a melted area with a density corresponding to the bulk density and stable BCC crystal. We have studied the structure of the layers in the vicinity of the wall by calculation of local bond order parameters. It turns out that the layer in the vicinity of the wall has no specific order and is amorphous. However, in a very high-density crystal, the particles within the first layer tend to form a hexagonal structure. Moreover, due to the phase transitions in these confined crystals, we could not use the thermodynamic integration scheme to calculate the free energy of the BCC-wall interface.

As the last confined system, we have considered the fluid state around the BCC-fluid coexistence between a pair of charged walls. These systems are the coexistence density and the fluid up to 50% below the coexistence density. The density profiles of these fluids show the formation of some dense layers which are not as dense as the layers in a hard wall case. The structure analysis via local bond order parameters shows that these layers in the vicinity of the walls do not have any specific order and they are amorphous layers. Since no phase transition has been observed in these cases, we were able to use the thermodynamic integration scheme to calculate the free energy of the fluid-wall interface. In contrast to the hard wall case, The calculated values for interfacial free energies are positive.

As the final step to calculate the free energy of the FCC-fluid interface at coexistence, we have employed a modified thermodynamic integration method consist of six steps. With these steps we tried directly calculate the FCC-fluid interfacial free energy. However, due to the crystallization of the fluid in contact with FCC crystal, this method is not valid to calculate the free energy of the FCC-fluid interface.

The issues and results which we have presented in this thesis is have not been considered and studied via experiment for charge colloids. In this point, we think that would be a good model in the real system, and one could address them via designing a specific experiment.

Bibliography

Alexander, S. (1978). S. alexander and j. mctague, phys. rev. lett. 41, 702 (1978). *Phys. Rev. Lett. 41*, 702. (Cit. on p. 9).

Auerbach, D., Paul, W., Bakker, A., Lutz, C., Rudge, W., & Abraham, F. F. (1987). A special purpose parallel computer for molecular dynamics: Motivation, design, implementation, and application. *Journal of Physical Chemistry*, *91*(19), 4881–4890. (Cit. on p. 29).

Benjamin, R., & Horbach, J. (2012). Wall-liquid and wall-crystal interfacial free energies via thermodynamic integration: A molecular dynamics simulation study. *The Journal of chemical physics*, *137*(4), 044707. (Cit. on pp. 3, 35).

Benjamin, R., & Horbach, J. (2014a). Crystal-liquid interfacial free energy via thermodynamic integration. *Journal of Chemical Physics*, *141*(4). doi:10.1063/1.4891220. arXiv: arXiv:1406.0418v1. (Cit. on p. 35)

Benjamin, R., & Horbach, J. (2014b). Crystal-liquid interfacial free energy via thermodynamic integration. *The Journal of chemical physics*, *141*(4), 044715. (Cit. on p. 37).

Benjamin, R., & Horbach, J. (2015). Crystal-liquid interfacial free energy of hard spheres via a thermodynamic integration scheme. *Physical Review E*, *91*(3), 032410. (Cit. on pp. 19, 35, 37).

Bennett, C. H. (1976). Efficient estimation of free energy differences from monte carlo data. *Journal of Computational Physics*, *22*(2), 245–268. (Cit. on p. 11).

Berendsen, H. J., Postma, J. v., van Gunsteren, W. F., DiNola, A., & Haak, J. (1984). Molecular dynamics with coupling to an external bath. *The Journal of chemical physics*, *81*(8), 3684–3690. (Cit. on p. 23).

Binder, K. (1992). Phase transitions in reduced geometry. *Annual Review of Physical Chemistry*, *43*(1), 33–59. (Cit. on p. 1).

Binder, K. [Kurt]. (1987). Theory of first-order phase transitions. *Reports on progress in physics*, *50*(7), 783. (Cit. on p. 31).

Binder, K. [Kurt], Horbach, J., Vink, R., & De Virgiliis, A. (2008). Confinement effects on phase behavior of soft matter systems. *Soft Matter*, *4*(8), 1555–1568. (Cit. on p. 1).

Bonn, D., Eggers, J., Indekeu, J., Meunier, J., & Rolley, E. (2009). Wetting and spreading. *Reviews of modern physics*, *81*(2), 739. (Cit. on p. 15).

Broughton, J. Q., & Gilmer, G. H. (1986). Molecular dynamics investigation of the crystal–fluid interface. vi. excess surface free energies of crystal–liquid systems. *The Journal of chemical physics*, *84*(10), 5759–5768. (Cit. on pp. 36, 37).

Callen, H. B. (1998). Thermodynamics and an introduction to thermostatistics. AAPT. (Cit. on p. 33).

Carbajal-Tinoco, M. D., Castro-Román, F., & Arauz-Lara, J. L. (1996). Static properties of confined colloidal suspensions. *Physical Review E*, *53*(4), 3745. (Cit. on p. 18).

Courtemanche, D. J., Pasmore, T. A., & Van Swol, F. (1993). A molecular dynamics study of prefreezing: Hard spheres at a smooth hard wall. *Molecular Physics*, *80*(4), 861–875. (Cit. on p. 17).

Courtemanche, D. J., & van Swol, F. (1992). Wetting state of a crystal-fluid system of hard spheres. *Physical review letters*, *69*(14), 2078. (Cit. on pp. 1, 16, 17).

Davidchack, R. L., & Laird, B. B. (2000). Direct calculation of the hard-sphere crystal/melt interfacial free energy. *Physical review letters*, *85*(22), 4751. (Cit. on p. 37).

Davidchack, R. L., & Laird, B. B. (2003). Direct calculation of the crystal–melt interfacial free energies for continuous potentials: Application to the lennard-jones system. *The Journal of chemical physics*, *118*(16), 7651–7657. (Cit. on pp. 34, 51, 58, 59).

De Gennes, P.-G. (1985). Wetting: Statics and dynamics. *Reviews of modern physics*, *57*(3), 827. (Cit. on p. 33).

de, G. P., Brochard-Wyart, F., & Quere, D. (2004). Capillarity and wetting phenomena: Drops, bubbles, pearls, waves. (Cit. on p. 33).

de Gennes, P.-G. (1981). Some effects of long range forces on interfacial phenomena. *Journal de Physique Lettres*, *42*(16), 377–379. (Cit. on p. 15).

Derjaguin, B., & Landau, L. (1941). The theory of stability of highly charged lyophobic sols and coalescence of highly charged particles in electrolyte solutions. *Acta Physicochim. URSS*, *14*(633-52), 58. (Cit. on p. 10).

Dhont, J. K. (1996). *An introduction to dynamics of colloids*. Elsevier. (Cit. on p. 5).

Dietrich, S. (1988). Phase transitions and critical phenomena. Academic London. (Cit. on p. 33).

Dijkstra, M. (2004). Capillary freezing or complete wetting of hard spheres in a planar hard slit? *Physical review letters*, *93*(10), 108303. (Cit. on pp. 1, 16, 17).

El Azhar, F., Baus, M., Ryckaert, J.-P., & Meijer, E. J. (2000). Line of triple points for the hard-core yukawa model: A computer simulation study. *The Journal of Chemical Physics*, *112*(11), 5121–5126. (Cit. on pp. 2, 12).

Eshraghi, M. (2015). *Interfaces of methane in metal organic frameworks (mofs)*. Heinrich-Heine University of Duesseldorf. (Cit. on pp. 28, 29).

Fortini, A., & Dijkstra, M. (2006). Phase behaviour of hard spheres confined between parallel hard plates: Manipulation of colloidal crystal structures by confinement. *Journal of Physics: Condensed Matter*, *18*(28), L371. (Cit. on pp. 1, 17, 34, 51, 58, 59).

Frenkel, D., & Smit, B. (2001). *Understanding molecular simulation: From algorithms to applications*. Elsevier. (Cit. on pp. 22, 24, 28, 32).

Gallardo, A., Grandner, S., Almarza, N. G., & Klapp, S. H. (2012). Theory of repulsive charged colloids in slit-pores. *The Journal of chemical physics*, *137*(1), 014702. (Cit. on p. 2).

Glicksman, M., & Singh, N. (1989). Effects of crystal-melt interfacial energy anisotropy on dendritic morphology and growth kinetics. *Journal of crystal growth*, *98*(3), 277–284. (Cit. on p. 33).

Grandner, S., & Klapp, S. H. (2008). Freezing of charged colloids in slit pores. *The Journal of Chemical Physics*, *129*(24), 244703. (Cit. on pp. 2, 18).

Hamaguchi, S., Farouki, R., & Dubin, D. (1996). Phase diagram of yukawa systems near the one-component-plasma limit revisited. *The Journal of chemical physics*, *105*(17), 7641–7647. (Cit. on p. 9).

Hamaguchi, S., Farouki, R., & Dubin, D. (1997). Triple point of yukawa systems. *Physical Review E*, *56*(4), 4671. (Cit. on pp. 9, 10, 13).

Hansen, J.-P., & McDonald, I. R. (1990). *Theory of simple liquids*. Elsevier. (Cit. on p. 18).

Heni, M., & Löwen. (1999). Interfacial free energy of hard-sphere fluids and solids near a hard wall. *Physical Review E*, *60*(6), 7057. (Cit. on p. 34).

Hockney, R. W., & Eastwood, J. W. (1988). *Computer simulation using particles*. crc Press. (Cit. on p. 27).

Howe, J. (1997). Interfaces in materials: Atomic structure, kinetics and thermodynamics of solid-vapor, solid-liquid and solid-solid interfaces. New York: Wiley. (Cit. on p. 33).

Hückel, E., & Debye, P. (1923). Zur theorie der elektrolyte. i. gefrierpunktserniedrigung und verwandte erscheinungen. *Phys. Zeitschrift*, *24*, 185. (Cit. on p. 7).

Huisman, W. J., Peters, J. F., Zwanenburg, M. J., de Vries, S. A., Derry, T. E., Abernathy, D., & van der Veen, J. F. (1997). Layering of a liquid metal in contact with a hard wall. *Nature*, *390*(6658), 379. (Cit. on p. 17).

Hünenberger, P. H. (2005). Thermostat algorithms for molecular dynamics simulations. In *Advanced computer simulation* (pp. 105–149). Springer. (Cit. on p. 24).

Hynninen, A.-P., & Dijkstra, M. (2003). Phase diagrams of hard-core repulsive yukawa particles. *Physical Review E*, *68*(2), 021407. (Cit. on pp. 2, 12–14, 19–21, 52, 64–66).

Ivlev, A., LÃ, H., Morfill, G., Royall, C. P. et al. (2012). *Complex plasmas and colloidal dispersions: Particle-resolved studies of classical liquids and solids*. World Scientific Publishing Company. (Cit. on p. 6).

Karanikas, S., Dzubiella, J., Moncho-Jordá, A., & Louis, A. (2008). Density profiles and solvation forces for a yukawa fluid in a slit pore. *The Journal of chemical physics*, *128*(20), 204704. (Cit. on pp. 21, 75).

Kegel, W. K. (2001). Freezing of hard spheres in confinement. *The Journal of Chemical Physics*, *115*(14), 6538–6549. (Cit. on pp. 1, 16).

Kirkwood, J. G., & Buff, F. P. (1949). The statistical mechanical theory of surface tension. *The Journal of Chemical Physics*, *17*(3), 338–343. (Cit. on p. 33).

Kofke, D. A. (1993). Gibbs-duhem integration: A new method for direct evaluation of phase coexistence by molecular simulation. *Molecular Physics*, *78*(6), 1331–1336. (Cit. on pp. 11, 12).

Laird, B. B., & Davidchack, R. L. (2007). Wall-induced prefreezing in hard spheres: A thermodynamic perspective. *The Journal of Physical Chemistry C*, *111*(43), 15952–15956. (Cit. on pp. 1, 16).

Lechner, W., & Dellago, C. (2008). Accurate determination of crystal structures based on averaged local bond order parameters. *The Journal of chemical physics*, *129*(11), 114707. (Cit. on pp. 43, 45, 47, 55–58, 68, 69, 71, 77, 78, 80, 81, 89–92).

Louis, A., Allahyarov, E., Löwen, H., & Roth, R. (2002). Effective forces in colloidal mixtures: From depletion attraction to accumulation repulsion. *Physical Review E*, *65*(6), 061407. (Cit. on p. 21).

MacQueen, J. et al. (1967). Some methods for classification and analysis of multivariate observations. In *Proceedings of the fifth berkeley symposium on mathematical statistics and probability* (Vol. 1, *14*, pp. 281–297). Oakland, CA, USA. (Cit. on p. 47).

Meijer, E. J., & El Azhar, F. (1997). Novel procedure to determine coexistence lines by computer simulation. application to hard-core yukawa model for charge-stabilized colloids. *The Journal of chemical physics*, *106*(11), 4678–4683. (Cit. on pp. 2, 11, 12).

Meijer, E. J., & Frenkel, D. (1991). Melting line of yukawa system by computer simulation. *The Journal of chemical physics*, *94*(3), 2269–2271. (Cit. on p. 8).

Messina, R., & Löwen, H. [Hartmut]. (2003). Reentrant transitions in colloidal or dusty plasma bilayers. *Physical review letters*, *91*(14), 146101. (Cit. on p. 2).

Monovoukas, Y., & Gast, A. P. (1989). The experimental phase diagram of charged colloidal suspensions. *Journal of colloid and interface science*, *128*(2), 533–548. (Cit. on p. 2).

Navascues, G. (1979). Liquid surfaces: Theory of surface tension. *Reports on Progress in Physics*, *42*(7), 1131. (Cit. on p. 33).

Pathria, R. K., & Beale, P. D. (2012). *Statistical mechanics*. Elsevier. (Cit. on p. 32).

Pistoor, N. (1991). *Struktur und dynamik von yukawa-systemen* (Doctoral dissertation, Johannes Gutenberg University Mainz). (Cit. on p. 7).

Plimpton, S. (1995). Fast parallel algorithms for short-range molecular dynamics. *Journal of computational physics*, *117*(1), 1–19. (Cit. on p. 51).

Pollock, E. L., & Hansen, J.-P. (1973). Statistical mechanics of dense ionized matter. ii. equilibrium properties and melting transition of the crystallized one-component plasma. *Physical Review A*, *8*(6), 3110. (Cit. on p. 14).

Puertas, A. M., de las Nieves, F. J., & Cuetos, A. (2015). Computer simulations of charged colloids in confinement. *Journal of colloid and interface science*, *440*, 292–298. (Cit. on p. 18).

Robbins, M. O., Kremer, K., & Grest, G. S. (1988). Phase diagram and dynamics of yukawa systems. *The Journal of chemical physics*, *88*(5), 3286–3312. (Cit. on pp. 8–10).

Roth, R. [R.], & Dietrich, S. [S.]. (2000). Binary hard-sphere fluids near a hard wall. *Phys. Rev. E*, *62*(5), 6926. (Cit. on p. 1).

Russel, W. B., Saville, D. A., & Schowalter, W. R. (1991). *Colloidal dispersions*. Cambridge university press. (Cit. on p. 6).

Russell, S. J., & Norvig, P. (2016). *Artificial intelligence: A modern approach*. Malaysia; Pearson Education Limited, (cit. on p. 47).

Samuel, A. L. (1959). Some studies in machine learning using the game of checkers. *IBM Journal of research and development*, *3*(3), 210–229. (Cit. on p. 47).

Schmidt, M., & Löwen. (1997). Phase diagram of hard spheres confined between two parallel plates. *Physical Review E*, *55*(6), 7228. (Cit. on pp. 1, 17).

Schneider, T., & Stoll, E. (1978). Molecular-dynamics study of second sound. *Physical Review B*, *18*(12), 6468. (Cit. on p. 23).

Sharma, A. (2012). Introduction to colloid and interface science and engineering. Chemical Engineering IIT Kanpur. (Cit. on p. 7).

Snook, I. K., & Henderson, D. (1978). Monte carlo study of a hard-sphere fluid near a hard wall. *The Journal of Chemical Physics*, *68*(5), 2134–2139. (Cit. on pp. 1, 16).

Steinhardt, P. J., Nelson, D. R., & Ronchetti, M. (1983). Bond-orientational order in liquids and glasses. *Physical Review B*, *28*(2), 784. (Cit. on p. 42).

Stukowski, A. (2009). Visualization and analysis of atomistic simulation data with ovito–the open visualization tool. *Modelling and Simulation in Materials Science and Engineering*, *18*(1), 015012. (Cit. on p. 51).

Swope, W. C., Andersen, H. C., Berens, P. H., & Wilson, K. R. (1982). A computer simulation method for the calculation of equilibrium constants for the formation of physical clusters of molecules: Application to small water clusters. *The Journal of Chemical Physics*, *76*(1), 637–649. (Cit. on p. 22).

Ten Wolde, P. R., Ruiz-Montero, M. J., & Frenkel, D. (1995). Numerical evidence for bcc ordering at the surface of a critical fcc nucleus. *Physical review letters*, *75*(14), 2714. (Cit. on pp. 42–44, 55–58, 68, 69, 71, 77, 78, 80, 81, 89–92).

Tuckerman, M., Berne, B. J., & Martyna, G. J. (1992). Reversible multiple time scale molecular dynamics. *The Journal of chemical physics*, *97*(3), 1990–2001. (Cit. on p. 24).

Turnbull, D. (1952). Kinetics of solidification of supercooled liquid mercury droplets. *The Journal of chemical physics*, *20*(3), 411–424. (Cit. on p. 36).

Verlet, L. (1967). Computer"experiments"on classical fluids. i. thermodynamical properties of lennard-jones molecules. *Physical review*, *159*(1), 98. (Cit. on p. 27).

Verwey, J., & Overbeek, T. (1948). Theory of the stability of lyophobic colloids. *Advances in Colloid Interface Science. Elsevier: Amsterdam*, *17*. (Cit. on p. 10).

Young, T. et al. (1805). Iii. an essay on the cohesion of fluids. *Philosophical transactions of the royal society of London*, *95*, 65–87. (Cit. on p. 15).

Eidesstattliche Versicherung

Ich versichere an Eides Statt, dass die Dissertation von mir selbständig und ohne unzulässige fremde Hilfe unter Beachtung der „Grundsätze zur Sicherung guter wissenschaftlicher Praxis an der Heinrich-Heine-Universität Düsseldorf“ erstellt worden ist.

Düsseldorf, den 11.03.2019 *Mojtaba Eshraghi*